University of Oklahoma

Graduate College

Microwave Electrometry with Rydberg

Eletromagnetically Induced Transparency in Vapor Cells

A Dissertation

Submitted to the Graduate Faculty

in partial fullfillment of the requirements for the

degree of

Doctor of Philosophy

By

HAOQUAN FAN
Norman, Oklahoma
2016

MICROWAVE ELECTROMETRY WITH RYDBERG ELETROMAGNETICALLY INDUCED TRANSPARENCY IN VAPOR CELLS

A DISSERTATION APPROVED FOR THE
HOMER L. DODGE DEPARTMENT OF PHYSICS AND ASTRONOMY

BY

_____

Dr. James P. Shaffer, Chair

_____

Dr. Peter Barker

_____

Dr. John E. Moore-Furneaux

_____

Dr. Eric R. I. Abraham

_____

Dr. Gregory A. Parker

To my parents and grandparents

Acknowledgements

I would like to thank my advisor, Professor James P. Shaffer for his constant enthusiasm on supporting me on researches in his group. His support ranges from inspiration ideas to hand-to-hand work with me together on optical tables. His strong belief in his scientific ideas including the way to achieve them in experiment paves the way to every point of my everyday work in the lab. It has been an honor to work under his patient direction.

I would also like to thank Professor Neil E. Shafer-Ray for encouraging me to stay in atomic and molecular physics even when he had severe illness. The passion and creativity on his pursuit in physics are invisible driving forces, stronger than any words, spurring me on all the way of academic world. Special thanks should go to Professor John E. Moore-Furneaux, whose love in physics is an invaluable wealth which I am sharing in every possible way. His enthusiastic explanations in physics, as well as the encouragement from him during my hard time, inspire me all the way along my PhD period.

I appreciate the help from Ms. Adrienne Wade, the director of electronic shop in the physics department. She is always helpful with everything I need in her electronic shop. In addition, she also taught me a lot of technique skills that enabled me to build excellent circuits for my experiments. She is a friendly and warm-hearted person whom I'd like to work with. I also want to thank Dr. Henry Neeman, the director of the Oklahoma Supercomputer Center for Education and Research, for this help using Fortran and Mathematica on the Supercomputer.

I want to thank postdocs in the group, they are Dr. Santosh Kumar, Dr. Jiteng Sheng and Dr. Harald Kübler who worked with me on this project and gave tremendous helps. I also want to thank Dr. Christopher L. Holloway, and Dr. Joshua A. Gordon for collaborating on the geometry experiment. Thanks to Jonathon Sedlacek, Donald Booth, Jonathan Tallant, Arne Schwettmann, Renate Daschner, Yuanxi Chao, Akbar Jahangiri Jozani, Jin Yang, Tao Yang, Chris McRaven, Melinda Rupasinghe, and James Coker, who all helped a lot through discussions in the lab over these years. It has been an honor to have the following professors as the members of my graduate committee, Dr. Peter Barker, Dr. Eric R. I. Abraham, and Dr. Gregory A. Parker.

Thanks also should go to respectful professors from my alma mater, Wuhan University and Wuhan Institute of Physics and Mathematics in Chinese Academy of Sciences, who have helped me during my long journey to PhD degree. They are Dr. Kelin Gao, Dr. Hua Guan, Dr. Mang Feng, Dr. Xueren Huang, Dr. Liang Chen, Dr. Guiguang Xiong and Dr. Duanzheng Yao.

I thank my wife, Wushuang. Without her support from the home front, I would not have been able to do any of this. Aside from her encouragement to me for getting a PhD degree in physics, she has persevered intense work, even during the pregnancy and birth to my lovely daughter, Chenhan. She is my support and I thank her wholeheartedly.

Table of Contents

Abstract

An atom-based approach is presented to detect absolute microwave (MW) electric fields (E-fields). The approach uses Rydberg atoms in vapor cells at room temperature. The MW E-field measurements utilize a bright resonance prepared within an electromagnetically induced transparency (EIT) window. The large transition dipole moments between energetically adjacent Rydberg states enable this method to make traceable E-field measurements with a sensitivity that is several orders of magnitude higher than the current standard for MW E-field measurements. The method can be used to image MW E-field in the near field regime with a subwavelength resolution of $\lambda_{\mathrm{MW}}/650$, where λ_{MW} is the wavelength of the MW E-field. A high accuracy of 1% has been reached by minimizing the effects of the vapor cell geometry on the measured MW E-field. The dissertation also presents an alternative technique to perform the MW E-field measurement using dispersive properties of the EIT spectrum with a prism vapor cell. Recently, we applied a homodyne detection technique with a Mach Zehnder interferometer to achieve a new sensitivity limit for the MW E-field measurement, $\sim 3~\mu\mathrm{Vcm}^{-1}\mathrm{Hz}^{-1/2}$. The new sensitivity is one order of magnitude better than our prior best sensitivity presented in Ref. [Nat. Phys. 8, 819 (2012)]. The Rydberg atom-based method is promising to be a new standard for MW E-field measurements and to develop into portable devices in the field of MW technologies.

Chapter 1

Intoduction

1.1 Precision measurement and atom-based sensing

Atomic spectroscopy is essential for many precision measurements of physical quantities. The high performance of these measurements comes from the fact that precision atomic spectroscopy relates atomic structure to physical quantities [1] such as time, length, magnetic field etc. For example, magnetic field detection using properties of valence electron spin has reached a sensitivity below 1 fT $\text{Hz}^{-1/2}$ [2, 3]. By analysing the abundances of noble-gas isotopes (e.g. ^{39}Ar and ^{81}Kr) using the isotope energy shifts, a technique called atom trap trace analysis has been developed to identify the age of ancient glaciers and aquifers. This technique was able to accurately identify 120,000-year-old ice in Antarctica [4, 5]. By controlling atomic momentum transfer with stimulated Raman transitions, matterwave interferometry with ultracold atoms has been proposed to build highly sensitive gyroscopes, keeping a bias stability of < 70 μdeg h^{-1} with short-term noise of ~ 3 μdeg $\text{h}^{-1/2}$ [6, 7]. Such measurements are often referred to as atom-based sensing because properties of atoms are fundamentally involved in the measurements [1].

Besides its high performance, atom-based sensing provides an effective way to study the structure of atoms and molecules. In the process of atom-based sensing, the target physical quantities affect the spectral signal by modifying the atomic structure. For example, a magnetic field causes a Larmor procession of the valence electron of

alkali atoms. The Larmor procession leads to changes in the spectrum and can be used to determine the amplitude of the magnetic field with a high sensitivity [3]. The rigorous spectroscopic investigations through atom-based sensing may deepen the understanding of fundamental laws of physics. The valence electron in a polarized diatomic molecule has been proposed as a means to detect the potentially existing permanent electron electric diploe moment (eEDM) [8, 9]. The existence of a permanent eEDM would have profound implications on both fundamental symmetry violations and physics beyond the standard model. In the pursuit of searching for the permanent eEDM, new technologies, such as direct cooling and trapping diatomic molecules [10], have been under development to study the precision spectroscopy of cold molecules. Atomic and molecular precision spectroscopy can significantly improve atom-based sensing.

In addition, the definitions of certain physical quantities should be universal and standardized. As human activities are tightly connected around the globe in modern society, it is necessary for the measurements of certain physical quantities to be the same all over the world. In this way, international commerce and trade are facilitated without converting between diverse units of measurement; and standard units of physical quantities improve the efficiencies of scientific research activities. The most important physical quantities are defined as the international standard of units (SI units) such as length, mass, time, electric current,amount of substance, etc. Atomic spectroscopy is a good candidate to define some SI units because the properties of atoms or molecules enable measurements of these physical quantities to

be not only universal but also extremely precise. For example, time and frequency standards defined by the hyperfine transition of the ground state of the Cs atom are accepted as the definition of seconds. To support the the definitions of SI units, the committee on data for science and technology (CODATA) recommends values of fundamental physical constants [11, 12, 13], most of which are closely related to precision measurements with atomic spectroscopy.

Atom-based sensors benefit multiple aspects in human lives, such as environment, health care, communication, and entertainment. Thus, precision measurements using atoms and molecules attract the interest of people in different areas of academia and industry. Atomic clocks are used as primary standards for international time distribution services [1]. Atomic magnetometers are applied in health care to detect weak magnetic fields produced by the brain and heart, providing valuable information for diagnostics and research[14]. Atomic gyroscopes have been proposed as the core part of a sensitive inertial navigation system [15]. These atom-based sensing methods have surpassed the precision of conventional methods. Such atom-based sensors require either atoms in vapor cells at room temperature or cold atoms/molecules cooled and trapped by laser fields in high vacuum. Thus, these atom-based sensors rely on physics, especially atomic, molecular and optical (AMO) physics, and laser technologies.

The work presented in this dissertation applies atomic spectroscopy to measure microwave electric fields (MW E-fields). A Rydberg atom-based sensing method is demonstrated to measure the amplitude of MW E-fields. The method utilizes electromagnetically induced transparency (EIT) with Rydberg atoms in vapor cells at

room temperature. Owing to the huge transition dipole moment between Rydberg states, the Rydberg atom-based method leads to orders higher of magnitude greater sensitivity compared to conventional MW E-field probes. The method promises to be a revolutionary standard for MW E-field measurements.

1.2 Microwave electric field sensing

1.2.1 Motivation

The accurate measurement of MW E-fields is important for a wide range of applications, such as communication, meteorology, radar, entertainment, and medical care. These applications result in commodities and services valued over 1 trillion dollars each year. According to electromagnetic theory, the MW magnetic field (B-field) and electric field (E-field) are "born" together. The Maxwell equations reveal the relation between the B-field and E-field showing that the E-field can be calculated if the B-field is known. This relation is rather straightforward in free space, but not always simple in many cases. For example, in the near-field regime of a conducting material (typically a piece of metal), the E-field can be disturbed or distorted by the metal, while the B-field is barely affected by the metal, except for magnetic field shielding metals, such as nickel, cobalt and iron. In addition, the widespread use of magnetometry is limited by its detectable frequency range. A typical magnetometer detects magnetic fields at low frequencies, in the range of $<$ kHz, while measurements at high frequencies, e.g. in the GHz range are challenging [3]. Therefore, direct measurements of the MW E-fields are as important as the B-field measurements.

MW E-field sensing has been an active area of research since the electromagnetic wave was discovered. In the 1880s, Heinrich R. Hertz implemented dipole antennas to demonstrate the existence of electromagnetic waves [16]. Since then, dipole antennas have been a standard way to detect MW E-fields. The dipole antenna detects the MW E-field radiation and converts it into a direct current (DC) by applying resistive termination and filters. The amplitude or the power of the MW E-field is determined by measuring the value of the resulting voltage. This is the fundamental concept for measuring MW E-fields and to build traceable standards to calibrate those devices. The current traceable standards for MW E-field measurement are called the 'standard antenna' or 'standard field' methods [17, 18]. MW E-fields can be calibrated and determined to ~ 1 mVcm^{-1} [19, 20, 21, 22]. Modern variations on sensing MW E-fields for traceable standards are based on optical measurements for the electro-magnetic fields converted by the dipole antenna. These configurations can sense the MW E-field strengths down to $\sim 30~\mu$V cm^{-1} [23] with a sensitivity of ~ 1 mV cm^{-1}Hz$^{-1/2}$ [17]. The accuracy of the measurement is in the range of $4\% - 20\%$. The exact percentage depends on the frequency of the target MW E-fields and the exact method used for the standard.

Despite these achievements, the dipole antenna has several limitations. First, the probes of dipole antennas are made of metal and use metal transmission lines. Thus, the target MW E-fields are disturbed by the conducting material involved in the measurement. Second, although the spatial resolution has been improved by reducing the size of the probes, there are no subwavelength measurements for MW E-fields.

Third, complex and accurate design of antenna geometry is required for standard antennas. Due to the geometry and construction methods of the standard antenna, the system is subject to aging and manufacturing variations. Antenna variation in construction can reduce the reproducibility. Thus, it takes extra effort to maintain the accuracy and precision of the standard antenna. Fourth, there is currently no analytic solution for the MW E-field measurements, causing people to spend increasing effort on numerical calculations, which complicates the calibration process of standard antennas. Fifth, the minimum detectable E-field is relatively large because the probe needs substantial strength of field to make an accurate measurement. The combination of these limitations impacts the ability to conduct traceable measurements for MW E-fields. As a result, usually a few large laboratories have the resources and time to build and maintain standard antennas for MW E-field measurements, such as the National Institute of Science and Technology (NIST) in the United States.

In addition, it is difficult for dipole antenna to detect a MW E-field in the far-infrared (FIR) regime. The shape of a dipole antenna, or a probe, changes for different applications and frequencies. This is because the size of the probe depends on the target frequency. The size of a typical antenna is half of the wavelength of the MW E-field. When the target MW E-field is in FIR regime, the required antenna to probe the MW E-field is too small to practically produce. This leaves a critical gap in one of the most rapidly developing bands of the electromagnetic spectrum. Considering the advantages of precision measurements using atomic spectroscopy, MW E-field measurements can potentially be substantially improved by using atom-based sensing.

1.2.2 Background of atom-based sensing on E-fields

B-field measurements have been motivated by atom-based sensing, where it is now possible to achieve a sensitivity in the fT Hz$^{-1/2}$ regime. In contrast, atom-based methods for absolute E-field measurement has changed little over the same period of time, creating a great desire to the current E-field standard and measurements with an atom-based method. Precise, atom-based methods for absolute E-field measurement are clearly of scientific and practical interests. The work in the dissertation is to explore the possibility using Rydberg atoms to perform such measurements for E-fields.

Compared to previous E-field standards using atoms [24, 25, 26, 27], this method measures E-fields using Rydberg atoms rather than ground-state atoms. Due to the large polarizability, Rydberg atoms are highly sensitive to E-fields. That is, a response to E-field for Rydberg atoms is comparably stronger than ground-state atoms, because a Rydberg electron is relatively weakly bound, compared to a valence electron for ground-state atoms. Different methods involving Rydberg atoms have been proposed to measure DC E-fields by utilizing the large polarizabilities of Rydberg atoms. For example, Herrmann *et al.* experimentally proposed a spurious E-field measurement as small as ~ 80 mVcm^{-1} using Cs atomic beams [28]; a minimum DC E-field measurement of 20 μVcm^{-1} has been achieved by using krypton atoms in Rydberg states [29]; by utilizing the fluorescence imaging technique, DC E-fields are measured around 10 Vcm^{-1} [30]. The large polarizabilities of Rydberg atoms have also been used for RF modulation via a giant electro-optic effect that is Kerr non-linearity [31]. For MW E-fields in the millimeter regime, resonant transitions have been used

to detect small AC E-fields in atomic beams and masers [32, 33].

These methods open the way to atom-based E-field sensing, but an atom-based E-field standard remains challenging. First, such works have focused on DC E-field or low frequency AC E-field that have not reached to the MW regime, $\sim$ GHz regime. The first AC E-field measurement using Rydberg atoms detected an E-field as large as ~ 7 Vcm^{-1}, at the frequency of 15 MHz [34], which in principle measures a DC field with modulation in the MHz regime. Second, the methods described above, such as Rydberg atom masers and atomic beam methods, require an ultrahigh vacuum system and even coupling of the radiation into a high-Q millimeter wave cavity in the apparatus. Consequently, although Rydberg atom masers and atomic beam methods are very sensitive and accurate, they are complex and hard implement for many practical applications [32, 33]. Third, these methods also rely on an antenna that converts the millimeter wave field, transferring the signal to the atoms, in order to be read out. The antenna pick-up method reintroduces the problems of the conventional antenna into the sensor.

The impediment to widely applying many of the atom-based methods listed here to electrometry is the technical complexity of the setups. To build an atom-based standard that is practically applicable for MW electrometry, more improvements on the simplicity and sensitivity are needed. In this dissertation, a Rydberg atom-based method is described to detect MW E-fields in thermal vapor cells. The method is free of ultrahigh vacuum, significantly reducing the volume of the setup. The setup can perform MW E-field measurements with several orders of magnitude higher in

(a)

Horn Antenna

Vapor Cell $\quad \Omega_C \quad$ Detector

Ω_P

Dichroic
Mirror

(b)

n D$_{5/2}$ $\qquad$ MW

(n+1) P$_{3/2}$

508-510 nm

6P$_{3/2}$

852 nm

6S$_{1/2}$
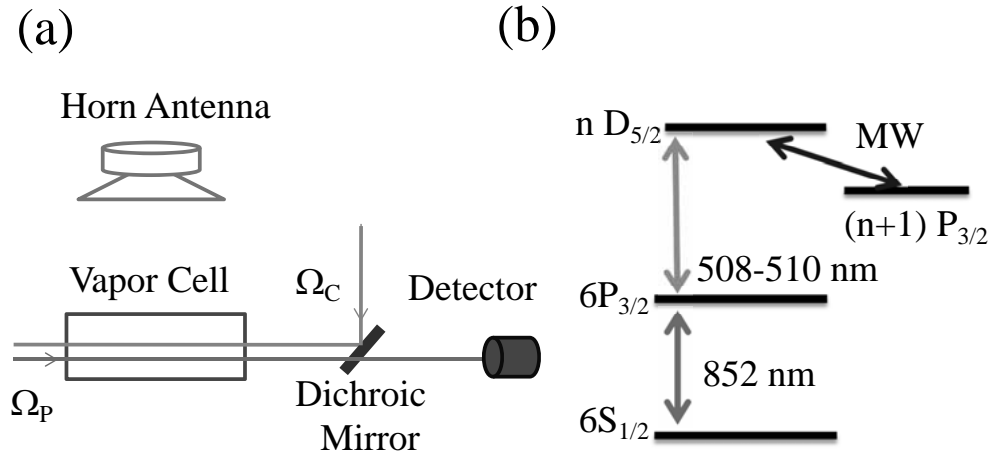
Figure 1.1: (color online) (a) The typical experimental setup for MW
E-field measurement. The MW E-field is generated by a horn antenna.
The probe and coupling lasers are in a counter-propagating gemometry
interacting in a vapor cell filled with Cs atoms. The signal of the probe
laser is captured by an photodiode detector. (b) The transition diagram
of ^{133}Cs used for the MW E-field measurement. The probe and coupling
lasers excite the atom into a Rydberg state, while the MW E-field couples
two adjacent Rydberg levels.

sensitivity and accuracy than the current MW E-field standard. The atom-based measurement will calibrate MW E-fields to the spectral properties of Rydberg atoms, enhancing stability and reproducibility. Thus, the setup of the method can be developed into portable and self-calibrated devices for MW E-field standards.

1.2.3 MW E-field sensing using Rydberg atoms at room temperature

The MW E-field measurement described in this dissertation relies on two features of Rydberg atoms. One is resonant transitions between Rydberg states, while the other is the associated large transition dipole moments between neighboring, or nearby, Rydberg states that scales as n^2. For the Rydberg atom-based eletrometry, the amplitude of a MW E-field is determined by the MW coupling strength between two closely lying Rydberg states,

$$\Omega_{MW} = \frac{\vec{E} \cdot \vec{\mu}_{MW}}{\hbar}. \tag{1.1}$$

The coupling to the MW E-field, Ω_{MW}, known as Rabi frequency, will cause a splitting in the EIT window. The splitting is the Autler-Townes splitting (AT splitting) that is proportional to the Rabi frequency of the MW E-field, Ω_{MW}. MW dressing of interaction potentials and AT splitting in Rydberg EIT was demonstrated in an ultracold gas [35]. Here, with Rydberg EIT in vapor cells at room temperature, the target MW E-field couples two adjacent Rydberg states, generating an observable AT splitting in spectrum.

In this dissertation, the atom-based standard and probe for MW E-fields are performed with one type of heavy alkali atom, ^{133}Cs atoms in vapor cells. With a

modest experimental setup, the alkali atoms are prepared partially in Rydberg states in a vapor cell. Due to the presence of a strong resonant coupling laser beam, the probe laser beam is transmitted through a normally absorbing atomic vapor, resulting in an EIT window in the absorption of the probe beam [36, 31]. If the coupling laser beam is in a counter-propagating direction of the probe laser beam, a spectrally narrow EIT window can be created in an atomic vapor because the counter-propagation geometry greatly reduces the Doppler broadening. When a MW E-field is on resonance with an adjacent Rydberg state, a narrow absorption feature is induced, causing AT splitting in the transmission lineshape that can be observed as a function of probe laser frequency. The strength of MW E-fields on the EIT lineshape is determined by equation 1.1.

The Rydberg atom-based MW E-field measurement uses each gaseous Rydberg atom in the vapor cell as a probe for the MW E-field. This atom-based method can at least overcome several shortcomings of conventional dipole antennas. The atom probe is free of metal that leads to disturbance to the target MW E-fields. The atomic probe will not suffer from aging or construction variations because the atoms are the same everywhere and all the time. The amplitude of the MW E-field is calibrated by the property of Rydberg atoms that are stable and extensively studied. There is no need to build another probe to calibrate the MW E-field as the conventional MW standard does. This is the reason why the atom-based method is self-calibrated for MW E-field measurements.

Due to the large transition dipole moments between neighboring Rydberg states, the sensitivity of the Rydberg atom-based MW E-field sensing is high. For the atomic

spectrum, the AT splitting can be large even when the MW E-field is weak. As an example to demonstrate the sensitivity of the MW E-field measurement using this method, let us consider the case when a MW E-field is on resonance with the transition of ^{133}Cs $52D_{5/2} \leftrightarrow 53P_{3/2}$. This transition is in the C band of the microwave spectrum and has the frequency of 5.05 GHz. A Rabi frequency, Ω_{MW}, of 1 MHz is induced by a MW E-field amplitude of only $\sim 450~\mu Vcm^{-1}$ or an intensity of only $\sim 0.26~nWcm^{-2}$. This is equivalent to 1 nW of MW E-field shining on an area as large as an US quarter coin. This small amount of the MW E-field power is usually hard to observe by a dipole antenna. However, one can utilize the Rydberg EIT method to detect the AT splitting of the transition caused by this small MW E-field. With stabilized diode lasers and vapor cells at room temperature, the MW E-field results in a signal that is technologically easy to observe in the atomic spectroscopy.

Despite the high sensitivity to MW E-fields, there are several factors that limit the ability to detect a lineshape change of the EIT transmission window. These factors include the laser linewidths, transit time broadening, Doppler mismatch between the probe and coupling lasers, and dephasing rates of the Rydberg states involved in the EIT process. The dephasing rates are mostly due to collisions, blackbody radiation and spontaneous emission. The details of these limiting factors are discussed later in the dissertation. By carefully studying these limiting factors, it is possible to reach the shot noise limit where MW E-field can be detected as small as $\leq 10\,pV\,cm^{-1}$.

The previous work in our lab has shown that the MW E-field can be measured with an angular resolution of 0.5º for a vector MW E-field [37] and a high sensitivity

8 μVcm^{-1}Hz$^{-1/2}$ [38]. The measurement barely disturbs the MW E-field because the probe is a dilute gas of atoms in a vapor cell. This feature is promising to perform MW E-field subwavelength measurements in near field regime. We show that MW E-field spatial distributions can be mapped in near field regime with a high resolution, $\sim \lambda_{\mathrm{MW}}/650$ [39, 40], where λ_{MW} is the wavelength of the MW E-field. The dissertation will also show the method to measure MW E-fields with a sensitivity an order higher in amplitude ~ 3 μVcm^{-1}Hz$^{-1/2}$. The dissertation will present that the accuracy of the MW E-field measurement is less than 1%. Moveover, the Rydberg atom-based method can cover a large frequency range, 1 GHz $\sim$ 1 THz. Considering the property of self-calibration, the high sensitivity, the high accuracy, and the coverage of a large frequency range, this Rydberg atom-based MW E-field sensing is a promising candidate for a new standard for MW E-fields.

1.3 Thesis outline

In chapter 2, the basic theory that is important to understand the work described in this thesis is presented. First, the EIT theory and calculations involving Rydberg atoms and MW E-field is presented. The theory of EIT includes the Doppler effect because the atoms that are involved in the interaction are in a Maxwell distribution in velocity in a vapor cell at room temperature. Next, the properties of Rydberg atoms are summarized, including the scaling properties of Rydberg atoms, the quantum defect that can be used to calculate the transition wavelengths of MW E-field, and the transition dipole moments which are calculated using the electronic wavefunctions

of Rydberg atoms.

In chapter 3, the prerequisites of the experiment are described in detail. This includes the manufacture of vapor cells and the frequency stabilization of the probe and coupling lasers. Most of the vapor cells used in the experiment were made in the glass workshop at the University of Oklahoma (OU) because of the unique requirements of the experiments, such as geometry, size and composition of the vapor cells. There are two types of frequency stabilization used for the lasers. One is the spectral locking involving the absorption of Cs D_2 transition and Rydberg EIT. The other is the Pound-Drever-Hall method that enables both the probe and coupling lasers to lock to an ultra-low expansion reference cavity.

Chapter 4 discusses our investigation of subwavelength imaging with a spatial resolution of $\lambda_{\mathrm{MW}}/650$ or 66 μm at 6.9 GHz. We show the ability for Rydberg atoms to image MW E-field at subwavelength regime by mapping in a standing wave and a near-field region above a coplanar waveguide (CPW). The MW E-field resolutions are ~ 50 μVcm^{-1}. Our experimental results agree with finite element calculations of test E-field patterns. The results we demonstrate here show the promise of a wide range of applications for the Rydberg atom-based MW E-field detection, particularly in characterizing metamaterials and small MW circuits, including antennas.

Chapter 5 presents a systematic investigation on the effect of vapor cell geometry on Rydberg atom-based measurements of MW E-fields. The accuracy of the MW E-field measurement depends on the geometry of the vapor cell which is the ratio of the vapor cell size D of the cubic Pyrex vapor cells used for the measurements

to the MW E-field wavelength λ_{MW}, i.e. D/λ_{MW}. We experimentally show that the accuracy is greater than the current methods in the frequency range 10-30 GHz and is not currently limited by the vapor cell geometry provided $D/\lambda_{\mathrm{MW}} < 0.1$.

Chapter 6 introduces a method to measure MW E-fields using atoms in a prism-shaped vapor cell using Rydberg EIT. The MW E-field induces changes in the index of refraction of the vapor resulting in deflection of the probe laser beam as it passes through the prism-shaped vapor cell. The deflection angle is measured by a position sensitive detector. We measured a minimum MW E-field of $8.25\mu\mathrm{Vcm}^{-1}$ with a sensitivity of ~ 46.5 $\mu\mathrm{Vcm}^{-1}\mathrm{Hz}^{-1/2}$. The experimental results agree with a numerical model that includes dephasing effects. We also discuss possible improvements to obtain higher sensitivity for MW E-field measurements as well as the applications for the index of reflection measurements which is MW E-field induced.

Chapter 7 reports the MW E-field measurements aiming at eliminating one of the main factors limiting sensitivity of MW E-field using Rydberg atoms in vapor cells, the noise of the probe laser. We apply a homodyne detection technique using a Mach-Zehnder interferometer to achieve a new sensitivity limit for the measurement of MW E-fields, $3 - 5\mu\mathrm{Vcm}^{-1}\mathrm{Hz}^{-1/2}$. The new sensitivity is almost one order of magnitude higher than the previous results reported in Ref. [41]. We also report on the homogeneous dephasing effects caused by transit time broadening, collision broadening, and the lifetime of Rydberg atoms which we can now directly observe. We show that these dephasing effects are the fundamental limiting factors that determine the shot noise limit.

In Chapter 8, we summarized the work in the dissertation and discuss the shot noise limit for the atom-based MW E-field sensing. The sensitivity can be several pV cm^{-1} Hz$^{-1/2}$ with shot noise limited performance. These factors are basically dephasing rates in the measurement including collisions between transit time broadening, lifetime of Rydberg atoms, and etc. The outlook is also given in this chapter.

Chapter 2

Theory on EIT and Rydberg Atoms

2.1 Introduction

In this chapter, the theoretical basis for MW E-field sensing with Rydberg atoms is described in detail. First, the theory of electromagnetically induced transparency (EIT) is presented for a 4-level ladder-type system, in which the Doppler effect and dephasing factors are included. Next, the properties of Rydberg atoms are presented, including the quantum defect that is crucial to determine the energy levels of Rydberg atoms. Then, calculations for transition dipole moments are described. The wavefunctions of the Rydberg states are numerically calculated using an empirical potential model.

2.2 Electromagnetically induced transparency

2.2.1 Introduction to typical EIT systems

EIT, firstly termed by S. E. Harris and co-workers in 1990 [42], describes a phenomenon of quantum interference where an initially opaque atomic media is rendered to be transparent to probe laser light in the presence of a coupling laser that modifies the probe absorption. This phenomenon usually takes place in 3-level systems. Fig. 2.1 shows two types of EIT systems; one is Λ-type and the other is ladder-type or Ξ-type. In such EIT systems, there are two long-lived energy levels and one intermediate energy level with a relatively short lifetime. The Λ-type EIT is

frequently studied, in which the two long-lived states are typically two components of the ground state, e.g., hyperfine levels of an alkali atom. The other EIT system is the ladder-type EIT system (Ξ-type system) that usually has a Rydberg state as one of the long-lived levels. Such an EIT system is also called Rydberg EIT. Through the EIT process, the atomic media is coherently prepared in a dark state that usually takes place with a weak probe field and a strong coupling field.

The full width half maximum (FWHM) of an EIT window is determined by the coherence relaxation time between the two long-lived states rather than the spontaneous decay of the relatively short-lived state. The transition between the two long-lived states is dipole forbidden, leading to a long coherence relaxation time. Thus, the FWHM of an EIT window can be orders of magnitude narrower in frequency compared to the natural linewidth of the probe transition. Such an EIT system is a good candidate to perform sensitive frequency measurements with a high resolution because of its narrow transmissive spectral features [27]. One of the successful examples is the atomic clock. A technique called coherent population trapping (CPT) has been developed to build atomic clocks using alkali atoms as absolute frequency references [43]. An advantage of the CPT technique is that the width of the transition can be as narrow as 1×10^{-3} Hz for a cesium CPT clock, resulting in a stability of $< 1\times10^{-12}$ [44]. In addition, the CPT setup of atomic clocks is free of large vacuum systems; therefore, its size can be minimized. A CPT atomic clock has been fabricated as small as 1 cm^3 while keeping a long term stability with less than 30 mW electrical power [45], leading to a wide variety of commercial and military systems with portable, battery-powered
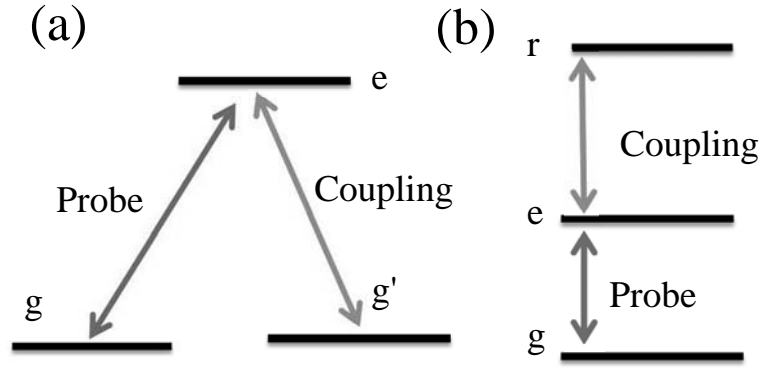
Figure 2.1: The energy levels of two typical electromagnetically induced transparency (EIT) systems (a) The Λ-type system. g and g′ are the hyperfine levels of the ground state which are coupled to an excited state e by two laser fields. The ground states are stable and have a longer lifetime than the excited state. A weak probe beam is on resonance with the g $\leftrightarrow$ e transition, while a strong coupling beam is on resonance with the g′ $\leftrightarrow$ e transition. (b) The ladder-type (or Ξ-type) EIT system. It consists of a ground state, g, an excited state, e, and an higher excited state which usually is a Rydberg state, r. The g and r states are long-lived compared to the state e. The weak probe laser field is on resonance with the g $\leftrightarrow$ e transition and the strong coupling laser field is on resonance with the e $\leftrightarrow$ r transition.

19

units for atomic-level timekeeping. Given the advantages and achievements of using EIT to perform atom-based measurements, this dissertation describes how to apply an EIT system to perform absolute MW E-field measurements using Rydberg atoms in vapor cells at room temperature.

2.2.2 The calculation of 4-level EIT-like system

The MW E-field sensing described in this dissertation is performed with a ladder-type EIT system. The system has two features that are different from typical EIT systems described in Section 2.2.1. One feature is that there is one more energy level compared to a typical 3-level EIT system. Coupling a fourth level to the EIT system with a MW E-field induces the probe laser beam to be absorbed on resonance, resulting in a "bright state". The bright state causes AT splitting in the probe absorption spectrum. The other feature is that the probe laser is relatively strong compared to the coupling laser. The transition dipole moment for the coupling transition is $< 1\%$ of the transition dipole moment for the probe transition. To obtain an EIT window with a high enough signal-to-noise ratio (SNR) for the MW E-field measurements, the power of the probe laser is relatively strong compared to the power of the coupling laser, which drives the EIT system out of the weak probe regime.

With the two features described above, a full calculation for the 4-level EIT system is performed to simulate the results of MW E-field measurements without applying the weak probe approximation as in a typical EIT system. Fig. 2.2(a) shows the energy levels of a typical 4-level EIT system. For generality, $|i\rangle = |1\rangle, |2\rangle, |3\rangle$

and $|4\rangle$ represent the ground state, the intermediate state and two Rydberg states, respectively. The probe beam is on resonance with the $|1\rangle \leftrightarrow |2\rangle$ transition, and the coupling beam is on resonance with the $|2\rangle \leftrightarrow |3\rangle$ transition. The MW E-field is on resonance with the transition between the two Rydberg states, $|3\rangle \leftrightarrow |4\rangle$. The Hamiltonian of the system is expressed as

$$\mathbf{H} = \mathbf{H}_0 + \mathbf{H}_I. \tag{2.1}$$

$\mathbf{H}_0$ is the unperturbed Hamiltonian,

$$\mathbf{H}_0 = \sum_i \hbar \omega_i |i\rangle \langle i|, \tag{2.2}$$

where $\omega_i = \omega_P$, ω_C, and ω_{MW} represent the angular frequencies of the probe laser, the coupling laser, and the MW E-field, respectively. $\mathbf{H}_I$ is the interaction Hamiltonian involving the probe, the coupling, and the MW transitions. It is described as,

$$\mathbf{H}_I = \frac{\hbar}{2}[(\Omega_P e^{-i\omega_p t} |1\rangle \langle 2| + \Omega_C e^{-i\omega_c t} |2\rangle \langle 3| + \Omega_{MW} e^{-i\omega_{MW} t} |3\rangle \langle 4|) + h.c.], \tag{2.3}$$

where Ω_P, Ω_C, and Ω_{MW} are Rabi frequencies of the probe, the coupling, and the MW E-field, respectively. With the standard rotating wave approximation, the Hamiltonian is,

$$\mathbf{H} = \frac{\hbar}{2}[2\Delta_P |2\rangle \langle 2| + 2(\Delta_P + \Delta_C) |3\rangle \langle 3| + 2(\Delta_P + \Delta_C + \Delta_{MW}) |4\rangle \langle 4|]$$
$$- \frac{\hbar}{2}[(\Omega_P |1\rangle \langle 2| + \Omega_C |2\rangle \langle 3| + \Omega_{MW} |3\rangle \langle 4|) + h.c.], \tag{2.4}$$

where Δ_P, Δ_C, and Δ_{MW} are the detunings of the probe, the coupling and the MW E-field, respectively. The Hamiltonian can be written in matrix form,

$$H = \frac{\hbar}{2} \begin{pmatrix} 0 & -\Omega_p & 0 & 0 \\ -\Omega_p & 2\Delta_c & -\Omega_c & 0 \\ 0 & -\Omega_c & 2(\Delta_c + \Delta_p) & -\Omega_{MW} \\ 0 & 0 & -\Omega_{MW} & 2(\Delta_c + \Delta_p + \Delta_{MW}) \end{pmatrix}. \tag{2.5}$$

21

The time evolution of the density matrix operator, in the presence of decay, is obtained from the Liouville equation,

$$\frac{d}{dt}\boldsymbol{\rho} = -\frac{i}{\hbar}[\mathbf{H}, \boldsymbol{\rho}] + L, \tag{2.6}$$

where ρ is the density operator and the L is the Liouville-von Neumann matrix related to the decay or decoherence of the system. It can be described as

$$L_{ij} = \frac{\Gamma_{ij}}{2}(2\sigma_{ji}\rho\sigma_{ij} - \sigma_{ii}\rho - \rho\sigma_{ii}), \tag{2.7}$$

where Γ_{ij} is the decay rate from state $|i\rangle$ to state $|j\rangle$; σ_{ij} is the projection operator from state $|j\rangle$ to state $|i\rangle$ [46]. For example, in an EIT system, $6S_{1/2} \leftrightarrow 6P_{3/2} \leftrightarrow 52D_{5/2}$ of a ^{133}Cs atom with a MW E-field coupling the $52D_{5/2} \leftrightarrow 53P_{3/2}$ transition, the primary sources of relaxation are the spontaneous emission of the intermediate state, $6P_{3/2}$, $\Gamma_{12} = 2\pi \times 5.2$ MHz, and the Rydberg state spontaneous decay including blackbody radiation for $52D_{5/2}$, $\Gamma_{23} \approx 2\pi \times 3.4$ kHz and $\Gamma_{34} \approx 2\pi \times 1.6$ kHz for $53P_{3/2}$ [47]. The dephasing factors that depend on the experimental setup are also considered in the simulation, including transit time broadening (Γ_t), Rydberg-ground state atom collisional decay (Γ_{coll}), laser dephasing (Γ_e), and magnetic field dephasing (Γ_m). The transit time broadening, Γ_t, and laser dephasing, Γ_e, contribute to Γ_{12} and Γ_{23}; Rydberg-ground state atom collisions, Γ_{coll}, contributes to the decoherence between the Rydberg state and the ground state, Γ_{13}; and magnetic field dephasing, Γ_m, contributes to dephasing of the two Rydberg states, Γ_{23} and Γ_{34}.

The transit time broadening rate Γ_t and the collision rate Γ_{coll} play particularly important roles in the MW E-Field measurements. The atoms see the lasers as a

pulse of light whose temporal width is determined by the time it takes the atoms to pass through the laser beams. This leads to a broadening of the spectroscopic signals, referred as transit time broadening. It can be described by,

$$\Gamma_t \sim 0.225 \frac{v}{d}, \tag{2.8}$$

where v is the velocity of the atoms and d is the diameter of the laser beam [48]. Collisions between atoms in the vapor cell are one of the most important contributions to the dephasing rate. Collisions involve Rydberg atoms, ground state atoms and intermediate state atoms. The collisional rate, Γ_c, is determined by the cross section for these collisions, σ, velocity of the atoms in the gas, v, and the density of the collision particles, ρ. Γ_c can be written in terms of these variables as,

$$\Gamma_c = \sigma v \rho, \tag{2.9}$$

where σ depends on the long range interaction potential through its appropriate leading order multipolar coefficient and the kinetic energy of the collision [49]. In addition, the diagonal elements of transition matrix satisfy the condition,

$$\rho_{11} + \rho_{22} + \rho_{33} + \rho_{44} = 1. \tag{2.10}$$

To evaluate the steady state solutions, the right hand side of Equation. 2.6, is set to equal to zero, $d\rho/dt = 0$.

In the MW E-field sensing experiment, the probe and coupling laser beams are in a counter-propagating geometry to minimize the effect of Doppler broadening for the Rydberg EIT. The atoms are contained in a vapor cell at room temperature.
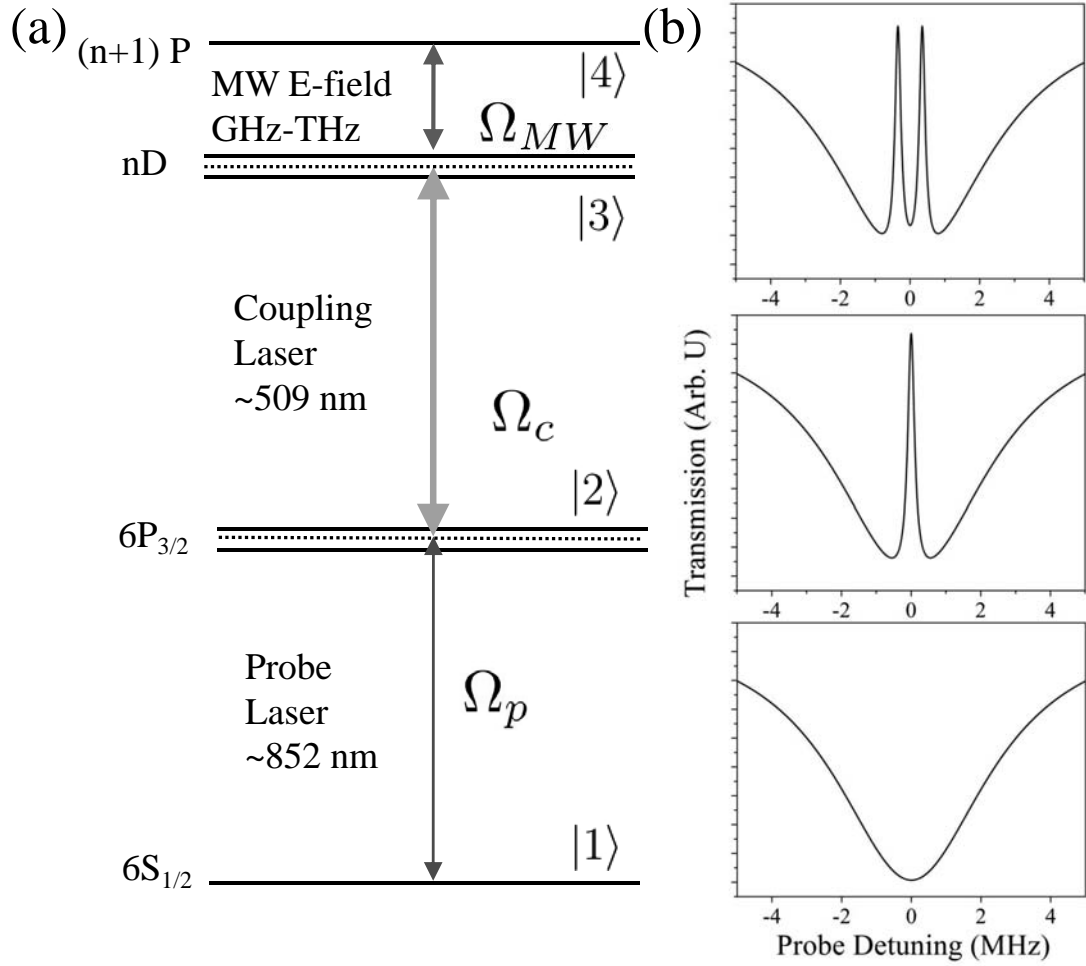
Figure 2.2: (a) The diagram of a typical excitation scheme for atom-based MW E-field sensing using Cs Rydberg atoms in vapor cells. (b) The lower panel shows the absorption spectrum of the D_2 transition with no coupling laser or MW E-field present. The middle panel is the spectrum with a resonant coupling laser. An EIT windows appears at the center of the absorption spectrum. The upper panel shows the spectrum in the presence of a MW E-field coupling two adjacent Rydberg levels. A narrow absorption feature appears at the center of the EIT window.

There is still a residual Doppler effect because the lasers have different wavelengths, forming a wavelength mismatch condition [50]. The residual Doppler effect results in a broadening in the spectrum, $(k_C - k_P)\mu \sim 2\pi \times 3.5$ MHz, where k_C and k_P are the wave vectors of the coupling and probe lasers, respectively; and $\mu = \sqrt{2k_BT/M}$ is the most probable velocity of the atoms, in which M is the mass of one atom, T is the temperature, and k_B is the Boltzmann constant. In the counter-propagating scheme of probe and coupling laser beams, the detunings of the probe and the coupling lasers are modified as,

$$\Delta_P \rightarrow \Delta_P + k_P v,$$
$$\Delta_C \rightarrow \Delta_C - k_C v. \tag{2.11}$$

The moving atoms in the vapor cell have a Maxwell-Boltzmann distribution of velocities. The Maxwell-Boltzmann distribution is

$$f(v) = \frac{1}{\mu\sqrt{\pi}} e^{-\frac{v^2}{\mu^2}}, \tag{2.12}$$

where $f(v)$ is the fraction of atoms with velocity v. When the Doppler effect is applied in the calculation, the matrix element of ρ_{12} is expressed as,

$$\rho_{12} = \int \rho_{12}(v) \frac{1}{\mu\sqrt{\pi}} e^{-\frac{v^2}{\mu^2}} dv. \tag{2.13}$$

where $\rho_{12}(v)$ is obtained by solving the steady state condition of Equation 2.6 that includes the residual Doppler effect. The integration over the whole velocity range will give ρ_{12}. The transmission of the probe laser is proportional to the imaginary part of ρ_{12}. The dielectric response of the atomic media to the probe field is determined by the electric polarization, P. The linear polarization is related to the amplitude

25

(E_0) of the probe field and can be expressed as $P = \epsilon_0 \chi E_0$, where ϵ_0 is the electric permittivity of free space and χ is the electric susceptibility of the atomic media. The susceptibility is given by,

$$\chi = \frac{N\mu_{12}^2}{\epsilon_0 \hbar}\rho_{12} = \chi' + i\chi'', \qquad (2.14)$$

where N is the number of atoms participating in the interaction, χ' and χ'' are the real and imaginary part of the complex susceptibility respectively. χ' gives the dispersive response of the atomic media while χ'' gives the absorptive response. The absorption relates to the transmission spectrum while the dispersion relates to the index of refraction. Both of the absorptive and the dispersive properties are used to measure amplitudes of MW E-fields in this dissertation.

Fig. 2.2 (b) shows the calculated transmission of the 4 level system of Cs atoms in a vapor cell with $\Omega_P = 2\pi \times 1$ MHz, $\Omega_C = 2\pi \times 0.5$ MHz, and $\Omega_{MW} = 2\pi \times 0.7$ MHz. The calculation includes the sources of relaxation described in this section. To demonstrate the differences between the one-photon, two-photon, and three-photon processes, the transmission spectrum is calculated in the presence of of one-photon, two-photon, and three-photon fields, respectively. A single field, Ω_P, gives an absorption spectrum, while an EIT window appears in the presence of a two-photon field, Ω_P and Ω_C. When a MW E-field is on resonance with two neighbouring Rydberg states as the third photon, Ω_{MW}, an AT splitting is generated, which is determined by the amplitude of the MW E-field.

2.3 Rydberg atoms

2.3.1 Fundamental properties of Rydberg atoms

Rydberg atoms refer to atoms in which at least one electron is excited into a high energy state, i.e., a state of high principal quantum number n. The term "Rydberg atom" is in honor of J. R. Rydberg, who introduced an empirical formula to determine the energy levels of highly excited atoms [51]. The general interest of Rydberg atoms originates from the fact that Rydberg atoms have exaggerated properties. For example, Rydberg blockade effects, which result from energy shifts due to long-range interactions between Rydberg atoms, can be utilized for quantum information processing using collective states of mesoscopic atomic ensembles [52, 53]. A trilobite Rydberg molecule dimer, consisting of a ground state atom and a Rydberg atom, has a thousand-Debye permanent electric dipole moment [54]. Because the highly excited electron of an Rydberg atom is loosely-bounded to the ionic core, Rydberg atoms are extremely sensitive to external E-fields compared to valence states, which makes them promising for electrometry [29].

The properties of Rydberg atoms generally scale with the principal quantum number n. Table 2.3.1 shows Rydberg atom properties including binding energy, level spacing, orbital radius, transition dipole moment, spontaneous decay, etc. These scaling properties are beneficial for MW E-field measurements. The transition dipole moment scales as n^2, leading to a high sensitivity for MW E-field detection by utilizing large n of Rydberg states. In addition, high-lying Rydberg atoms have narrow natural

Quantity	Expression	Scaling
Binding energy	$E_n = -R_0 c n^{-2}$	n^{*-2}
Radius	$\langle r \rangle = a_0 n^2$	n^{*2}
Level spacing	$\Delta = E_n - E_{n-1}$	n^{*-3}
Dipole moment	$d = \langle nl \,|\, er \,|\, nl' \rangle$	n^{*2}
Radiative lifetime	$\tau_r = 1.43 n^3$	n^{*3}

Table 2.1: The properties of Rydberg atoms that are used in this dissertation and the scaling with the effective principal quantum number, n^*. The expression is taken from Ref [51]. The physical quantities are in SI units. (R_0 is the Rydberg constant, c is the speed of light in vacuum, and l is the quantum number of angular momentum.)

linewidth because the lifetime of Rydberg atoms scales as n^3. In an ideal case, when the spectrum is free of the Doppler effect and an atom is put into a superposition of the ground state and a Rydberg state, a dark state is formed in the absorption spectrum with a spectral linewidth of the Rydberg atoms <10 kHz at n=50 for a Cs atom. This linewidth is much narrower than the D_1 or D_2 transition of alkali atoms ($\sim$5.2 MHz for D_2 transition of Cs atoms [55]). The large transition dipole moment and the narrow natural linewidth lead to a high resolution for MW E-field sensing.

In the MW E-field sensing experiment, the most important features are the Rydberg energy levels and the transition dipole moments between Rydberg states. To estimate the wavelengths of MW E-fields, it is necessary to study the energies of Rydberg levels. The energy levels can be calculated using the quantum defect. In addition, the transition dipole moment between Rydberg states is crucial to estimate the sensitivity of the MW E-field measurement. In order to calculate the transition

28

dipole moments, the wavefunctions of Rydberg states are calculated using a numerical model coded with FORTRAN. The following sections give the details of calculations for Rydberg energy levels and transition dipole moments between Rydberg states.
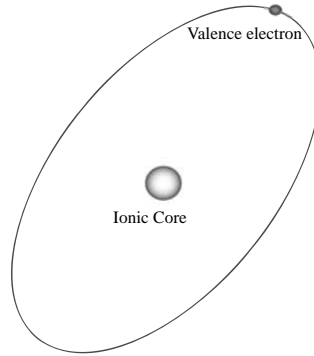
Figure 2.3: A diagram of an atom in a Rydberg state. The center is the ionic core and the highly excited electron orbits around the core.

2.3.2 Quantum defect

The energy levels of Rydberg atoms are calculated using quantum defect theory [51]. When the valence electron is far away from the ionic core, the atom is similar to a hydrogen atom with a net electric charge of $+1$ e, where e is the elementary charge. Because of the existence of the electrons surrounding the ionic core, the binding energy of alkali Rydberg atoms are modified from those of hydrogen atoms. As shown in Figure 2.3, a typical Rydberg atom consists of an ionic core and a highly-excited valence electron. The nuclear charge of the core is screened by the electron cloud of the core, such that the ionic core acts as an effective nucleus for the valence electron. For example, an ionic core of a ^{133}Cs atom in Rydberg states contains 55 protons,

Table 2.2: Quantum Defect of Cesium atoms.

	$S_{1/2}$	$P_{3/2}$	$D_{3/2}$	$D_{5/2}$
δ_0	4.0493527	3.5589599	2.4754562	2.4663091
δ_2	0.238100	0.392469	0.009320	0.014964
δ_4	0.24688	-0.67431	-0.43498	0.45828
δ_6	0.06785	22.3531	-0.76358	0.25489
δ_8	0.1135	-92.289	-18.0061	-19.6900

78 neutrons and 54 electrons. Thus, a ^{133}Cs Rydberg atom is expected to behave similarly to a hydrogen atom except for the ionic core that causes the quantum defect. The inner electrons of the ionic core do not perfectly screen the nuclear charge. The valence electron has a small possibility to penetrate the electron cloud around the nucleus. The orbit can penetrate into the core. Because of the core penetration of the valence electron, the wavefunction shifts towards the ionic core. The shift leads to a modification of the binding potential. Therefore, the energy levels of Rydberg atoms are shifted and can be characterized by a modified hydrogen energy formula known as Rydberg-Ritz formula,

$$E_{nlj} = -hc\frac{R_{Cs}}{(n - \delta_{nlj})^2},\qquad(2.15)$$

where R_{Cs} is the Rydberg constant for Cs atoms, δ_{nlj} is the quantum defect, and $n^* = n - \delta_{nlj}$ is the effective principal quantum number. This empirical formula leads to Rydberg energy levels with an accuracy of ≤ 1 MHz [53].

In the calculation of the quantum defects δ_{nlj}, the following empirical formula is applied,

$$\delta_{nlj} = \delta_0 + \frac{\delta_2}{(n - \delta_0)^2} + \frac{\delta_4}{(n - \delta_0)^4} + \frac{\delta_6}{(n - \delta_0)^6} + \frac{\delta_8}{(n - \delta_0)^8} + \cdots.\qquad(2.16)$$

In this equation, δ_0, δ_2... are dependent on l, and j. For Cs atoms, these parameters have been measured and listed in Ref. [56]. Table 2.2 shows the values of the quantum defects for the states used in the experiments that were used to determine the transition wavelength for both coupling laser and MW E-fields. The values of the quantum defect, δ_0, decrease when the angular momentum, l, increases.

The orbit of the valence electron becomes more and more circular when increasing the angular momentum, l, because the overlap with the inner-electron wavefunction becomes less when increasing l [57]. This leads to less probability to find the valence electron penetrating the ionic core with larger orbital angular momentum, l. Therefore, the energy shift due to the quantum defect decreases with increasing orbital angular momentum, l, of the Rydberg states. That is, the orbits with higher angular momentum of Rydberg atoms are closer to those of hydrogen atoms. In Table 2.2, the value of quantum defect is the largest for $S_{1/2}$, where the quantum number of orbital angular momentum is $l = 0$. In the MW E-field sensing experiment, wavefunctions for S($l = 0$), P($l = 1$), D($l = 2$), and F($l = 3$) are needed. The higher orders of quantum defect are much smaller than the zeroth order. To maintain the precision of wavefunctions for these states ($l \leq 3$), the calculation keeps the orders of the quantum defect up to eight. For states with $l \geq 4$, hydrogenic wavefunctions can be directly used for Rydberg transitions.

2.3.3 Wavelength of Rydberg transitions

In the experiment, the MW E-field measurement is performed with ^{133}Cs atoms in thermal vapor cells. The probe laser, 852 nm, excites the atoms from $6S_{1/2}$ to $6P_{3/2}$, the exact wavelength, ~ 852.347275 nm, can be found in Ref [55]. The coupling laser, approximately 509 nm, excites the atoms from $6P_{3/2}$ to Rydberg states (n$\sim$50). The exact wavelengths of the coupling laser and the MW need to be calculated in order to tune the frequencies at resonances. The quantum defect described above can be used to accurately calculate the transition wavelength of the coupling laser and the MW frequencies between Rydberg states. Using the exact quantum defect parameter found in Ref. [56], the transition wavelength of the coupling laser and MW E-fields can be calculated as shown in Table 2.3. The table shows the wavelength of the coupling laser that is on resonance with the $6P_{3/2} \leftrightarrow nD_{5/2}$ transition. It also shows the MW frequencies that are on resonance with the $nD_{5/2} \leftrightarrow (n+1)P_{3/2}$ transitions, which is crucial to determine frequencies of target MW E-fields.

2.3.4 Calculation of transition dipole moments

In the MW E-field sensing experiment, one of the goals is to obtain MW E-field amplitude through the spectrum of 4-level EIT system. The Rabi frequency of the MW applied between Rydberg states, Ω_{MW}, is proportional to the MW E-field amplitude, E, and the transition dipole moment, $\vec{\mu}_{kj}$. The relation between the MW E-field amplitude and the Rabi frequency of the MW E-field is given by Equation. 1.1 in

Table 2.3: The calculated wavelength of the coupling laser $6P_{3/2} \leftrightarrow nD_{5/2}$ and the MW frequency coupling the transition $nD_{5/2} \leftrightarrow (n+1)P_{3/2}$ using quantum defect.

n	λ_C (nm)	f_{MW}(MHz)	n	λ_C (nm)	f_{MW}(MHz)
30	512.0483	29545.98	46	509.7812	7441.35
31	511.7870	26534.31	47	509.7144	6950.20
32	511.5521	23918.67	48	509.6520	6501.34
33	511.3401	21636.01	49	509.5935	6090.33
34	511.1481	19634.96	50	509.5388	5713.25
35	510.9736	17873.37	51	509.4873	5366.67
36	510.8146	16316.46	52	509.4390	5047.58
37	510.6693	14935.32	53	509.3935	4753.30
38	510.5362	13705.83	54	509.3507	4481.46
39	510.4139	12607.73	55	509.3102	4229.96
40	510.3013	11623.90	56	509.2721	3996.94
41	510.1974	10739.88	57	509.2360	3780.72
42	510.1013	9943.29	58	509.2018	3579.83
43	510.0123	9223.61	59	509.1695	3392.93
44	509.9297	8571.75	60	509.1388	3218.81
45	509.8528	7979.92			

Chapter 1, while the transition dipole moment $\vec{\mu}_{kj}$ is determined by

$$\vec{\mu}_{kj} = \langle k \, | \, \hat{e} \cdot \vec{r} \, | \, j \rangle, \tag{2.17}$$

where $\hat{e}$ is the polarization vector of the electromagnet wave, $\vec{r}$ is the displacement vector of the valence electron, and $\langle k |$ and $| j \rangle$ are the wavefunctions of the Rydberg states. The transition dipole moment includes angular and radial parts that are treated separately. If the value of the integral is zero, it means the transition is forbidden. In practice, it is the symmetry of the transition that determines the possibility of the transition. Therefore, the formula of the transition dipole moment is [58],

$$\langle k \, | \, \hat{e} \cdot \vec{r} \, | \, j \rangle = T_{ang} D_{12}. \tag{2.18}$$

The radial part D_{12} is,

$$D_{12} = \int_0^\infty R_{n,l} r R_{n',l'} r^2 dr, \tag{2.19}$$

where $R_{n,l}$ is the radial wavefunction. The angular part T_{ang} is,

$$T_{ang} = \int_0^{2\pi} \int_0^{\pi} Y_{l_k,m_k}^*(\theta,\phi) \hat{e} \cdot \hat{r}_0 Y_{l_j,m_j}(\theta,\phi) d\theta d\phi, \tag{2.20}$$

where $\hat{r}_0 = \vec{r}/r$. The details of the calculation of the angular part of the transition dipole moments can be found in Ref. [59]. For example, the transition between Rydberg states $nD_{5/2} \leftrightarrow (n+1)P_{3/2}$ leads to the change of the orbital angular momentum, $\Delta l = 1$. Specifically, when the MW E-field is a linear polarized field, the transition is directed to $m_F \to m_F' + 1$ and $m_F \to m_F' - 1$ with an equal possibility, where F is the projection or magnetic quantum number and m_F is the hyperfine quantum number. m_F and m_F' are the hyperfine sublevels of $nD_{5/2}$ and $(n+1)P_{3/2}$,

34

Table 2.4: The fitting parameters for the radial charge $Z_l(r)$.

Cs	a_1	a_2	a_3	a_4	r_c
$l = 0$	3.49546309	1.47533800	-9.72143084	0.02629242	1.92046930
$l = 1$	4.69366096	1.71398344	-24.65624280	-0.09543125	2.13383095
$l = 2$	4.32466196	1.61365288	-6.70128850	-0.74095193	0.93007296
$l = 3$	3.01048361	1.40000001	-3.20036138	0.00034538	1.99969677

respectively. This configuration gives the angular amplitude of the transition dipole moment, 0.49. The radial part of the transition dipole moment can be calculated using the radial wavefunctions of the Rydberg states which are n and l dependent.

2.3.5 Rydberg radial wavefunction

It is known that the wavefunction of the Rydberg electron satisfies the Schrödinger equation,

$$[-\frac{1}{2\mu}\nabla^2 + V(r)]\psi(r,\theta,\phi) = E\psi(r,\theta,\phi), \qquad (2.21)$$

where $V(r)$ is the Coulomb potential that has no angular dependence, E is the energy of the particle. Because the potential $V(r)$ has no angular dependence, the wavefunction is separable, $\psi(r,\theta,\phi) = R(r)\Psi(\theta,\phi)$, where $R(r)$ is the radial part and $\Psi(\theta,\phi)$ is the angular part. The radial part of the Schrödinger equation is,

$$[-\frac{1}{2\mu}(\frac{d^2}{dr^2} + \frac{2}{r}\frac{d}{dr}) + \frac{l(l+1)}{2\mu r^2} + V_{eff}(r)]R(r) = ER(r). \qquad (2.22)$$

To calculate the radial wavefunction, it is necessary to find a model for the radial dependent potential $V_{eff}(r)$, which empirically matches the energy levels of Rydberg atoms. The model for $V_{eff}(r)$ is [51],

$$V_{eff}(r) = -\frac{Z_l(r)}{r} - \frac{\alpha}{2r^4}(1 - e^{-(r/r_c)^6}), \qquad (2.23)$$

35

in which α is the static dipole polarizability of the nucleus, and r_c is the cutoff radius set by the potential fitting model to truncate the range of the core polarization term. The first term of the potential, $V_{eff}(r)$ describes the Coulomb potential for a radially dependent charge, $Z_l(r)$. $Z_l(r)$ is defined as,

$$Z_l(r) = 1 + (Z-1)e^{-a_1 r} - r(a_3 + a_4 r)e^{-a_2 r}, \qquad (2.24)$$

where Z is the nuclear charge; and a_1, a_2, a_3 and a_4 are fitting parameters for the potential model. The fitting parameters and the cutoff radius are tabulated in Table. 2.4. The parameters are determined empirically by fitting $V_{eff}(r)$ to Rydberg state energies [60]. With this model potential, the wavefunction for each state can be calculated using the Schrödinger equation 2.22. A FORTRAN program package called RADIAL is used to perform the calculation [61]. The RADIAL package uses the potential $V_{eff}(r)$ that includes those optimized fit parameters. The 1D Schrödinger equation can be numerically solved to obtain the wavefunctions of any Rydberg state of interest.

The wavefunction of a Rydberg state is highly oscillatory near the ionic core and less oscillatory near the outer turning point where is far away from the ionic core. To ensure the accuracy of the calculation, a non-uniform logarithmic grid is used in the RADIAL package for the potential and the wavefunction. For principal quantum number $n < 50$, the accuracy of the wavefunction is obtained with a grid of 1000 points. For larger n, more points are needed to obtain accurate a wavefunction. For example, when n is 100, a grid of 50000 points is applied in the calculation.

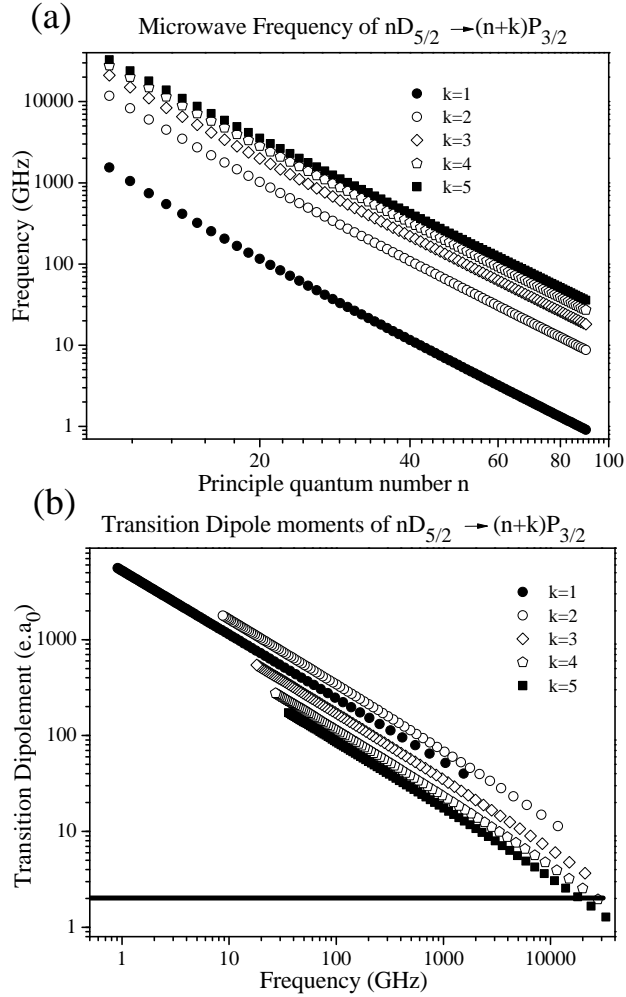The wavefunctions for Rydberg states are obtained for the principal number n

Figure 2.4: (a) shows the principal quantum number versus the microwave frequency of different transitions (b) shows the calculated transition dipole moment at different transition frequencies. The black line is the value of D_2 transition dipole moment of Cs.

between 20 to 100 and the orbital angular momentum quantum number l from 0 to 3. Then the transition dipole moments between Rydberg states can be evaluated according to equation 2.18. Using the RADIAL package, the numerical wavefunctions of Rydberg states are calculated with a resolution of < 1 a_0 to resolve the oscillation near the ionic core, which leads to accuracy of $< 1\%$ for the transition dipole moments. Fig. 2.4 shows the calculated transition dipole moments between Rydberg transitions that correspond to deviations of principal quantum numbers $k = 1, 2, 3, 4$, and 5. The black line in the Fig. 2.4(b) is the transition dipole moment for the Cs D_2 transition. The comparison in the figure shows that transition dipole moments between Rydberg states can be 3 orders of magnitude larger than that of D_2 transition. The large transition dipole moment results in a large AT splitting even with a small MW E-field, so that the sensitivity for the MW E-field measurement is high.

2.3.6 Discussion

This chapter describes the theory basis for MW E-field sensing that is based on the effect of the optical transitions between the two Rydberg states of Cs atoms. The atoms act as quantum interferometer using a 4-level EIT-like system. A full calculation without a weak probe approximation is needed because MW E-field sensing requires a relatively strong probe to maintain a high SNR signal. By simply changing the principal quantum number, n, this atom-based method can cover a large frequency range, from the GHz range to the THz range as shown in Fig. 2.4(a). This chapter also presents calculations for transition dipole moments between Rydberg states and

briefly describes a FORTRAN program package to calculate wavefunctions of Rydberg states. The transition dipole moments between Rydberg states are calculated with an accuracy of $< 1\%$. The transition dipole moments can be determined even more accurately with modern spectroscopy of Rydberg atoms [62]. The huge transition dipole moment between two Rydberg states ensures a high sensitivity for MW E-field sensing. The ability for Rydberg atoms to convert a small MW E-field to a large Rabi frequency makes them to be good candidates for MW electrometry.

Chapter 3

Experimental Setup

3.1   Introduction

MW E-field sensing depends on an EIT window with Rydberg atoms in vapor cells. As discussed in Chapter 1, the Rydberg EIT window is generated with atoms in a vapor cell by a probe laser and a coupling laser. The two lasers are in a counter-propagating geometry to reduce the Doppler broadening. With a MW E-field resonant with two adjacent Rydberg states, an Autler-Townes (AT) splitting is induced in the probe transmission. A photodiode captures the probe signal. The signal is sent to an oscilloscope to record the data. Therefore, vapor cells and the lasers generating the EIT window are essential for the experiment.

This chapter describes the experimental setup including vapor cells and laser locking systems. First, a conventional glass blowing method is presented to manufacture vapor cells which fulfill the requirements of generating narrow bandwidth Rydberg EIT for MW E-field measurements. Then, two laser stabilization systems are introduced. One stabilization system uses atomic energy levels as frequency references. This system uses dichroic atomic vapor laser lock (DAVLL) to lock the probe laser on the D_2 transition of a Cs atom, and an EIT signal to lock the coupling laser on the $6D_{5/2} \leftrightarrow nP_{3/2}$ transition. The other stabilization system uses a high finesse optical cavity as a frequency reference via a Pound-Drever-Hall (PDH) technique.

3.2 Vapor cells

Due to the high performance in precision atomic spectroscopy, atomic vapor cells are crucial for many atom-based sensors, such as atomic clocks [63], magnetometers [3], and gyroscopes [64]. The advantage of using vapor cells for atom-based sensors is that precision measurements of physical quantities are performed with atoms avoiding the use of cryogenic techniques. This advantage allows a significant reduction of volume and power consumption. Thus, such atom-based sensors can be highly miniaturized and directly used in many applications. Different fabrication techniques of vapor cells have been developed to meet requirements of such atom-based sensors. These techniques include conventional glass blowing [65], gluing [66], glass frit bonding [67], anodic bonding [68, 69], direct bonding and hollow core fibers [70]. This section describes a conventional glass blowing method to manufacture vapor cells for the MW E-field sensing experiment.

3.2.1 Vapor cell manufacturing process

The MW E-field sensing has several requirements on the vapor cells. First, the material of vapor cells should be optically transparent for the involved lasers and chemically inert for the alkali atoms. Pyrex and quartz are good choices for the current experiments. Second, it is necessary to produce tight sealing vapor cells that are free of leaking. Because alkali atoms in vapor cells react with many materials, the leaking of the vapor cells increases the chemical instability of the alkali atoms contained in the vapor cell. In addition, Rydberg atoms are sensitive to perturbations. The collisions

between Rydberg atoms and gas leaking into the vapor cell will broaden or even destroy the Rydberg EIT signal. Moreover, there are additional specific requirements for the geometry of vapor cells in the MW E-field sensing experiment. For example, in Chapter 5, different sizes of vapor cells are used to study the effect of the geometry of vapor cells to MW E-field measurement. To fulfill the above requirements, most of the vapor cells in the experiment are manufactured using a conventional glass blowing method.

The setup to manufacture vapor cells is shown in Fig. 3.1. The setup basically is a manifold with glass cells attached to it. The manifold consists of a pyrex tube, a liquid Cs container, an empty ampoule, empty vapor cells, and an iron hammer. The left end of the pyrex tube has an adaptor to connect to a vacuum pump. The right end of the pyrex tube is filled with liquid Cs, containing 1 gram of Cs. Empty vapor cells are connected to the pyrex tube. The vapor cells are made of pyrex or quartz. The leftmost cell in Fig. 3.1 is an ampoule to recycle the residual liquid Cs. An iron hammer sealed in a small pyrex tube is placed inside the manifold on the left side. The position of the iron hammer is controlled by a magnet. The iron hammer smashes the ampoule on the right when the vacuum of the manifold is down to 10^{-9} Torr. When the ampoule of the liquid Cs is smashed, the pyrex tube can be slowly tilted so that the liquid Cs can be filled into glass cells. For the amount of atoms in glass cells, a small droplet of liquid Cs is enough to perform the MW E-field sensing. The residual liquid Cs can be recycled in the empty container attached to the pyrex tube.

The vapor cells used in the MW E-field sensing are sealed by flame in order to
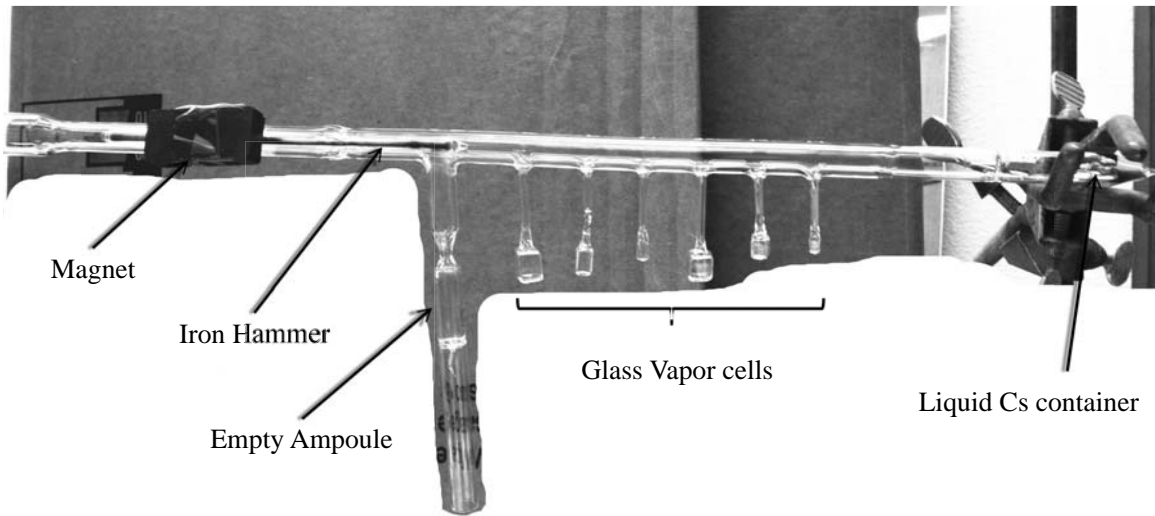
Figure 3.1: (color online) The glass manifold for manufacturing Cs vapor cells. The left side of the manifold has the adaptor to connect to vacuum pump. The right side of the manifold is the liquid Cs container with 1 g Cs atoms. The center is pyrex or quartz cells to be filled with Cs atoms. The right one is a container to recycle to residual liquid Cs atoms.
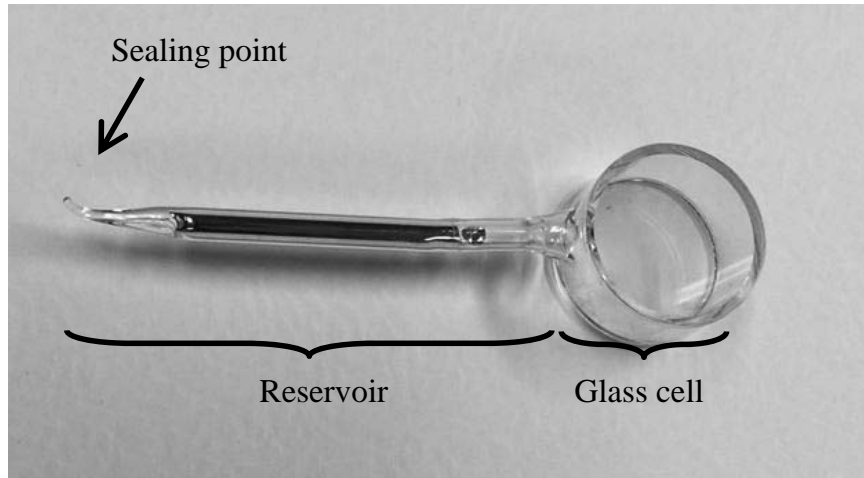
Figure 3.2: A typical vapor cell for the MW E-field sensing experiment. The reservoir is long to minimize the temperature of glass cell during sealing process.

tightly maintain the high vacuum after sealing. To determine if there is leaking in the vapor cells produced by the glass blowing method, Rydberg EIT spectroscopy was carried out with these vapor cells. A broadened Rydberg EIT window is the signature of leaking. The surface of vapor cells can be distorted because the high temperature of the sealing process can melt the glass. To minimize the distortion of the cell surfaces, the reservoir of a typical vapor cell is made longer compared to commercial vapor cells so that the temperature of the glass cell can be significantly lower than the tip of the reservoir during the sealing process. Fig. 3.2 shows one of the vapor cells manufactured for MW E-field measurement.

To improve the MW E-field measurements, efforts are ongoing to develop alternative manufacturing methods to construct vapor cells for the MW electrometry. One possible and promising approach is anodic bonding. The approach avoids melting glass

so vapor cells constructed using anodic bonding can be much smaller than those using the glass blowing method. Millimeter-sized vapor cells have been fabricated using the anodic bonding technique [71]. Unlike the gluing technique that requires careful choice of glue [66], anodic bonding uses triple stack glass-to-glass bonding in order to attach two glass plate to a center glass frame at 300 °C [69]. Thin film electrodes can be added between the glass-to-glass bonding layer. The small electrodes can be used to heat the vapor cells, apply DC E-fields and cancel stray magnetic fields.

The laser locking system is another important part of the experimental setup. The Rydberg atom-based MW electrometry is dependent on an EIT window that needs a probe laser and a coupling laser. Both of the lasers need to be frequency stabilized with narrow linewidths to resolve the AT splitting in the MHz regime. Moreover, the data for the MW E-field measurements are usually collected over long periods of time, especially when estimating the sensitivity of the MW measurements. Therefore, the lasers are required to have both narrow linewidths and long term stability.

3.3   DAVLL and EIT stabilization systems

The common method of frequency stabilization of lasers is dependent on a dispersive signal with a zero-crossing at the lock point. The signal is sent to a proportional-integral-derivative (PID) circuit to provide a feedback to stabilize the frequency of the laser. The lasers used for the MW E-field measurement have PID circuits integrated in Digilock 110 from Toptica. This section discusses how to generate a dispersive signal to stabilize the frequency of the lasers at an atomic transition,

which is an absolute atomic frequency reference and ensures both short-term and long-term stability. The probe laser is stabilized using the hyperfine structure of the D_2 transition of Cs atoms, while the coupling laser is stabilized using the resonance of an EIT window. The method for stabilizing the probe laser adapts sub-Doppler dichroism in a Cs vapor cell based on the Zeeman effect, known as DAVLL [72]. The setup is simple and fulfills the needs of the experiment in terms of stability and linewidth. The method for stabilizing the coupling laser is an EIT locking scheme. The EIT locking scheme involves frequency modulation (FM) spectroscopy to derive a dispersive signal with a two-photon process. The FM spectroscopy is widely used in laser-locking schemes because of the ability to provide high signal-to-noise ratio signals.

3.3.1 DAVLL locking system

The probe laser in the MW E-field sensing experiment is a diode laser (TOPTICA DL-pro) working at a wavelength of 852 nm. The laser is stabilized using a DAVLL technique [73]. This technique uses a magnetic field to separate the Zeeman components of an absorption signal. A linearly polarized incident laser beam consists of two circular orthogonal polarized components with equal amplitudes, σ^+ and σ^-. In the presence of a magnetic field, the absorptions of the two components are different due to the energy splitting caused by the Zeeman effect. For an atomic state with angular momentum of $J = 1$ in a magnetic field, the $m_J = +1$ state are shifted to a higher frequency absorbing the σ^+ component, while the $m_J = -1$ state are shifted to a lower frequency

absorbing the σ^- component. A subtraction of the two components gives a dispersive signal with the center of the signal being at the degenerate atomic state without the presence of the magnetic field.

The setup of the DAVLL stabilization system is shown in Fig. 3.3(a), where the probe laser, 852 nm, is locked to the hyperfine structure of the D_2 transition of Cs atoms. To resolve the hyperfine structure of the excited state $6P_{3/2}$, counter-propagating beams are used to generate Lamb dips. As shown in Fig. 3.3(a), the transverse linear polarized beam, transmitted through the vapor cell, is considered as a pump beam while the reflected beam is considered as a probe beam. A quarter waveplate is placed in front of the mirror to shift the polarization of the probe beam perpendicular to the the pump beam so that the probe beam can be captured by a photodiode placed at the other side of a polarized beam splitter (PBS). A Faraday coil surrounding the Cs vapor cell generates a magnetic field that shifts the target degenerate state. The amplitude of the magnetic field is applied to atoms of the vapor cell in a way that the Zeeman shift is about the linewidth of the two sub-levels. Then, the beam carrying the information of two hyperfine components of D_2 transition is separated by a quarter waveplate and another PBS. The two hyperfine components are captured by two photodiodes respectively and sent to a subtraction circuit where a dispersive signal is obtained.

By measuring the root-mean-square value of the locking signal, an instantaneous linewidth of ~ 100 kHz for the probe laser is obtained using the DAVLL stabilization method. The long term stability of DAVLL is strongly dependent on the environment,
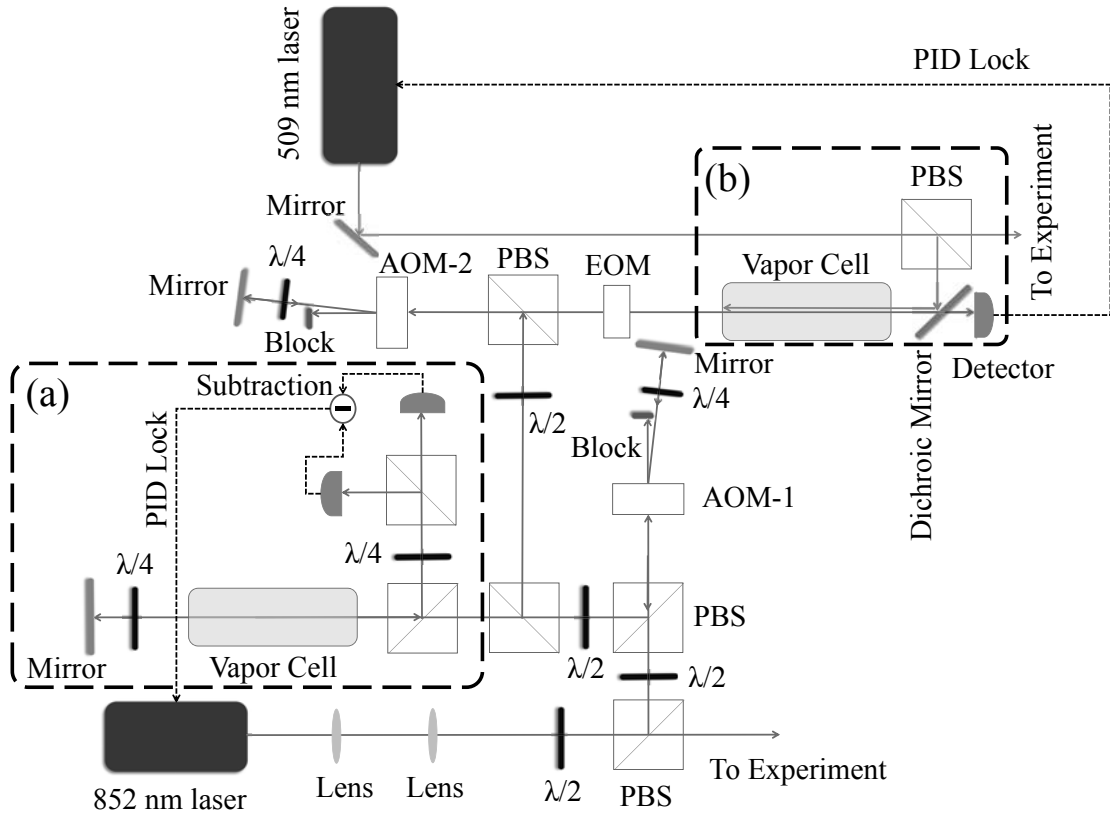
Figure 3.3: EIT locking setup scheme. The locking system consists of two parts. (a) Dichroic atomic vapor laser locking (DAVLL) for 852 nm with two acoustic-optical modulators (AOM) that are used to shift the frequency of the probe laser; (b) EIT laser stabilization for the 509 nm laser. The coupling beam, 509 nm, counter-propagates with the probe beam, 852 nm. The two lasers interact with Cs atoms in a vapor cell. The probe beam is phase-modulated through an EOM and detected by a photodetector.

especially the thermal fluctuations. The DAVLL system is placed in a plastic box to minimize the thermal fluctuations from the environment. A temperature stabilization of the vapor cell of the DAVLL setup is an effective method to improve the long term stability. Given the linewidth and the stability of the probe laser, the DAVLL locking scheme demonstrated in this section is adequate to perform MW E-field measurements.

The frequency-stabilized laser at 852 nm plays two important roles in the MW E-field experiment. One is to work as a probe laser in the MW E-field measurements. The other role is to generate a two-photon EIT signal to stabilize the frequency of the coupling laser at 509 nm. These two important roles are carried out in two different vapor cells, respectively. Therefore, the 852 nm laser beam is split by a PBS, and two acoustic-optical modulators (AOM) are implemented in the two paths of the probe beam respectively. Both of the AOMs are tunable in frequency and shift the frequency of the probe laser beams about 250 MHz away from the locking point of the DAVLL.

The DAVLL system is set to lock at the $6S_{1/2}$ (F = 4)$\leftrightarrow$$6P_{3/2}$ (F$'$ = 4) transition in the experiment. Thus, the frequency of the two laser beams passing through the two AOMs are frequency-shifted to the $6S_{1/2}$ (F = 4)$\leftrightarrow$$6P_{3/2}$ (F$'$ = 5) transition, where both of the MW E-field sensing and the EIT locking for the coupling laser are performed. To minimize intensity fluctuations of the probe laser in the MW E-field sensing experiment, a PID loop is implemented to stabilize the intensity of the probe beam.

3.3.2   EIT locking system

The coupling laser at a wavelength of 509 nm is stabilized through an EIT signal. The EIT signal for the stabilization system is generated by a two-photon cascade transition, $6S_{1/2}$ (F = 4)$\leftrightarrow$$6P_{3/2}$ (F$'$ = 5) for the 852 nm laser and $6P_{3/2}$ (F$'$ = 5)$\leftrightarrow$$nD_{5/2}$ for the 509 nm laser. The two-photon frequency-stabilization scheme uses the probe laser signal to stabilize the coupling laser that is at a completely different wavelength. Through an intermediate state, $6P_{3/2}$ (F$'$ = 5), the information of the coupling laser at 509 nm is transferred to the probe laser at 852 nm via the two-photon EIT signal. Therefore, the two-photon stabilization scheme, in principle, is applicable to a large number of applications for optical frequency stabilization involving a highly-excited state transition. The EIT locking system described here is limited by the residual Doppler effect. The residual Doppler effect is due to the wavelength mismatch between the probe laser and the coupling laser. Compared to the DAVLL technique which relies on the population in the states involved, the EIT locking scheme allows for no population in the intermediate state or the Rydberg state. In an ideal case, the the EIT locking scheme enables the width of the EIT signal to be free of the natural linewidth of the intermediate state, $6P_{3/2}$ (F$'$ = 5). Thus the width of the stabilization can be substantially reduced.

The two laser beams counter-propagate with each other in order to minimize the Doppler effect. The residual Doppler effect in the setup broadens the EIT signal to MHz regime. The vapor cell is shielded with μ-metal to reduce the effect of stray magnetic and electric fields. The transition dipole moment for the coupling laser is

two or three orders lower than that of the probe laser, so a suitable power for 509 nm laser is chosen in order to obtain a strong EIT signal that is not broadened by the coupling laser power. The typical full-width-half-maximum (FWHM) of the EIT signal for locking is around 4 MHz. The beams of both lasers are shaped as Gaussian beams with lenses to ensure maximum overlapping in the vapor cell.

In order to generate a dispersive signal from the cascade EIT transition, a FM spectroscopy technique is used for the laser stabilization. The probe laser is frequency modulated using an electro-optical modulator (EOM). A high speed photodiode captures the signal that is demodulated in a mixer. The signal from the output of the mixer is sent to the PID circuit to lock the frequency of 509 nm laser. Just by changing the principal quantum number of Rydberg states, the scheme can lock the coupling laser in a large wavelength range, from 508 to 512 nm.

The linewidth of the coupling laser obtained using the EIT stabilization scheme is $\sim$500 kHz. The transit time broadening contributes to the linewidth $\sim$ 30 kHz. The locking information of the coupling laser is transferred through the two-photon EIT signal. The stability of the EIT signal is dependent on that of the probe laser. Thus, the stability of the probe laser is evaluated to be $\sim$ 100 kHz. Despite of these limitations, the linewidth for the coupling laser is narrow enough to resolve the MW E-field features through an AT splitting. The EIT locking method for the coupling laser is adequate to perform several experiments described in later chapters, including the subwavelength E-field imaging and the geometry study of the vapor cells in the presence of MW E-fields.

3.4 Cavity locking

To measure MW E-fields with a higher sensitivity than what has been already achieved [38], the MW E-field sensing experiment requires spectrally narrower lasers than obtained with the DAVLL and EIT locking methods. A high-finesse reference cavity with a narrow resonance linewidth is a good candidate to stabilize both the probe and coupling lasers. The stabilization scheme utilizes a Pound-Drever-Hall (PDH) technique that is a common method to stabilize lasers using a reference cavity [74]. The method was initially developed by P. V. Pound to stabilize the frequency of a microwave oscillator [75], and was later extended to the optical regime by R. Drever and J. L. Hall [76]. Owing to its ability to control and decrease the laser's linewidth, the PDH technique has wide applications in atomic physics, especially in precision atomic spectroscopy, e.g., optical frequency standards [77]. The technique can also be used in a reverse way to lock a cavity to a laser. The benefit of doing this is that one can measure extremely small changes in the length of cavity at a high precision [74].

The PDH technique basically works as described in Ref. [74]. A laser beam is phase modulated with an EOM and sent to a high finesse cavity. A high speed photodiode captures the reflection of the modulated light from the cavity. The signal detected by the photodiode contains a phase modulated carrier component along with two sidebands at the modulation frequency. By mixing the signal with a local oscillator, an error signal is generated and sent to a PID circuit to stabilize the frequency of the laser. This technique is widely applied for laser frequency stabilization because of its high stability and ultranarrow linewidth. This section presents several important parts

for a PDH locking system, such as the reference cavity, temperature stabilization, mode matching, and experimental setup including the optical alignment and electronics.

3.4.1 Reference cavity

For the MW E-field sensing experiment, both the probe laser and coupling laser are locked at a high finesse reference cavity. The two mirrors of the cavity are fixed on the two ends of a 100 mm long ultralow expansion (ULE) solid cylindrical rod with a hollow center. The condition for a stable cavity is,

$$0 < \left(1 - \frac{L}{R_1}\right)\left(1 - \frac{L}{R_2}\right) < 1, \tag{3.1}$$

where L~100 mm, is the distance between the two mirrors of the cavity, R_1 and R_2 are the radius of curvature (ROC) of the two mirrors. One mirror of the reference cavity is a flat mirror, $R_1 \to \infty$, while the other is concave mirror with the ROC, $R_2 = 500 \ mm$. Therefore, a simple calculation will show the cavity fulfills the stable condition. The free spectral range (FSR) is estimated by,

$$FSR = \frac{c}{2nL}, \tag{3.2}$$

where c is the speed of light, and n is index of refraction. The cavity is placed in a vacuum system [78], giving $n = 1$. As a result, the FSR is ~1.5 GHz. The mirrors of the reference cavity are coated for both 852 nm and 1018 nm laser with high reflectivity. The reflectivity of both mirrors is > 99.9%, resulting in a finesse around 12000-16000. The cavity is loaded into a cylindrical aluminium chamber. The cavity is pumped down to 10^{-7} Torr by a mechanical pump; and then, an ion pump connected to the cavity is turned on to maintain the vacuum.

3.4.2 Temperature stability

The temperature variation is an important factor to the stability of the cavity. The thermal expansion of the ULE material is minimum at a certain temperature, T_c. T_c is also called the zero-expansion temperature. Although the use of such a ULE material as a spacer considerably reduces the thermal drift, the relative length of the ULE material has a quadratic dependence on temperature as follows,

$$\Delta L/L \propto (T - T_c)^2, \tag{3.3}$$

where ΔL is the length variation, and T is the temperature of the ULE material. To minimize the length variation, the temperature should be stabilized around T_c.

The zero-expansion temperature of the ULE material, $T_c = 29\ ^oC$, is above room temperature. The value of T_c allows the ULE material to be heated to the zero-expansion temperature. A precise solid state temperature sensor with a precision of ± 0.05 °C is used to detect the temperature of the ULE material. An active temperature stabilization system is built to stabilize the temperature of the cavity by using a PID circuit. The PID circuit controls the electric current of heaters inside the cavity according to the comparison of the set temperature and the value read by the temperature sensor.

3.4.3 Mode matching

The laser beam inside the cavity is described by Hermite-Gaussian modes. Hermite-Gaussian modes (TEM$_{lm}$ modes) have wavefronts represented by mode order (l,m). l and m refer to the x and y direction of the beam profile in a cartesian
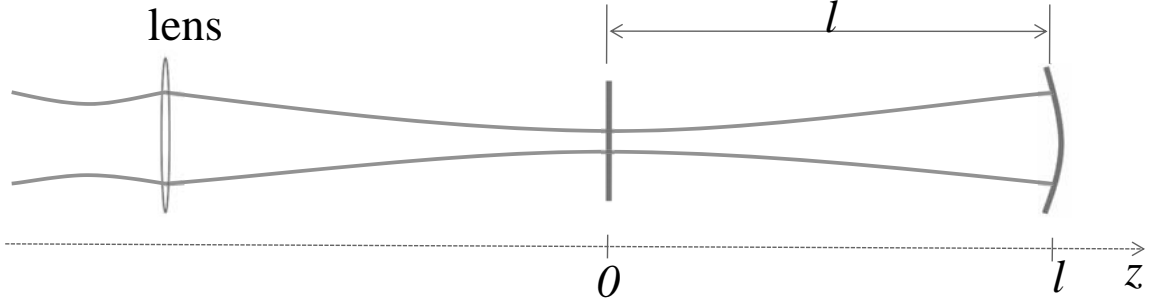
Figure 3.4: The alignment of the cavity. The cavity consists of a plano mirror and a convex mirror. The laser beam propagates in z direction. To obtain the mode matching condition, a lens is used to adjust the parameters of the laser beam. Under the mode matching condition, the waist of the beam should be at the 0 point where the flat mirror of the cavity is; and the radius of curvature (ROC) of laser beam at l point should be equal to that of the concave mirror.

coordinate. A Gaussian beam is a special Hermite-Gaussian beam with the mode order of (0,0), i.e., TEM_{00} mode. A proper alignment is required to largely reduce the excitation of higher orders of modes and keep only the Gaussian mode (TEM_{00} mode). This is called mode matching.

For a reference cavity that is composed of a flat mirror and a concave mirror, the expected alignment with proper mode matching is shown in Fig. 3.4. A Gaussian beam propagates in z direction. The flat mirror should sit at point 0 where the beam waist is. The concave mirror is placed at point l. The ROC of the Gaussian beam at point l should be equal to that of the concave mirror. In this case, the TEM_{00} mode of Hermite-Gaussian beam will be in resonance with the cavity. As shown in
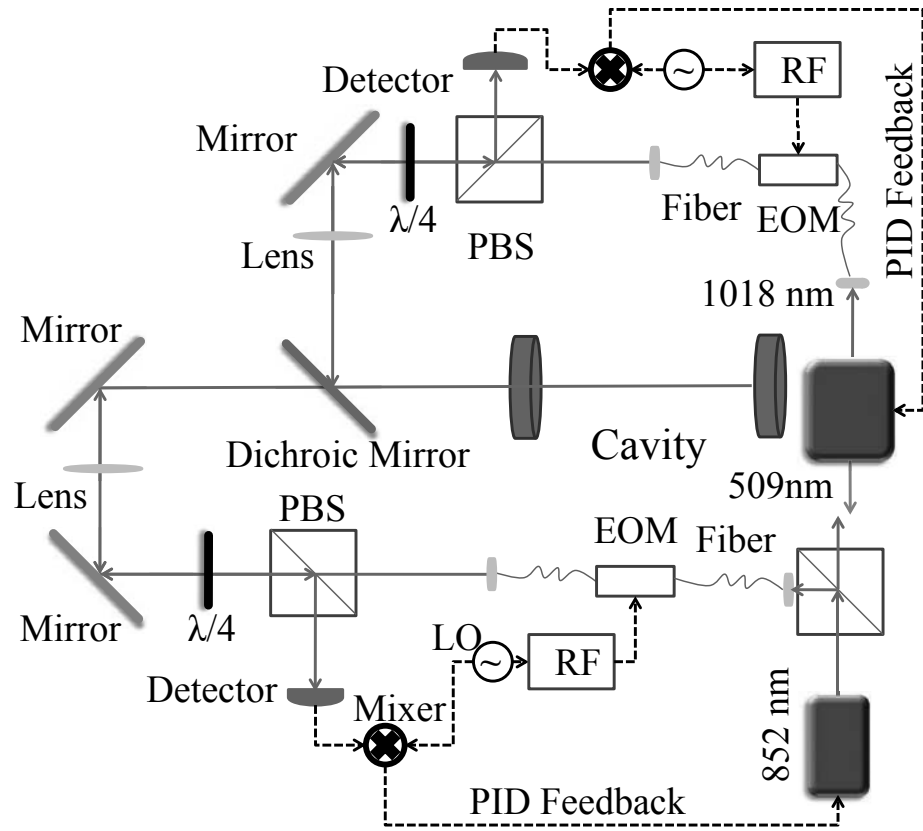
Figure 3.5: Pound-Drever-Hall transfer cavity locking setup. The two
lasers are locked on one cavity coated for 852 nm and 1018 nm with high
reflectivity. 852 nm is the probe laser while the 1018 nm laser is the
seeding laser for coupling laser, 509 nm which is frequency doubled in a
bowtie cavity.

Fig. 3.4, one lens is placed in front of the cavity. The lens changes the waist and ROC of the Gaussian laser beam to fulfil the mode matching condition. The focal length and the location of the lenses can be accurately estimated using ABCD matrix, which describes the propagation of a Gaussian beam in an optical system.

3.4.4 ABCD matrix

The property of a Gaussian beam is easily represented by the q-parameter, $q(z)$. The q-parameter is a complex valued parameter that describes both the size and curvature of the Gaussian beam, i.e.,

$$q(z) = z + iz_0, \tag{3.4}$$

where $q(z)$ is also called the complex ROC because the inverse of $q(z)$ relates to the ROC as,

$$\frac{1}{q(z)} = \frac{1}{z + iz_0} = \frac{z}{z^2 + z_0^2} + i\frac{z_0}{z^2 + z_0^2} = \frac{1}{R(z)} - i\frac{\lambda_0}{\pi n r(z)^2}, \tag{3.5}$$

where $R(z)$ is the ROC at point z, and $r(z)$ is the beam radius at the point z. If the initial value of $q(0)$ is specified, the values of $R(z)$ and $r(z)$ at point z in the beam propagation direction can be calculated. The property of the Gaussian beam can be estimated using ABCD matrix when propagating in an optical system.

When the beam propagates in free space with a distance d from the position z_0, the complex radius of curvature is,

$$q_2(z) = q(z_0) + d. \tag{3.6}$$

The equation is the free space propagation law for a Gaussian beam. It can also be

written as,

$$q_2(z) = \frac{Aq(z_0) + B}{Cq(z_0) + D},$$ (3.7)

where

$$\begin{pmatrix} A & B \\ C & D \end{pmatrix} = \begin{pmatrix} 1 & d \\ 0 & 1 \end{pmatrix}.$$ (3.8)

The expression 3.8 is the ABCD matrix in free space. Similarly, the ABCD matrix is given for a Gaussian beam propagating through a thin lens with focal length f,

$$\begin{pmatrix} 1 & 0 \\ -2/f & 1 \end{pmatrix}.$$ (3.9)

When a Gaussian beam propagates in an optical system with multiple optical elements, the q-parameter can be calculated by multiplying the ABCD matrices for each optical element. For example, if a thin lens is placed with the focal length f, at a distance d, in the beam propagation direction, the overall ABCD matrix simply becomes,

$$\begin{pmatrix} A & B \\ C & D \end{pmatrix} = \begin{pmatrix} 1 & 0 \\ -2/f & 1 \end{pmatrix} \begin{pmatrix} 1 & d \\ 0 & 1 \end{pmatrix}.$$ (3.10)

With equation 3.10, the focal length of a lens and suitable place for the lens can be calculated to fulfil the mode matching condition of the cavity. For example, the beam waist of the 852 nm laser is ~1 mm and located 600 mm away from the cavity. The calculation shows that the focal length of the lens is around +500 mm, and the lens should be placed ~300 mm away from the flat mirror of the cavity. With the calculated parameters, the mode matching is easily realized in the experiment.
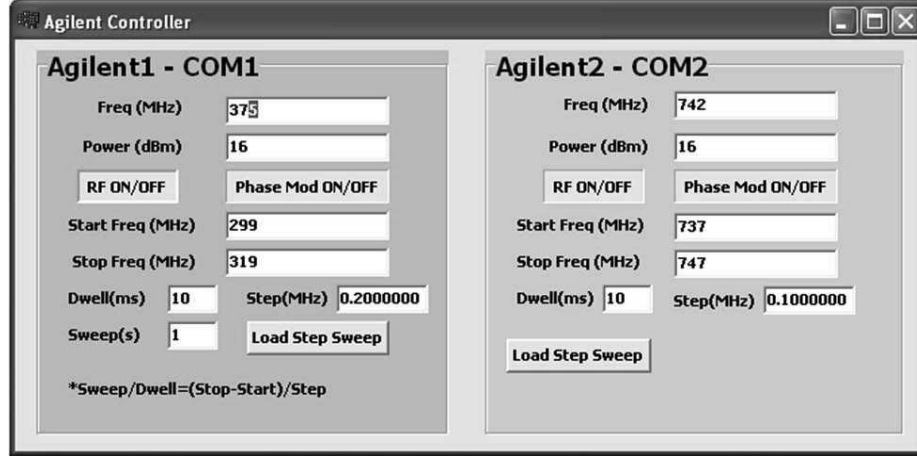
Figure 3.6: (color online) The C++ program to control the RF generator using RS-232 port of the computer. There are two channels there, the right side is the channels for 852 nm laser while the leftside is the channel for 1018 nm laser.

3.4.5 Experimental setup for PDH locking system

Fig. 3.5 shows the experimental setup for PDH locking. The probe laser and the coupling laser are stabilized through one ULE cavity. The output beam of the probe laser is directly sent to the reference cavity for stabilization. The coupling laser is a frequency doubled laser seeded by a near-infrared laser at a wavelength of 1018 nm. To avoid the noise from the frequency-doubling procedure, the seed laser is sent directly to the ULE cavity for stabilization. The two laser beams are coupled into two fiber-based EOMs respectively. After being mode matched to the reference cavity using lenses, the two laser beams are on resonance with the cavity mode, TEM_{00}. The two lasers are aligned together via a dichroic mirror in front of the cavity. The transmitted beam through the cavity is captured by a photodiode for monitoring.

59

The reflected beam is polarization-rotated by a quarter waveplate to send to a fast
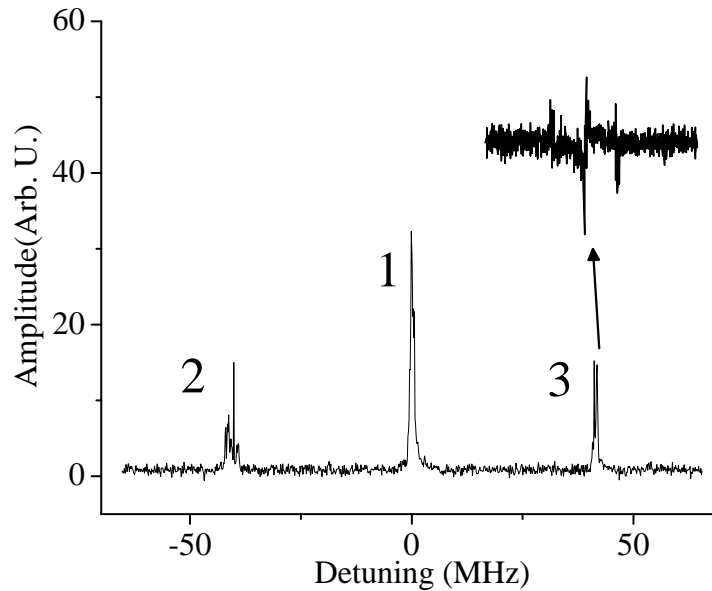photodiode.

Figure 3.7: The lineshape of the resonance signal with sidebands generated
by the the modulation through an EOM. The inset is the PDH signal of
one of the sideband whose center peak is the locking point.

The function of an EOM is to tune the frequency as well as to modulate the
phase of the laser. The EOM receives radio-frequency (RF) signals from a function
generator. The function generator is the source for both the frequency detuning and
phase modulation. The function generator is controlled using a C++ program via
a RS-232 interface in a desktop computer. The program panel is shown in Fig. 3.6.
The left side is for the RF source of the probe laser while the right side is for the
RF source of the coupling laser. The linewidth of the cavity is less than 100 kHz. A
typical PDH signal detected by a photodiode is shown in Fig. 3.7. Peak 1 is the cavity

resonant peak while peak 2 and peak 3 are the sidebands where the lasers are locked. The inset is the PDH signal that is used to lock the laser with a PID loop.

3.4.6 Discussion

This section describes how to stabilize the frequencies of the probe and coupling lasers using a high-finesse cavity as a frequency reference employing a PDH technique. The cavity is on resonance with the TEM_{00} mode of laser beams. The lasers are phase-modulated and frequency-detuned by EOMs. The lasers are locked PDH signals generated at one of the sidebands of the cavity mode. For a cavity with a FSR of 1.5 GHz and a finesse of ~15000, the corresponding FWHM of the transmission peak is ~100 kHz. Therefore, the instantaneous linewidth of both lasers are less than 100 kHz. By using a temperature stabilization loop, the reference cavity is operated at the zero-expansion temperature T_c. At the temperature of T_c, the length of the cavity is least sensitive to temperature instabilities. Thus, the temperature stabilization ensures the long term stability of both lasers. The long term stability is a necessity for a long time integration to estimate the sensitivity of the MW electrometry. The PDH method has been used for locking diode lasers in many different applications, including precision metrology, high resolution atomic spectroscopy, and quantum information and communication [79]. An ultra-narrow linewidth at sub-Hz scale can be achieved by improving the stability of the ULE cavity and electronic locking loops [80].

3.5 Summary

This chapter describes some important and unique aspects of the experimental setup for the MW E-field measurements. The vapor cells for the MW electrometry are constructed using a conventional glass blowing method. The high temperature in the process of the construction sometimes distorts the surfaces of the vapor cells. The effort is ongoing to construct better vapor cells to improve the MW electrometry. For example, the anodic bonding method, which can be utilized to construct vapor cells with better surfaces, smaller sizes, and electrodes attached between the bonding layers.

The chapter also describes laser stabilization schemes using atomic transitions as absolute frequency references. A DAVLL technique is adapted to stabilize the frequency of the probe laser while an EIT scheme is demonstrated to stabilize the coupling laser to a Rydberg state via a two-photon transition. Both of the DAVLL and the EIT stabilization schemes are reliable and simple in implementation. A micro-DAVLL of 9-mm long is implemented using a 3-mm vapor cell [81]. Such a small-sized laser device can facilitate the miniaturization for atom-based MW electrometers. Although the current linewidth for the EIT stabilization scheme is limited by the residual Doppler effect, the EIT window determined by the spontaneous decay rate of Rydberg states can be orders of magnitude smaller than the that of Cs D_2 transition. Thus, the EIT stabilization scheme has the potential to reduce the width of the coupling laser down to several kHz, which is essential to improve the sensitivity of the MW E-field measurements.

In addition, to obtain better stability and narrower linewidth of the lasers for MW electrometry, both the probe laser and the coupling laser are stabilized to a high-finesse cavity by a PDH technique. The linewidths of the probe laser and coupling laser are below 100 kHz due to the high-finesse of the cavity. Both the probe and the coupling lasers can be locked for days without observable drifting by stabilizing the temperature of the cavity. The narrow linewidths and the long term stability is the prerequisite to pursue higher sensitivity of the MW E-field measurements.

Chapter 4

Subwavelength Imaging of MW E-fields Using Rydberg Atoms in Vapor Cells

4.1 Introduction

In this chapter, the subwavelength MW E-field imaging is demonstrated using Rydberg atoms in vapor cells at room temperature. A standing wave pattern is created to image MW E-field as a test. The experiment achieved a high spatial resolution, $66\mu m$ or $\lambda_{MW}/650$ at 6.9 GHz, where λ_{MW} is the wavelength of the MW E-field in free space. Using the atom-based approach, the near-field imaging is also demonstrated above a coplanar waveguide.

4.2 Motivation

In prior work [38, 37], it has been demonstrated that with atoms contained in a thermal vapor cell, Rydberg atom-based MW E-field sensing is able to detect a minimum MW E-field amplitude of $\sim 8\,\mu\mathrm{V}\,\mathrm{cm}^{-1}$ with a sensitivity of $\sim 30\,\mu\mathrm{V}\,\mathrm{cm}^{-1}\,\mathrm{Hz}^{-1/2}$ [38]. This method is also capable of detecting a vecter MW E-field with an angular resolution of $0.5°$ [37]. The accurate measurement of MW E-field strength and polarization can lead to advances in applications such as antenna design, device development, characterization of electro-magnetic interference, advanced radar applications, and materials characterization including metamaterials characterization [18, 20, 21, 82, 83, 84, 85, 86].

The absolute measurement of MW E-fields at sub-wavelength resolutions and in the near field regime is necessary for many MW applications. However, as discussed in Chapter 1, there are two problems for sub-wavelength MW E-field measurement using conventional antennas. One problem is that the size of a typical MW E field antenna is $\lambda_{MW}/2$. Using such an antenna as a MW E-field probe, the measurements of MW E-fields require integration and averaging over the length of the probe. Therefore, it is quite problematic to measure a MW E-field with a subwavelength resolution. The other problem is that the probes are all made of metal, so they disturb the incident MW E-field. The precision of the measurement can be significantly reduced because of the metal material in the presence of the incident field. Rydberg atom-based MW E-field sensing uses gaseous alkali atoms in Rydberg states as MW E-field probes. Therefore, the MW E-field measurement is free of solid metal material and independent of the probe size. At present, there is no other work on imaging MW E-fields with atoms in vapor cells. Even for B-fields, where atom-based magnetometry is playing a crucial part [87], it is only recently that absorptive imaging for MW B-field has been implemented in vapor cells [88, 89]. Although a rather straightforward connection exists between an E-field and a B-field in free space, there is not always a simple relation between them in the near field. Moreover, because the methods for electrometry are different from magnetometry, many of the technical issues of imaging a MW E-field are also quite different from imaging a B-field. Thus, studies of imaging both E-fields and B-fields are important.

To meet the need for the subwavelength imaging of MW E-fields, an experimental
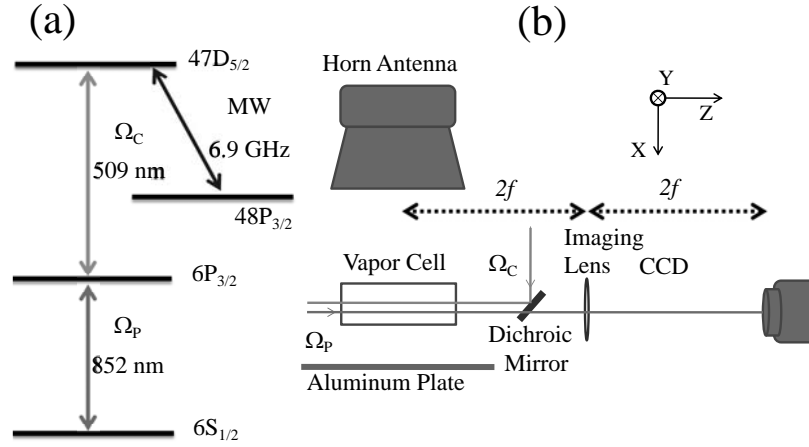
Figure 4.1: Setup and energy level diagram for the experiments on sub-wavelength imaging. (a) Ω_p and Ω_c are the Rabi frequencies for the probe and coupling transitions, respectively. MW labels the transition between two Rydberg states used for the standing wave E-field measurements. (b) The MWs generated by the horn antenna form a standing wave pattern between the aluminum plate and the horn antenna. The standing wave is sampled by the atoms in the Cs vapor cell and imaged by a $2f$ imaging configuration with a lens onto a CCD cameara, where f is the focus length of the lens. The horn antenna and plate are moved together to change the position of the vapor cell in the standing wave MW E-field.

scheme is demonstrated in this chapter for sub-wavelength MW electrometry using Rydberg atom EIT [90, 36] in Cesium (Cs) atomic vapor cells at room temperature. Comparing to other imaging methods, such as scanning probe technology [91, 92], the approach described here avoids cryogenics and eliminates the presence of conducting materials near the sample, therefore, field disturbances are minimized. In this chapter, 2-dimensional MW E-fields are imaged with a spatial resolution of $\sim \lambda_{\mathrm{MW}}/650$, $\sim 66\,\mu$m at $\sim 6.9\,$GHz. A test MW E-field in the form of a standing wave and a MW E-field in the near field regime of a CPW are used to demonstrate the sub-wavelength. The E-field resolution is $\sim 50\,\mu$V cm^{-1}, which is limited by the detection system.

4.3   Methods for MW E-field imaging

The transmission signal of the probe laser is captured by a CCD camera (Pco Pixelfly). As shown in Fig. 4.1, the probe beam is imaged onto the CCD camera using a single lens with a focal length of $f = 400\,$mm. The vapor cell is placed at a position, $2f$, in front of the lens and the camera is located at a distance of $2f$ behind the lens. The depth of the focus is $\sim 9\,$mm and the diameter of the Airy disk for the imaging system is $\sim 65\,\mu$m.

Fig. 4.2 is a diagram showing how to convert the images of the probe profile to MW E-field distribution. The CCD takes images by recording the intensity of the probe profile when scanning the probe laser frequency, Δ_P. An AOM is used as a shutter to switch the coupling laser on and off. The MW E-field information is contained in the images when the coupling laser is on, while the background of
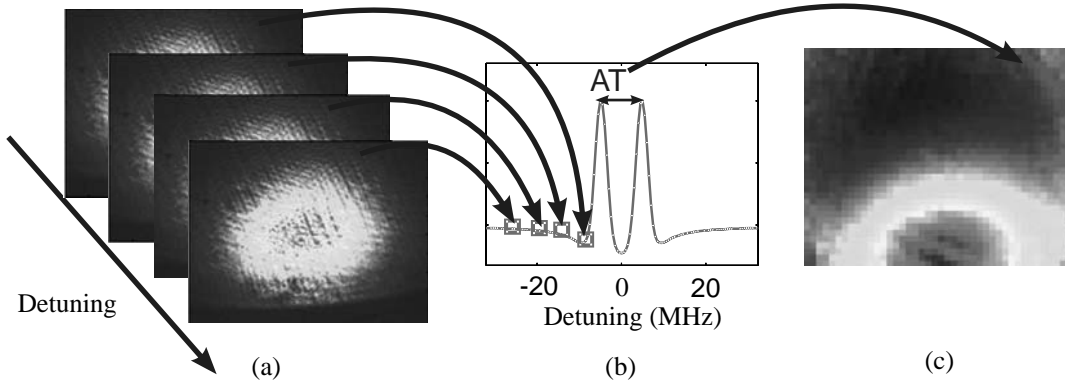
67

Figure 4.2: A diagram showing how to convert the pictures of probe profile to MW E-field distribution. (a) images showing the intensity of the probe profile at different probe detunings Δ_P; (b) the spectrum of AT splitting taken from one of the pixels in the images shown in (a); (c) MW E-field distrubution converted from the images in (a).

the transmission is obtained when the coupling laser is off. Images shown in 4.2(a) are those of the probe transmission after the subtraction of the probe background. These images show the spatial-dependent absorption with the CCD camera detuning Δ_P in discrete steps. The exposure time is longer than the lifetime of the Rydberg states, $\sim 50\,\mu$s, so that the steady-state condition of the EIT spectrum is reached. An exposure time of 1 ms is chosen in the experiment. Each image consists of 40 averaged pictures to minimize the intensity fluctuations of the probe laser. The spatial dependence of the MW E-field is obtained by averaging the probe laser transmission over small patches of each image. That is, for each patch in the images, the values of the profile intensities are recorded with the detuning of the probe laser. Then, the lineshape of the four-level EIT signal is formed with AT splitting at each patch. The

AT splitting is recorded to calculate the MW E-field amplitude of this patch. The dimension of the patches is $66\,\mu\mathrm{m}\times66\,\mu\mathrm{m}$. The amplitude of the MW E-field can be acquired across the overlap region of the probe and coupling laser beams. With this method, the images of intensities of the probe profile are converted to MW E-field distribution.

4.4 Numerical simulation with the finite element method

In the subwavelength imaging experiment, it is necessary to estimate the accuracy of the MW E-field measurement. To do this, a numerical model is needed to simulate the E-field distribution of the standing wave between the horn antenna and the aluminum plate. In this chapter, the target MW E-field is numerically simulated with a finite element (FE) method. The FE method [93] is a numerical technique for approximate solutions of MW E-fields through Maxwell equations with boundary conditions. The FE method requires large problems to be divided into smaller, and simpler parts, called finite elements (FEs). After using simple equations to solve these FEs, the solutions are combined together to model the entire problem. Variational methods are applied to minimizing the error of the numerical solutions. High frequency structural simulator (HFSS) is a commercial software that simulates MW fields using the FE method. The numerical results simulated in this chapter are generated by this software.

4.5   Imaging a standing wave MW E-field

4.5.1   Experimental setup

To demonstrate the subwavelength MW E-field imaging, a standing wave field is generated in the experimental setup as shown in Fig. 4.1(b). The MW E-field is emitted out of a horn antenna and reflected by an aluminum plate. The incident field and the reflected field interfere with each other, forming a standing wave pattern between the horn antenna and the aluminum plate. The frequency of the MW E-field is $\sim$6.9 GHz. To image the standing wave E-field at $\sim 6.9\,$GHz, the method uses the Cs level system shown in Fig. 4.1a. Through a 3-level Rydberg EIT system, $6S_{1/2} - 6P_{3/2} - 47D_{5/2}$, a "dark state" is created by a probe laser with a Rabi frequency, Ω_{P}, and a coupling laser with a Rabi frequency, Ω_{C}. By coupling a fourth level to the Rydberg EIT system, $48P_{3/2}$, with a MW E-field, a "bright state" is created, which leads the probe light to be absorbed again on resonance [38, 94, 95, 96]. The bright state induced by the MW E-field causes an AT splitting in the EIT spectrum for large enough MW electric amplitudes [38]. The AT splitting of the spectrum is proportional to the Rabi frequency of the MW E-field, $\Omega_{\mathrm{MW}} = \mu_{\mathrm{MW}} \, E_{\mathrm{MW}}/\hbar$, where E_{MW} is the MW E-field amplitude and μ_{MW} is the transition dipole moment for the $47D_{5/2} \longleftrightarrow 48P_{3/2}$ transition. In the experiments presented here, the probe and coupling lasers have opposite circular polarizations.

The setup configured for the experiment is shown in Fig. 4.1b. The probe laser light that drives the $6S_{1/2}(\mathrm{F} = 4) \to 6P_{3/2}(\mathrm{F} = 5)$ transition at $852\,$nm is generated

by a frequency stabilized diode laser. The frequency of the probe laser is stabilized

using a DAVLL scheme as described in Chapter 3. The coupling laser at 509 nm is

supplied by an amplified diode laser at 1018 nm that is doubled in a ring cavity. The

coupling laser is frequency stabilized and tuned to the $6P_{3/2} \rightarrow 47D_{5/2}$ transition of

Cs. The EIT locking scheme in Chapter 3 is used to lock the coupling laser. The

probe laser power is $50\,\mu$W resulting in $\Omega_P = 2.03\,$MHz. The coupling laser power is

$34\,$mW, corresponding to a Rabi frequency of $\Omega_C = 1.12\,$MHz. The diameter of the

probe (coupling) laser beam is $2.78 \pm 0.01\,$mm $(2.47 \pm 0.01\,$mm$)$. The transition dipole

moment of the MW E-field is $\mu_{MW} = 2938.5\,$e$\,$a$_0$, which is 1000 times larger than the

Cs D$_2$ transition dipole moment [55]. The probe and coupling lasers are configured in

a counter-propagating geometry. An HP 8340B is used for the MW source.

The MW E-field pattern that is investigated first is created by placing the

reflecting aluminum plate, $3\lambda_{MW}$ away from a horn antenna to create a standing wave

pattern of the MW E-field. As shown in Fig. 4.1(b), a standing wave is formed with a

spatial period of $\lambda_{MW}/2$ as predicted by the FE calculation using HFSS. The horn

antenna generates an MW E-field with the wavelength of $\lambda_{MW} = 4.3187099$ cm, or the

frequency of $6.9465189\,$GHz. To measure the standing wave of the MW E-field, the

horn antenna and the reflective aluminum plate are attached to a translation stage

such that they can be moved together to scan the position of the vapor cell along the

standing wave pattern of the MW E-field.

The transition dipole moment of the $6P_{3/2} \rightarrow 47D_{5/2}$ transition is two orders

smaller than that of the $6S_{1/2}(F = 4) \rightarrow 6P_{3/2}(F = 5)$ transition. Rydberg state

population results in Rydberg atom collisions and absorption of MWs as they pass through the laser beam overlap region. Absorption can be accounted for using Beer's law for the MW powers in our experiments. To lower the absorption of the MW E-field and collision effects, Rydberg state population should be low. On the other hand, the low Rydberg state population leads to low signal-to-noise ratio for the EIT window. The Rabi frequencies of the probe, Ω_P, and the coupling, Ω_C, are chosen to reduce the Rydberg state population, yet still obtain EIT signals that facilitate the MW E-field measurement in a reasonably large spatial area. As a result, the probe and the coupling laser powers result in the MW E-field measurements taking place in the intermediate regime of EIT.

4.5.2 Results

Fig. 4.3(a) shows the data of the subwavelength imaging experiment extracted along the center of the MW E-field pattern with the comparison to the FE calculation. The spatial resolution is $66\,\mu$m. The range of the data covers one half wavelength. The images are taken every $1\,$mm along the axis of the standing wave pattern, i.e. the x direction in Fig. 4.1(b). According to the comparison of the image data and the FE calculation, good agreement between the two traces is observed. The differences between the image data and the FE calculation can be attributed to the finite calculation regions, the presence of the cell walls, and the modeling of the horn antenna used for the FE calculation. Fig. 4.3(b) shows the 2-dimensional image data of a standing wave pattern, in which the plot is composed of 26 images, each offset by

1 mm in the x direction. The center of the transverse axis is on the y symmetry plane of the cell and the MW cavity, as shown in Fig. 4.1(b).

To test the accuracy of the subwavelength imaging technique, an iris is placed at the center of the probe beam. A photodiode is placed behind the iris to observe the spectrum of the probe laser, similar to experiments found in Refs. [38, 37]. Fig. 4.3(a) shows this measurement in comparison with the data obtained from the CCD camera and the numerical results using the FE method. The differences between the photodiode measurement and the subwavelength imaging measurement are analyzed for different traces along x. From the analysis, the standard deviation is 0.25 MHz at a spatial resolution of $66\,\mu$m. This uncertainty translates to a deviation of the MW E-field amplitude $\sim 67\,\mu\mathrm{V\,cm^{-1}}$ and the associated spatial resolution is $\sim \lambda_{\mathrm{MW}}/650$. With the current optical setup, a better spatial resolution can be obtained at the cost of uncertainty in the MW E-field and at a reduced depth of field. These values, including the spatial resolution, standard deviation, and the sensitivity, are all limited by the CCD camera and the imaging system. The sensitivity is additionally limited by the CCD camera readout time. Large improvements can be obtained with a more sensitive and faster CCD camera or a multichannel spatially sensitive detector. Thus, the proof-of-principle measurements of the Rydberg atom-based subwavelength imaging technique can be significantly better with more engineering of the detection system.

Within the uncertainty of the experiments, the subwavelength imaging requires the experiment setup to be free of the geometry of the vapor cells. To meet this requirement, two room temperature Cs vapor cells are used for the experiment. One
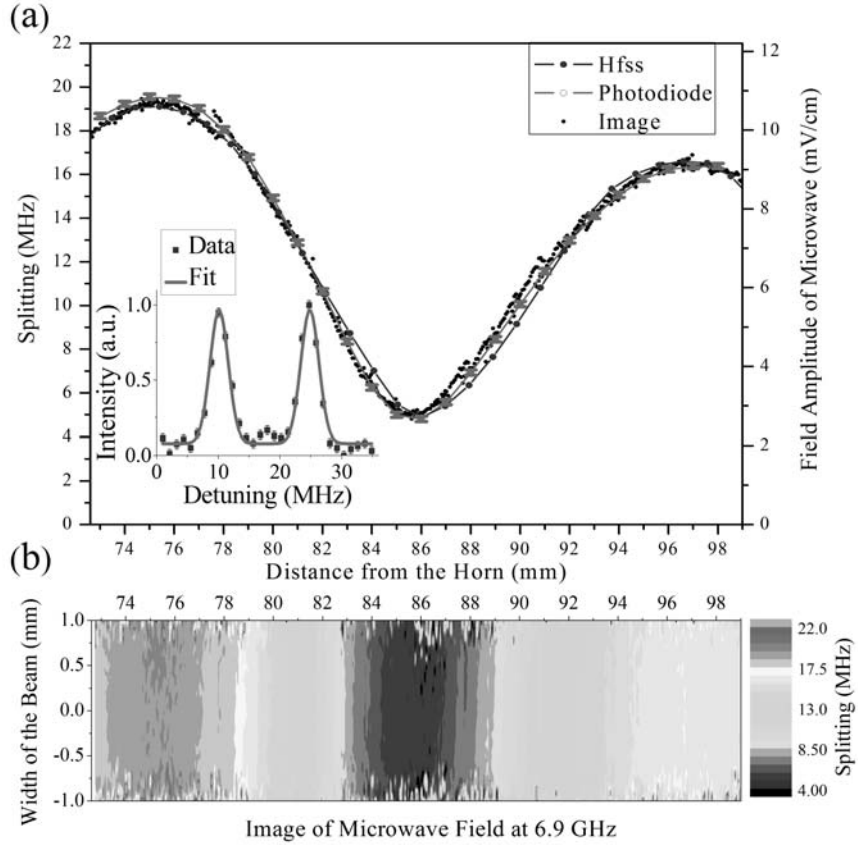
Figure 4.3: (a) Measurement of the EIT dark state splitting versus distance from the horn antenna. The theoretical FE calculation (blue), photodiode measurement (red) and image measurement data (black) are shown for a trace taken along the centerline of the image. The right hand axis shows the MW E-field amplitude that corresponds to the EIT dark state splitting (b) Two-dimensional image of the MW E-field. The data is composed of 26 images with a step size of 1 mm in the direction along the cavity axis, x. In the transverse, y, direction, a 2 mm cross-section with the zero point at the center of the probe beam is displayed. The legend shows the EIT dark state splitting in MHz. The error bars show the standard deviation between the photodiode and imaging measurements.

vapor cell is made of quartz with a square cross-section, $1\,\text{cm} \times 1\,\text{cm} \times 3\,\text{cm}$; the second vapor cell is made of pyrex with a cylindrical cross-section, $2.5\,\text{cm}$ diameter and $4\,\text{cm}$ long. Each cell was evacuated to $< 3 \times 10^{-9}\,\text{Torr}$ before it is filled with a Cs vapor. A 3-dimensional Helmholtz coil is utilized in the experiment setup to cancel residual magnetic fields, which disturbs the MW E-field measurements. An anechoic box is placed around the setup to reduce reflections and stray MW E-fields. For all the measurements, the vapor cell is placed in a region of the test MW E-field where the field is maximally uniform along the length of the vapor cell, i.e. the propagating direction of the probe laser.
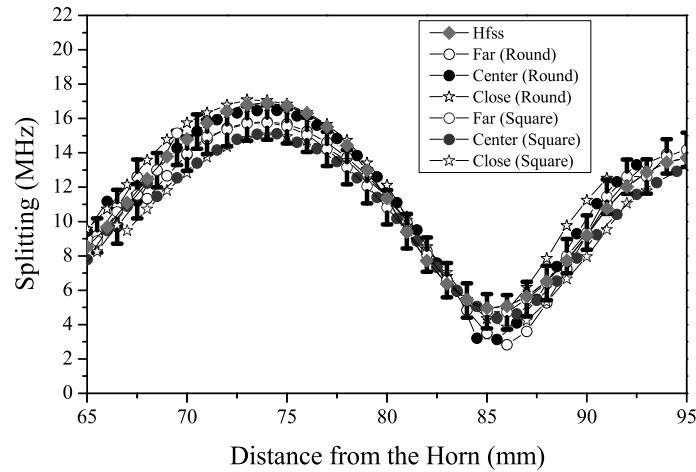

Figure 4.4: Photodiode measurement of the EIT splitting versus distance at different positions of the probe beam for square (blue) and cylindrical (black) cells compared to the FE calculations (red). The representative error bars are the standard deviation of the measurement from the theory.

To further check the measurements of the standing wave pattern with the two

vapor cells, an iris is used in front of a photodiode to filter the probe signal and the AT splitting are recorded at three different horizontal positions across the square and cylindrical vapor cells. The size of the probe beam is $\sim 500\,\mu\text{m}$. The spots of the measurement were spaced horizontally by a separation of $1\,\text{mm}$ along the x-direction on the centerline of the vapor cells. The data obtained for the measurement using the iris is compared to the results of the FE calculation as shown in Fig. 4.4. The results obtained for the two different vapor cells show that the signal, within the uncertainty of subwavelength imaging, is independent of the size and the composition of vapor cells. To explain the observation to a great extent, the wavelength of the MW E-field, λ_{MW}, should be longer than the dimensions of either vapor cell as used in this experiment and the dielectric constant of vapor cell walls should be as close to that of vacuum as possible. The primary observable effect caused by the presence of the vapor cells is an increase in the optical path length of the MW cavity, which can be observed as a shift in the fringe of the standing wave pattern. This effect has been removed from the plot shown in Fig. 4.4. As shown in Fig. 4.4, the field variations where the low vs. high MW E-field measurements corresponding to the two vapor cells invert themselves over the extent of the scan. This observation indicates that the MW E-field errors in the measurement are not correlated with a particular vapor cell.

4.6 Near-field imaging

The experiments described here show that the Rydberg atom-based method has the ability to detect subwavelength MW E-fields with a high spatial resolution,
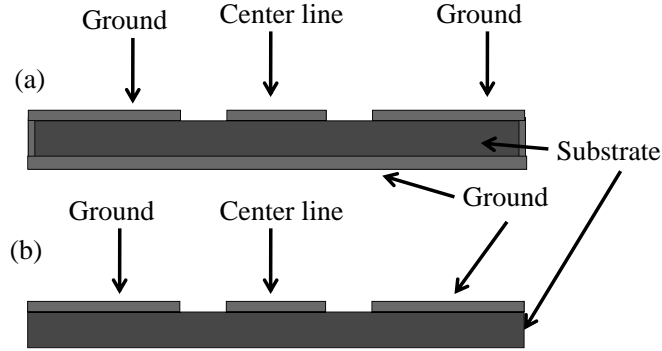
Figure 4.5: The profiles for two kinds of CPW (a) a conductor-backed
CPW; (b) a conventional CPW.

$\sim \lambda_{\mathrm{MW}}/650$. This ability offers the possibility to measure MW E-field distributions in
near-field regime of arbitrary electric structures without significantly distorting the
target field. Although the ability to measure near-field MW E-fields is necessary for
many MW applications, there is no direct near-field measurements for conventional
dipole antennas because the conducting material of the probe disturbs MW E-fields.
This section will show that the Rydberg atom-based method can measure the MW
E-field distribution near a stripline waveguide on a printed circuit board, known as
coplanar waveguide (CPW).

4.6.1   Experiment setup with Coplanar waveguide

A CPW is a type of electrical transmission line that can convey MW signals. A
conventional CPW is fabricated on a dielectric substrate with a center strip conductor
and semi-infinite ground planes on either side. There is also other kinds of CPW, such
as conductor-backed CPWs whose conductor on the back is grounded as shown in Fig.

4.5(a). In this chapter, a conventional CPW is fabricated. The conventional CPW minimizes the reflection of the MW E-fields because there is no conductor at the back of the substrate.
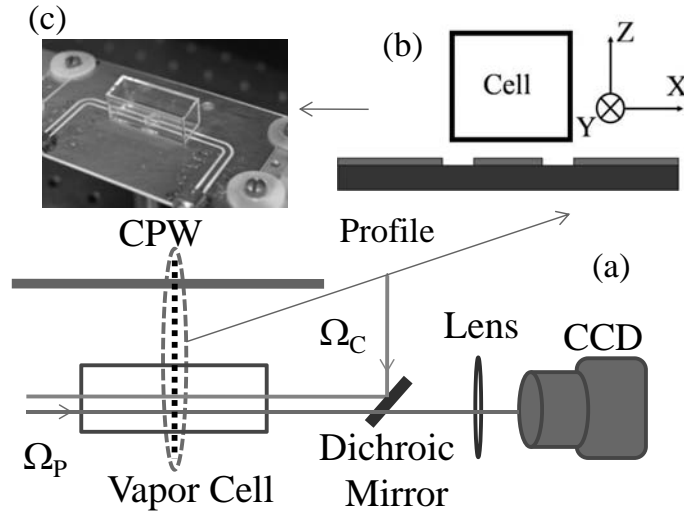

Figure 4.6: The experiment setup for near-field imaging. (a) The lasers and imaging system in near-field regime of a CPW; (b) the profile of the vapor cell and the CPW; (c) a picture of the vapor cell and CPW in experiment.

The experiment setup is shown in Fig. 4.6 (a). The lasers, the vapor cell and the imaging system are the same as the standing wave experiment described in Section 4.3. A CPW replaces the horn antenna and is placed near the vapor cell. The profile of the vapor cell and the CPW is shown in Fig. 4.6 (b). The geometry of the CPW can be easily constructed in HFSS to simulate the near-field pattern with FE method. Fig. 4.6 (c) is a picture showing the CPW near a vapor cell in experiment.

4.6.2 Results

To check the accuracy of the near-field measurement, the experimental data of the MW E-field right above a CPW are shown with a comparison to the numerical results of the FE calculation. The CPW was operated at a frequency of 12.602001 GHz, $\lambda_{\mathrm{MW}} = 2.3805743$ cm. The MW E-field drives the $39\mathrm{D}_{5/2} \longleftrightarrow 40\mathrm{P}_{3/2}$ transition. The Rabi frequencies of the probe and coupling lasers were 2.03 MHz and 1.52 MHz, respectively. Fig. 4.7 shows the results along with the FE calculation of the cell above the waveguide. The FE calculation included the vapor cell.

The spatial resolution is 66 μm. The minimum distance where the MW E-field can be imaged is 2.7 mm above the centerline of the CPW. The MW E-field amplitude decreases when increasing the distance from the CPW. Specifically, the image data also fits with the analytic near-field pattern, $A \exp(-2\pi z/\lambda_{\mathrm{MW}})$, where A is a constant determined by a fit to the data. From the comparison of the data to the calculation, a statistical variation in the field is $120\,\mu\mathrm{V\,cm}^{-1}$. The subwavelength imaging based on Rydberg EIT in a vapor cell is successfully demonstrated in the near-field regime of the CPW. The ability to measure MW E-field in the near-field regime can benefit applications of MW technologies, such as the characterization of metamaterials and small high frequency circuits.

4.7   Conclusion

In conclusion, this chapter presented a method to image MW E-fields using Rydberg atom EIT in a Cs vapor cell at room temperature. Unlike conventional dipole
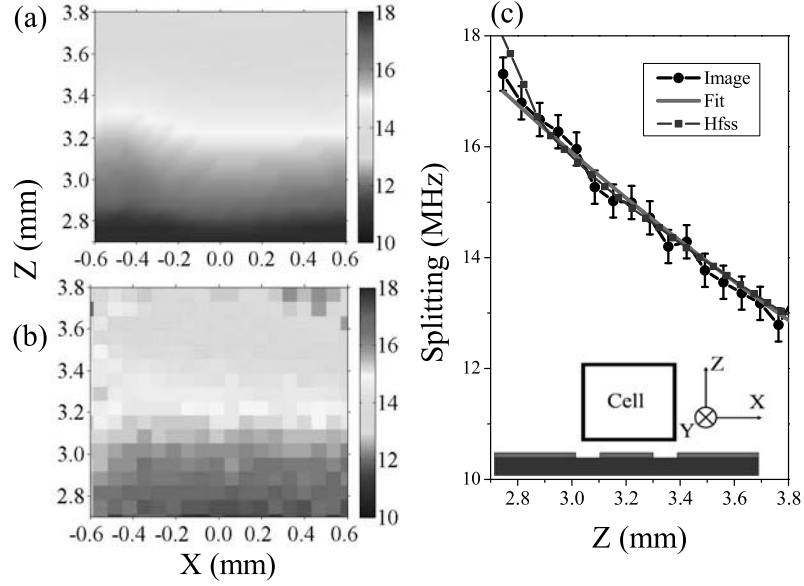
Figure 4.7: (a) This figure shows the FE calculation directly above the microwave coplanar waveguide (CPW) where the MW E-field was sampled. (b) This figure shows the imaging data corresponding to (a). (c) This plot shows a comparison between the data and the FE calculation along the z-axis at $x = 0$. $x = 0$ is at the center of the CPW. Solid circles (black) are the imaging data while the solid squares (blue) are the FE calculation. The line (red) is a plot of $A\exp(-2\pi z/\lambda_{\mathrm{MW}})$, where A is a constant determined by a fit to the data. The geometry is shown in the inset of (c).

antennas that are made of conducting materials, the probe for MW E-fields is an atomic vapor in a dielectric cell that barely disturbs the target field. By mapping a MW E-field standing wave and the near field region above a CPW, very high spatial resolution has been demonstrated at MW E-field resolutions similar to the best so far achieved in absolute measurements. The resolution of the subwavelength imaging is limited by the optical detection system. This MW E-field imaging method promises a wide range of applications, particularly in the area of characterizing metamaterials and small MW circuits. The method can be improved by using better imaging detectors and smaller vapor cells [97]. It may be possible to measure much smaller MW E-fields at higher sensitivity, determined by the Rydberg state lifetime. Achievement of this objective could allow MW E-field imaging at field strengths $< 10\,\mathrm{nV\,cm^{-1}}$ with $< 10\,\mu\mathrm{m}$ spatial resolution.

Chapter 5

Effect of Vapor Cell Geometry on Rydberg Atom-based MW E-Field Measurements

5.1   Introduction

This chapter presents the experimental investigation on how the vapor cell geometry affects the accuracy of the absolute MW E-field measurements. One of the important factors affecting the accuracy of the MW E-field measurement is the Fabry-Perot effect. The Fabry-Perot effect is dependent on the ratio of vapor cell size, D, to the MW E-field wavelength, λ_{MW}, i.e. D/λ_{MW}. By making the ratio of vapor cell size to wavelength small, the experiment shows that the accuracy is greater than current methods in the frequency range, 10-30 GHz, and is not limited by the vapor cell geometry provided $D/\lambda_{MW} < 0.1$.

5.2   Motivation

To apply Rydberg atom-based MW E-field detection in practice, the accuracy of the method needs to be studied. The vapor cell is one of the factors that determines the accuracy. Atoms are confined in a vapor cell which is typically made of pyrex or quartz. MW E-fields can be absorbed or reflected by the walls of the vapor cells. Although the reflection and absorption can be made to be small by choosing suitable materials, variation of the MW E-field can arise from the Fabry-Perot (FP) effect, absorption by the vapor cell surface as the MW E-field passes through to interact

with the atoms and polarization of the vapor cell. The FP effect is due to reflections of the MW wave inside the vapor cell. When a MW wave is incident into a hollow glass vapor cell, standing waves can develop inside the vapor cell due to reflections from the glass walls, forming a MW FP cavity. The distribution of the E-field inside the vapor cell will vary depending on the frequency of the MW E-field and on the size of the vapor cell. The FP effect can result in the measured E-field being different from the incident field, or the desired quantity. The corners and imperfections of a vapor cell can also re-scatter and re-radiate the MW E-field. Such effects also cause the measured MW E-field to be different from the incident E-field signal.

5.3   Experiment

5.3.1   The configuration of lasers

The experimental setup is shown in Fig. 5.1(a) and the energy level diagram is shown in Fig. 5.1(b). The experimental setup is similar to those described in Chapter 4, 5. The probe laser and the coupling laser are in a counter-propagate geometry. The two laser beams overlap inside the vapor cell with beam waist at the center of the vapor cell. The transitions are the same as those described in Chapter 4, 5. The probe laser, ~ 852 nm, is set to the Cs $6S_{1/2}(F = 4)$ to $6P_{3/2}(F = 5)$ transition, while the coupling laser, $\sim 508 - 510$ nm, is set to the Cs $6P_{3/2}(F = 5) \leftrightarrow nD_{5/2}$ transition shown in Fig. 5.1(b). Both lasers are locked to a high-finesse FP cavity with the linewidth of ≤ 100 kHz as described in Chapter 3. The beam radii are 156 μm for the probe laser and 210 μm for the coupling laser. Both laser beams are shaped as

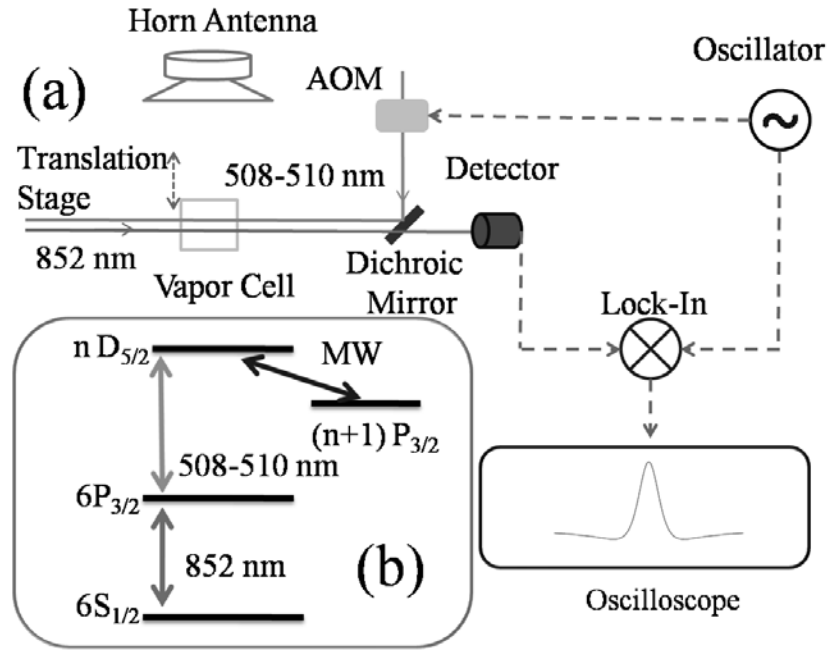Figure 5.1: Setup and energy level diagram for the experiments. (a) The experimental setup. The probe and coupling lasers are overlapped inside the vapor cell and the MW horn antenna is placed in the far field limit. (b) The energy level diagram. The 852 nm and $508 - 510$ nm lasers are the EIT probe and coupling lasers, respectively. The MW E-field couples to the $nD_{5/2} \leftrightarrow (n+1)P_{3/2}$ transitions.
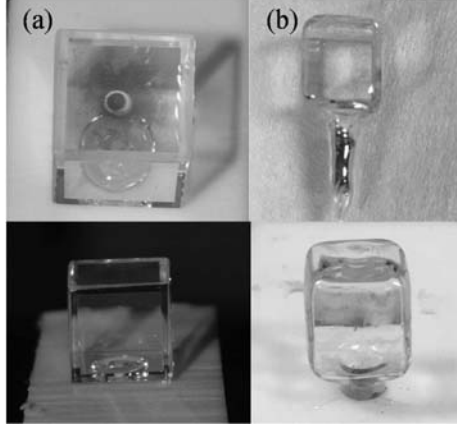
Figure 5.2: The vapor cells used in the experiment. (a) The vapor cell with 8 mm inner diameter and 1 mm wall thickness. (b) The vapor cell with 9 mm inner diameter and 1.25 mm wall thickness.

Gaussian beams using optical fibers. A horn antenna generates MW E-fields driven by a MW signal generator.

The experiment will study the MW E-field variation at different D/λ_{MW} ratios. The size of the vapor cell, D, and the wavelength of the MW E-field, λ_{MW}, are the two important factors in the experiment. For the factor λ_{MW}, MW E-fields at different wavelengths are needed in the experiment. The MW E-field couples to the $nD_{5/2} \leftrightarrow (n+1)P_{3/2}$ transition and the horn antenna is placed in the far field regime. By changing the principal quantum number n, the 4-level EIT system will be on resonance with MW E-fields at different frequencies or wavelengths. In the experiment, the involved MW frequencies are 23.91 GHz for n = 32, 19.64 GHz for n = 34 , 17.84 GHz for n = 35, 12.06 GHz for n = 39, 8.57 GHz for n = 44, 6.49 GHz for n = 48, 3.06 GHz for n = 61, and 2.08 GHz for n = 69, respectively. The different frequencies of the MW E-fields relate to different wavelengths of the MW E-field,

λ_{MW}.

5.3.2 Vapor cells

To study the MW E-field variation at different D/λ_{MW} ratios, the other important factor is the size of the vapor cell, D. In this chapter, the size of a vapor cell is defined as the inner diameter of the vapor cell. Two cubic vapor cells are manufactured and the material of the vapor cells is pyrex, as shown in Fig. 5.2. Fig. 5.2(a) shows a vapor cell with a size of 8 mm and a wall thickness of 1 mm. So the size-to-wavelength ratios are, D/λ_{MW}, of 0.64, 0.52, 0.48, 0.34, 0.23, 0.17, 0.08, and 0.05. The size of the other vapor cell, as shown in Fig. 5.2(b), is 9 mm with 1.25 mm wall thickness, leading to size-to-wavelength ratios of 0.72, 0.59, 0.53, 0.36, 0.26, 0.19, 0.09, and 0.06. The range of D/λ_{MW} ratios is chosen according the wavelengths of the MW E-fields which vary from 1.25 cm, around the size of the vapor cells to 14.42 cm, around 10 times of magnitude more than the size of the vapor cells.

The vapor cells are placed on a translation stage and mounted on a teflon block. This allows the cross-section of vapor cell to be scanned across the lasers in order to map the field variability and distribution inside the vapor cell, similar to the experimental setups used in Chapter 4. The precision of of the translation stage is 0.01 mm. Thus, the precision of the position scanning of the vapor cells relative to the laser beams is 0.01 mm. MW absorbers are placed around the interaction area to avoid the effect of MW E-field reflections from the apparatus.

5.3.3   Data processing

To obtain high signal-to-noise ratios, the experiment applies the lock-in technique to acquire the signal. The coupling laser is amplitude-modulated with an AOM at 50 kHz. The transmitted probe signal is recorded by a photodiode and demodulated using a lock-in-amplifier. The demodulated signal from the lock-in amplifier is recorded on a digital oscilloscope.

The AT splitting, Δ, is recorded to calculate the MW E-field amplitude, E, while varying the power of the MW signal generator at the different MW E-field frequencies used for the vapor cell geometry experiments. Fig. 5.3 shows the square root of the MW power, P_{SG}, versus the measured amplitudes of the MW E-fields. P_{SG} is directly taken from the MW signal generator and the amplitudes of the MW E-fields are determined by the AT splitting. To calculate the Amplitudes of MW E-fields, the transition dipole moments between the Rydberg states, μ_{MW}, are needed. The details for the calculation of μ_{MW} are discussed in Chapter 2. Here is the values of μ_{MW} at different transitions: $\mu_{MW} = 3221.5 \; e \; a_o$ for the $69D_{5/2} \leftrightarrow 70P_{3/2}$ transition at 2.08 GHz, $\mu_{MW} = 1508.9 \; e \; a_o$ for the $48D_{5/2} \leftrightarrow 49P_{3/2}$ transition at 6.49 GHz; $\mu_{MW} = 971.2 \; e \; a_o$ for the $39D_{5/2} \leftrightarrow 40P_{3/2}$ transition at 12.60 GHz; and $\mu_{MW} = 770.0 \; e \; a_o$ for the $35D_{5/2} \leftrightarrow 36P_{3/2}$ transition at 17.84 GHz. The numerical fit shows the MW E-field amplitudes are proportional to the square root of P_{SG}. This validates the method for measuring the amplitudes of the MW E-fields in the vapor cells.

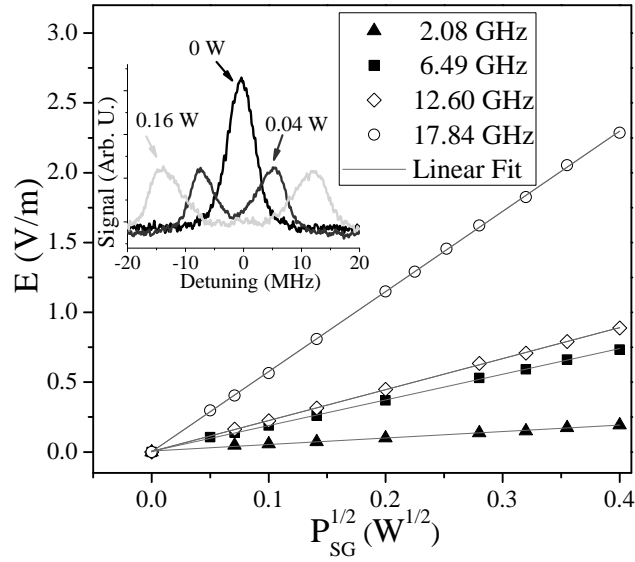Figure 5.3: Experimental data for MW E-field amplitude with a cubic vapor cell with 8 mm inner diameter as a function of the square-root of power at the MW signal generator. The MW E-field amplitudes are linearly increased with $\sqrt{P_{SG}}$ at different MW frequencies. The linear relationship between E and $\sqrt{P_{SG}}$ validates the measurement of MW E-fields in vapor cells. The inset shows raw data for 2.08 GHz.

5.4   Results

5.4.1   MW absorption by the material of vapor cells

When a MW E-field passes through a vapor cell, a fraction of the MW power is absorbed by the dielectric material that the walls of the vapor cell are made of. The absorption of the MW needs to be quantitatively calculated. Specifically, the interaction between the MW E-field and a dielectric material is dependent on the complex permittivity of the dielectric material [98],

$$\epsilon = \epsilon' + i\epsilon'', \tag{5.1}$$

where ϵ is the relative permittivity of the dielectric material, and ϵ', ϵ'' are the real and imaginary parts of complex permittivity, respectively. When a MW field incidents on the surface of the dielectric material, the dispersion of the MW E-field can be described by the real part of complex permittivity, ϵ', while the absorption is proportional to the imaginary part, ϵ''. Specifically, at a certain wavelength of a MW field, the loss tangent,

$$\mathrm{Tan}(\delta) = \frac{\epsilon''}{\epsilon'}, \tag{5.2}$$

determines the absorption fraction of the MW field. As a rule of thumb, materials with $\mathrm{Tan}(\delta) \geq 0.1$ are considered as good absorbers; while those with the loss tangent $\mathrm{Tan}(\delta) \leq 0.01$ are considered transparent to MW E-fields.

For the pyrex vapor cells involved in the MW E-field sensing experiment, the real part of the permittivity, ϵ', is ~ 4.6 and the imaginary part, ϵ'', is ~ 0.023 in the GHz MW frequency range. These yield a loss tangent of $\mathrm{Tan}(\delta) = 0.005$ for pyrex

[99]. Precisely, the MW E-field loss with propagation distance, d, inside a dielectric material is determined by,

$$E = E_0 \mathrm{Exp}\Big[-\frac{2\pi}{\lambda_{\mathrm{MW}}}\Big(\frac{\delta d}{2}\Big)\Big],\eqno(5.3)$$

where E_0 is the incident MW E-field amplitude and E is the transmitted MW E-field amplitude. For a MW E-field at a frequency of 12.6 GHz, the absorption by 1 mm of pyrex is 0.066%. Thus, the absorption effects of the MW by the vapor cell walls are small and can be ignored in this experiment.

5.4.2   Fabry-Perot effect of MW inside vapor cells

Given the absorption of the MW E-field is negligible, the dominant effect in the Chapter is the FP effect caused by the reflection of the MW E-field by the vapor cell walls. Fig. 5.4. shows the experimental data indicating the variation of the MW E-field inside the vapor cells for different D/λ_{MW} ratios. The results show that the variation of the MW E-field reduces when decreasing the D/λ_{MW} ratio. This observation is consistent with the theory of a FP cavity as discussed in the Motivation section. The interference between the incident MW and reflected MW is produced when the wavelength of the MW E-field is comparable to the size of the vapor cells, D. When D is smaller than $\sim \lambda_{\mathrm{MW}}/4$, the interference inside the vapor cell is greatly reduced in magnitude because the vapor cell is not large enough support a resonance. The cross section for MW scattering also is decreased as the vapor cell size is smaller than λ_{MW}. To quantify the interference effect of the MW E-field, the data at different D/λ_{MW} ratio was fit using a Taylor expansion of the MW E-field. Assumed the
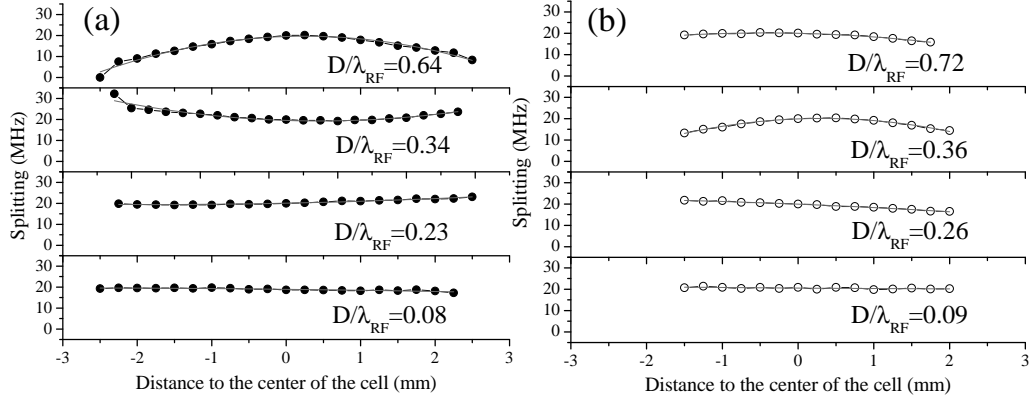
Figure 5.4: Data generated by scanning the position of the EIT detection beams through the vapor cells at different D/λ_{MW} ratios where D is the size of the vapor cells and λ_{MW} is the wavelength of MW E-field. The experiment involves two vapor cells both of which show the same effect. The black dots represent the 8 mm inner diameter vapor cell, and the hollow circles represent the 9 mm inner diameter vapor cell. The red lines are a quadratic fit. The variation becomes smaller as D/λ_{MW} decreases. The distance is measured from the vapor cell wall where the MW E-field is incident, while the vertical axis is the AT splitting caused by MW E-field.

incident MW E-field is a plane wave, the Taylor expansion of the MW E-field should be a constant if there is no FP effect caused by the reflection of the vapor cell walls. Higher order terms of the Taylor expansion indicate variation of the MW E-field in the vapor cell. For example, the quadratic term indicates the curvature of the MW E-field.

The fits show that the field variation is $\sim 1\%$ when the D/λ_{MW} ratio is smaller than 0.1. The 1% variation mostly arises from the measurement uncertainties of the AT splitting that determines the MW E-field amplitude. For example, when fitting the data for $D/\lambda_{MW} = 0.09$ as shown in Fig. 5.4, the average value of the AT splitting is 20.51 MHz and the standard variation of the fitting is ± 0.14 MHz. This gives a variation of $\leq \pm 0.7\%$ for the measured amplitudes of MW E-fields. The average MW E-field variation of the linear term is $\sim 1\%$ across the vapor cell while the average variation of the quadratic term across the vapor cell is $\sim 0.3\%$. Higher order terms than the quadratic one are much smaller than $\sim 0.3\%$. Therefore, the experimental results indicate that under the condition of $D/\lambda_{MW} \leq 0.1$, the MW E-field across the vapor cell is approximately constant. Moreover, it is difficult to distinguish the variation of the MW E-field at the level of $\sim 1\%$, which is also the level of the statistical uncertainty of the measurement. The fact that higher order terms are much smaller indicates that, under the condition of $D/\lambda_{MW} \leq 0.1$, the MW E-fields are barely perturbed by the vapor cell at the level of the statistical measurement error.
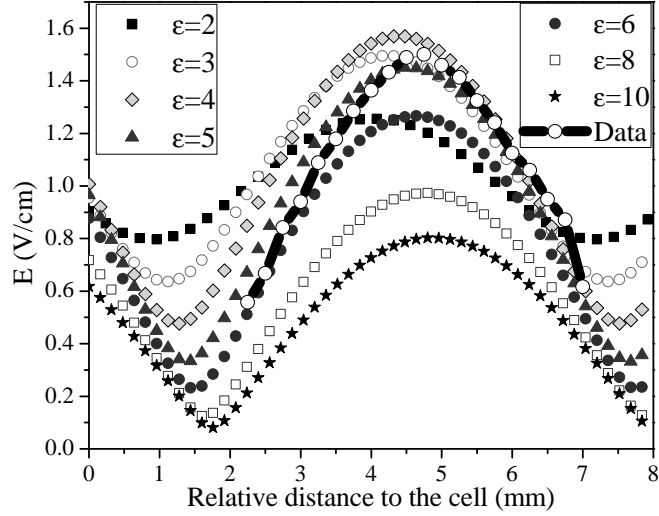
Figure 5.5: 1D model results for the *E*-field variability between two 1 mm thick glass walls separated by 8 mm for different dielectric constants at 23.93 GHz.

5.4.3 Comparison of the experimental results to calculations

Two different theoretical models are used to further support the experimental results. There are two effects when a MW E-field is incident onto a glass vapor cell. One effect is the MW FP effect described above and the other is MW polarization change caused by the vapor cell walls which leads to MW energy scattering, particularly at the corners of the vapor cell. The experimental results show that the FP effect is the dominating one. To numerically simulate the effect, the two theoretical models are a full 3-dimensional (3D) finite element (FE) model of the vapor cell and a simple analytic 1-dimensional (1D) 5-layer material model. Given the FE method uses a full 3D model, the geometry of the vapor cell is modeled to determine the field variation inside the vapor cell, which includes both the FP cavity effect and the scattering

effects of MW inside the vapor cell.

The 1D 5-layer analytical model is more straightforward compared to the FE calculations and can be used to isolate the MW FP cavity effects. In the 5-layer model, the field variation inside the vapor cell can be approximately estimated with five different regions: the region inside the vapor cell, the two glass walls and the surrounding free-space. The glass walls are 1 mm thick. The vapor cell walls extend to infinity such that the vapor cell in the model has no corners. Therefore, the E-field variation between the two glass walls can be easily determined analytically with a layered media approach [100]. The MW E-field is normally incident into the vapor cell. The two glass walls are separated by a distance D effectively forming a planar FP cavity.

Fig. 5.5 shows calculations of the amplitude variation of the MW E-field inside the vapor cells for different dielectric constants of vapor cell walls using the 1D analytical model. The experimental data is also shown in Fig. 5.5 for the $32D_{5/2} \leftrightarrow 33P_{3/2}$ transition at 23.93 GHz. The separation between the walls is D = 8 mm. Fig. 5.6 shows the variation of the MW E-field for a pyrex vapor cell at different frequencies. Because the dielectric constant can vary from the manufacturing process, the results are simulated for dielectric constant $\epsilon = 3.0 - 5.0$. The overall thickness of the vapor cell and the walls make it difficult to determine ϵ for the simulations. The results for the different dielectric constants are qualitatively the same as shown in Fig. 5.6. The results of the 1D analytical model show the same type of FP resonances as observed in the experimental data. The comparison of the 1D model results and the experimental
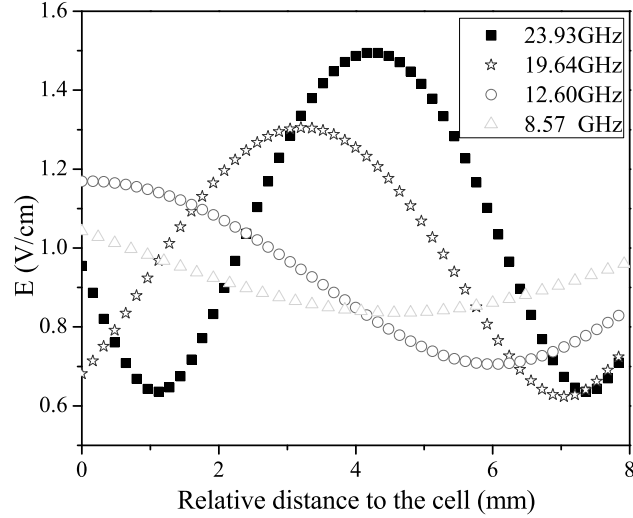
94

Figure 5.6: 1D model results for the E-field variability between two 1 mm

thick pyrex walls separated by 8 mm for different frequencies.

data suggest that the variation of the MW E-field is primarily due to the FP effect,

thus can be reduced by using vapor cells with smaller D/λ_{MW} ratios.

Both the FP effect and the polarization change of the vapor cell due to the

scattering are taken into account in the 3D FE model, which is a detailed model that

allows for better comparison to the experimental data. Fig. 5.7 shows a comparison

between the calculation using the FE model and the experimental data for the variation

of the MW E-field inside the vapor cell at different frequencies. The results of the 3D

FE calculation are similar to those obtained with the 1D analytic model as shown in

Fig. 5.6. The similarity again indicates that the dominate effect causing the E-field

variation inside the vapor cell is the FP cavity effect rather than the scattering effect

caused by the vapor cell corners.

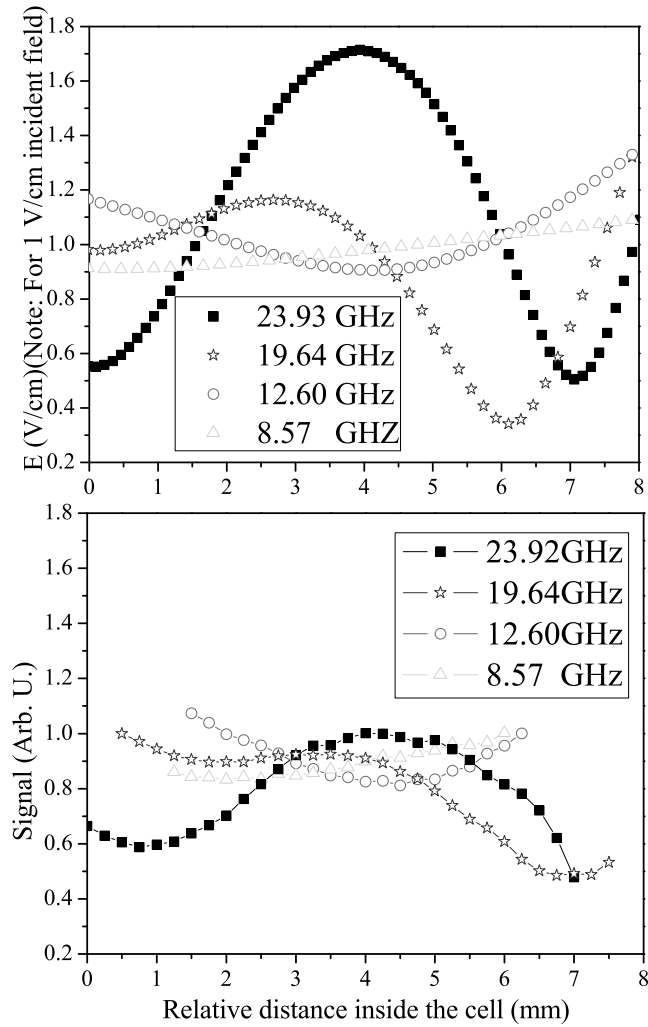Fig. 5.7 also shows that FE calculations qualitatively agree with the experimental

Figure 5.7: MW E-field pattern in the cubic vapor cell with 8 mm inner diameter and 1 mm wall thickness. The upper plot is the results of the 3D FE model and the lower plot is the experimental results.

data. The main difference between the experiment results and the 3D FE calculation is a result of surface imperfections of the vapor cell surfaces. The MW E-fields are scattered when hitting the imperfections. The imperfections also change the polarization of the MW E-fields. Thus, the measured values of MW E-fields are different from the calculated MW E-fields inside vapor cells. The imperfections of vapor cells are induced by the high temperature that is needed to seal the vapor cells during manufacture process. The imperfections can be eliminated by using a better fabrication process that is free of high temperature, like anodic bonding [66, 101].

By the comparison of the results from the 1D model, the FE model, and the experimental data, it is shown that the variation of the MW E-field inside the vapor cell is dominated by the FP cavity resonances which can affect the accuracy of an atom-based E-field measurement. However, the results show that this E-field variation can be reduced dramatically by making the vapor cell dimension small compared to wavelength of the MW E-field, i.e. $D/\lambda_{MW} \ll 1$. When the vapor cell is designed to eliminate FP resonances, the E-field variation is less than the statistical accuracy of current measurements.

5.5   Conclusion

This Chapter experimentally investigated one aspect of the accuracy of the Rydberg atom-based MW E-field measurements. The experimental results show that the D/λ_{MW} ratio and the dielectric constant of the vapor cell affects the accuracy of Rydberg atom-based MW E-field measurements. Specifically, the variation inside the

vapor cell and absorption by the vapor cell walls can ultimately affect the over-all uncertainty of a vapor cell Rydberg atom-based E-field measurement. The variation of the MW E-field inside the vapor cell is smaller than $\pm 0.7\%$ when the D/λ_{MW} ratio is less than 0.1. This value leads to ± 0.03 dB uncertainties in the magnitude of the MW E-field. By selecting a proper D/λ_{MW} value and vapor cell material, the uncertainty due to the vapor cell can be controlled and reduced to less than current MW E-field measurement uncertainties. The accuracy of Rydberg atom-based MW E-field measurements are currently not limited, in principle, by the vapor cell or its geometry.

Chapter 6

Dispersive Radio Frequency Electrometry using Rydberg atoms in a Prism-shaped Atomic Vapor Cell

6.1 Introduction

In this chapter, an alternative method is introduced to measure MW E-fields using a prism-shaped vapor cell filled with cesium (Cs). The MW E-field amplitude is determined by observing the deflection of a probe beam. A MW E-field induces a change in the index of refraction of the atomic media. The change in the index of refraction results in a small displacement of the probe laser beam on a spatially sensitive photo-detector. The method obtained a spectral angular dispersion $d\theta/d\lambda \approx$ 0.82 rad nm^{-1}, at a minimum angle change of ~ 0.0242 rad or $\lambda/\delta\lambda \approx 3.2 \times 10^{10}$, corresponding to a MW E-field of ~ 8 μV/cm with a sensitivity of ~ 46 μVcm^{-1}Hz$^{-1/2}$.

6.2 Motivation

So far, the work that has been done on Rydberg atom-based electrometry has focused on the absorptive features of the atomic vapor [39, 37, 102]. Along with absorption, there is always a dispersive part of the signal. The dispersive signal corresponds to changes in the index of refraction. According to Snell's law, the induced change in the index of refraction can lead the probe laser beam to deflect as it traverses a prism-shaped vapor cell [103, 104]. The MW E-field amplitude is

determined by measuring the change in the index of refraction caused by the MW E-field. Such a measurement can be more immune to some types of noise sources such as the power fluctuations of the read-out lasers. Thus, the MW E-field sensing using dispersive signals offers advantages under certain circumstances such as phase sensitive detection [105]. There are several successful examples for applications using dispersive signals. The properties of dispersive resonances have been used for magnetometery due to their high sensitivity to small magnetic fields [106]. The deflection of the probe beam in an EIT process from a prism-shaped vapor cell has been demonstrated for a 3-level EIT scheme [107] and can be used to separate pump, signal, and idler beams in a four-wave mixing process [108].

Section 6.3 gives the theoretical description on how a MW E-field induces changes in the index of refraction with Rydberg EIT system. Section 6.4 describes the experiment setup for the MW E-field measurement using a prism-shaped vapor cell. In section 6.5, the results for the MW E-field measurement is presented. The applications of the method using dispersive signals are also discussed. A short summary is given in section 6.7.

6.3   Theory

To understand how the displacement changes with the presence of a MW E-field, it is necessary to understand the the behavior of the probe beam within a prism-shaped vapor cell. Snell's law describes how a light beam propagates through a prism. Prism-shaped vapor cells filled with alkali atoms, known as atomic prisms, can cause

an output beam to deflect as the index of refraction changes. Specifically, if a probe laser is scanned in frequency in the presence of a coupling laser beam near an EIT resonance, the probe beam will be deflected as the index of refraction changes near the resonance. The frequency dependent deflection angle is determined by the change in index of refraction at the probe laser frequency.

6.3.1 Theoretical model

To calculate the deflection angle induced by a MW E-field, we still consider a 4-level ladder-type EIT system as described in Chapter 2. The difference is that the real part of the transition matrix element, $\text{Re}[\rho_{12}]$, is calculated. $\text{Re}[\rho_{12}]$ relates to the index of refraction that causes the probe deflection. As shown in Fig. 6.1, the probe beam excites the $6S_{1/2} \leftrightarrow 6P_{3/2}$ ($|1\rangle \leftrightarrow |2\rangle$) transition and the coupling beam excites the $6P_{3/2} \leftrightarrow 52D_{5/2}$ ($|2\rangle \leftrightarrow |3\rangle$) transition. The MW E-field couples to the Rydberg transition, $52D_{5/2} \leftrightarrow 53P_{3/2}$ ($|3\rangle \leftrightarrow |4\rangle$). Both the probe and coupling lasers are circularly polarized.

As described in Chapter 2, the solution for the transition matrix element, ρ_{12}, can be obtained by using the density matrix under the rotating wave approximation. Thus, the complex probe susceptibility used to calculate the probe beam deflection is given by,

$$\chi(\omega_p) = -\frac{2\mu_p \mathcal{N}}{\epsilon_0 E_p}\rho_{12}(\omega_p), \tag{6.1}$$

where μ_{p} is the dipole matrix element for the probe transition, E_{p} is the probe E-field, ω_{p} is the probe frequency, and $\mathcal{N}$ is the atomic density. The motion of the atoms

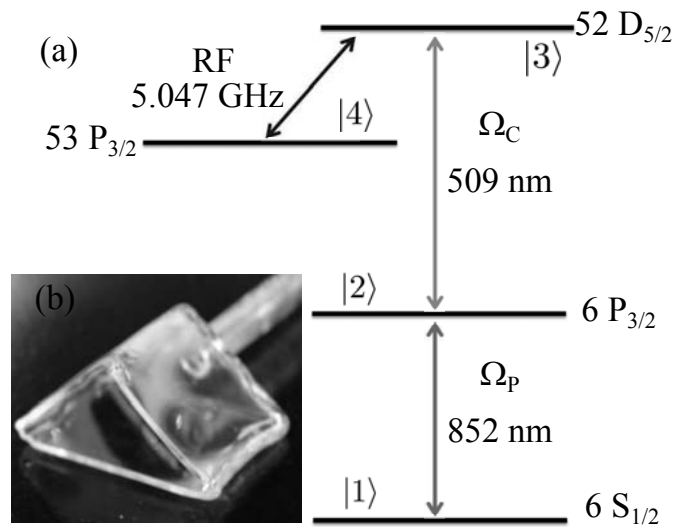Figure 6.1: (color online) (a) Four-level cesium (Cs) atomic system coupled to two laser fields on transitions $6S_{1/2} \leftrightarrow 6P_{3/2}$ and $6P_{3/2} \leftrightarrow 52D_{5/2}$ with Rabi frequencies Ω_P and Ω_C, respectively. The $52D_{5/2} \leftrightarrow 53P_{3/2}$ transition couples to the MW E-field at a frequency of 5.047 GHz. (b) A picture of the prism vapor cell filled with natural abundance of Cs.

leads to Doppler broadening. The transition matrix element $\rho_{12}(\omega_p)$ including the Doppler effect is obtained by integrating over a Maxwellian velocity distribution at the vapor cell temperature, T = 300 K [109]. The probe absorption and dispersion are proportional to the imaginary and real parts of the susceptibility, respectively. The real part of the susceptibility gives the refractive index of the medium,

$$n(\omega_p) \approx \sqrt{1 + 4\pi Re[\chi(\omega_p)]}. \tag{6.2}$$

As a result, the change in the index of refraction is dependent on the dispersive part. In the experiment we observe the dispersive part of the susceptibility, but the absorptive part of the susceptibility.

The probe laser beam passes into a prism-shaped Cs vapor cell as shown Fig. 6.2(a). The angle of incidence $\theta_p/2$ and angle of refraction θ_1' are also shown in Fig. 6.2(b). At the second surface, the beam is similarly refracted. If a position sensitive detector (PSD) is placed at distance L from the prism vapor cell, the displacement on the PSD is given by $\Delta x = L \cdot \tan(\Delta\theta(\omega_p))$, where $\Delta\theta(\omega_p)$ is the deflection angle. In the limit of small angle, the $\tan(\Delta\theta(\omega_p)) \approx \Delta\theta(\omega_p)$. $\Delta\theta(\omega_p)$ depends on the refractive index variation in the atomic prism. The relationship between the deflection angle and the index of refraction change is,

$$\Delta\theta(\omega_p) \approx 2\tan(\theta_p/2)\Delta n(\omega_p). \tag{6.3}$$

Equation (6.3) links the probe beam deflection to the index of refraction change under the assumption that the deflection angle $\Delta\theta(\omega_p)$ is much smaller than the apex angle

θ_p. Thus, the displacement measured on the PSD can be given in terms of $\chi(\omega_p)$,

$$\Delta x \approx \frac{4\pi L \tan(\theta_p/2)}{\sqrt{1 + 4\pi Re[\chi(\omega_p)]}} \Delta Re[\chi(\omega_p)]. \tag{6.4}$$

6.3.2 Superradiance

In the calculation, superradiance is an important dephasing effect that needs to be considered. Superradiance between Rydberg states is much stronger than for the ground state atoms because the transition wavelength between Rydberg states is long compared to the sample size [110, 111]. The transition wavelength between nearby Rydberg states is usually larger than the size of the vapor cell where the Rydberg atoms are created. As a result, superradiance can potentially play a role in decay and dephasing process. The emission rates between the Rydberg states, $52D_{5/2}$ and $53P_{3/2}$, can be estimated by $\Gamma_{Ryd} = (\omega^3 n \mu^2)/(3\pi\epsilon_0\hbar c) \approx 2\pi \times 0.0044$ Hz, where ω is the transition frequency between the Rydberg states, $2\pi \times 5.047$ GHz, n is index of refraction, ~ 1, μ is the transition dipole moment,~ 1720 e a_0, and ϵ_0 is the vacuum permittivity. In the experiment, the number of Rydberg atoms are estimated in the interaction volume to be N $\sim 1.6 \times 10^5$ corresponding to Rydberg density $\sim 3.1 \times 10^7$ cm^{-3}. The number of thermal photons in the field of $2\pi \times 5.047$ GHz is $N_v \sim 1200$. The maximum superradiance decay rate is $\Gamma_{Sup} = \Gamma_{Ryd} \cdot N \cdot N_v \approx 2\pi \times 700$ kHz indicating that the superradiance is important in the experiment.

However, there is not a signature of superradiance observed in the work of this chapter. It suggests that the picture here is considerably oversimplified. If the initial phases of the atomic oscillators are not correlated and/or change randomly due to

relaxation and dephasing, superradiance will be suppressed and in the extreme case will not occur at all. In this experiment, it is important to realize that the Rydberg states have hyperfine structure which are split in the background magnetic field. For example, the Rydberg atom D-state have 48 sub-states with hyperfine quantum numbers $|F, m_F\rangle$. Each transition out of these states can produce a photon with a different energy and polarization considering the shifts and natural width of the associated Rydberg transition. In addition, there is inhomogeneous broadening and the effect of the laser linewidth that are also spectrally broader than the linewidths of the Rydberg transitions. The supradiance is negligible compared to these broadening effects. The fits to the data show that this is a valid approximation.

6.4 Experimental method

6.4.1 Experimental setup

In section 6.3, equation 6.4 gives the relation between the displacement and the dispersive signal. This section gives the experimental setup that is used to directly observe the displacement. The experimental setup is shown in Fig. 6.2(a). The probe and coupling lasers are configured in a counter-propagating geometry. Both lasers are locked to an ultra-low expansion cavity using the Pound-Drever-Hall technique. The radius of the probe (coupling) laser beam is 0.40 ± 0.01 mm (0.50 ± 0.01 mm) with a Rayleigh range of 1.75 m. The probe laser power is 20 μW resulting in $\Omega_P = 2\pi \times 7.0$ MHz. The coupling laser power is 4 mW corresponding to $\Omega_C = 2\pi \times 0.5$ MHz. The MW E-field at a frequency of 5.047 GHz, resonant with
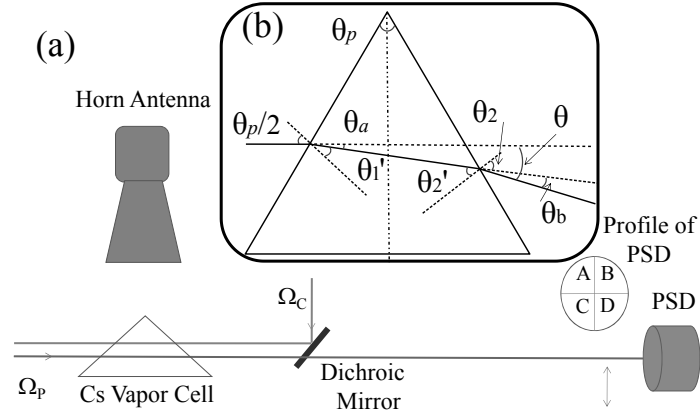
Figure 6.2: (color online) (a) Experimental setup. The two laser fields counterpropagate through the prism vapor cell and the MW E-field is supplied by a horn antenna perpendicular to the laser propagation direction. The probe beam with a Rabi frequency Ω_P passes through a dichroic mirror and is incident on a position sensitive detector (PSD). The detection area of the PSD is divided into four parts, as shown in the inset. The quadrants give the PSD three channels, which can detect the total transmission signal, and the displacement signal in the horizontal and vertical directions. (b) A diagram for the probe beam path when it traverses the atomic prism. The apex angle of the prism is θ_{p}, and the incident angle of the probe beam is $\theta_{\mathrm{p}}/2$.

the Rydberg transition, $52D_{5/2} \rightarrow 53P_{3/2}$, is generated by a horn antenna driven by a MW signal generator, HP 8340B. The homemade vapor cell is made of pyrex with an apex angle of $\theta_p = 105°$ and filled with a natural abundance of Cs after being pumped down to 10^{-9} Torr. The experiment is performed at room temperature, T = 300 K.

The PSD is placed 1 m away from the prism to capture to deflection signal of the probe beam. The PSD is within the Rayleigh length of the probe laser so that the divergence of the laser can be neglected. As the beam moves on the PSD, the signals falling on the different quadrants can be used to measure the beam displacement. To observe the index of refraction changes in the experiment, the probe beam is aligned to the center of the PSD when observing Rydberg EIT without an MW E-field incident. In this way, the probe beam will move relative to the center of the PSD as the MW E-field is applied. The displacement of the probe beam can be calibrated by placing the PSD on a translation stage. The displacement of the probe beam is substantially smaller than the beam sizes, so the probe and coupling beams overlap inside the vapor cell during the experiment.

6.4.2 Dephasing

In the experiment, the factors contributing to the dephasing rates are considered. The transit time broadening, Γ_t, is one of the dominating factors. The beam size, 0.4 mm in radius and the most probable velocity, v $\sim$ 192 m/s give a transit time broadening rate of $\Gamma_t \approx 2\pi \times 36$ kHz for the beam overlap region[112]. The Rydberg-ground state collisional dephasing rate is $\Gamma_{coll} \approx 2\pi \times 10$ kHz at room temperature
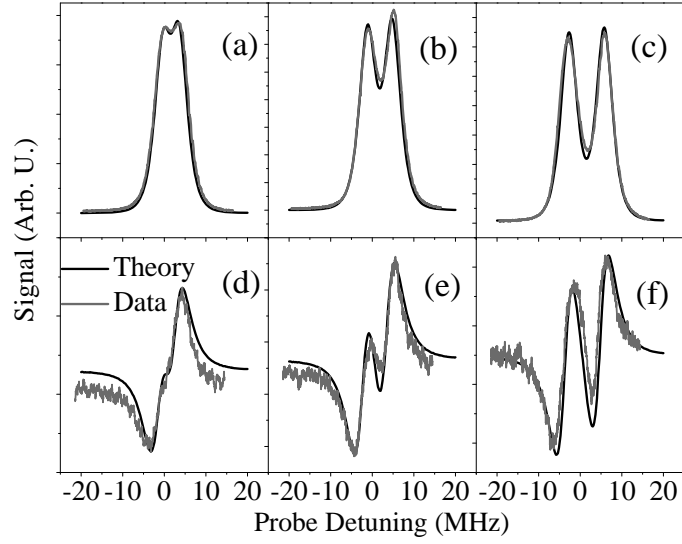
Figure 6.3: (color online) AT splitting and the displacement signal with a MW E-field. The Rabi frequency of the probe laser is $\Omega_P = 2\pi \times 7.0$ MHz. The Rabi frequency of the coupling laser power is $\Omega_C = 2\pi \times 0.5$ MHz. The top panel (a-c) is the absorptive signal with MW E-field both in theory and experiment. The AT splittings caused by the MW E-field are (a) $2\pi \times 2.0$ MHz ($\sim 1497\mu$V/cm), (b) $2\pi \times 4.0$ MHz ($\sim 2995\mu$V/cm), and (c) $2\pi \times 8.0$ MHz ($\sim 5990\mu$V/cm), respectively. The frequency of the MW E-field is tuned 0.3 MHz away from the resonant frequency to show the the effect of frequency variation of the MW E-field. The bottom panel (d), (e), and (f) are the displacement signals with MW E-field amplitudes, the same as shown in (a), (b), and (c), respectively. Black denotes numerical results, while red is experimental data. The zero point of the probe detuning on the frequency axis is the resonance point of the 4-level EIT system.

with $\sim 1.2 \times 10^{-6}$ Torr of Cs atoms in the vapor cell [113]. The laser dephasing rate is $\Gamma_\mathrm{l} \approx 2\pi \times 100$ kHz estimated by the error signals of the probe and coupling lasers locked to the cavity. The inhomogeneous magnetic field dephasing rate is $\Gamma_\mathrm{m} \approx 2\pi \times 100$ kHz, calculated by considering the Zeeman splitting of the atomic levels caused by the maximum magnetic field that Zeeman shifts the Rydberg sub-levels [114]. The Earth magnetic field is compensated with a magnet down to the precision of $\sim$0.1 Gauss, which is taken to be the maximum magnetic field. The coupling beam is intensity-modulated at a frequency of 11 kHz using an acoustic-optical modulator, so that the signal from the detector can be demodulated in a lock-in amplifier to increase the signal to noise ratio.

6.5 Results

6.5.1 The AT splitting and the deflection measurements

The experiment firstly examines the results when the AT splitting is resolvable. Figure 6.3 (a-c) shows the experimental data and the numerical results for AT splitting corresponding to the deflection measurements. The AT splitting is asymmetric because the MW E-field was detuned by ~ 0.3 MHz from resonance for these measurements. The top panel shows the typical AT splitting in the presence of a MW E-field measured using the absorptive signal. As discussed in Chapter 2, the absolute MW E-field is calculated using the AT splitting. The observation of the AT splitting validates the MW E-field measurements using the atomic prism. The results also calibrate the MW
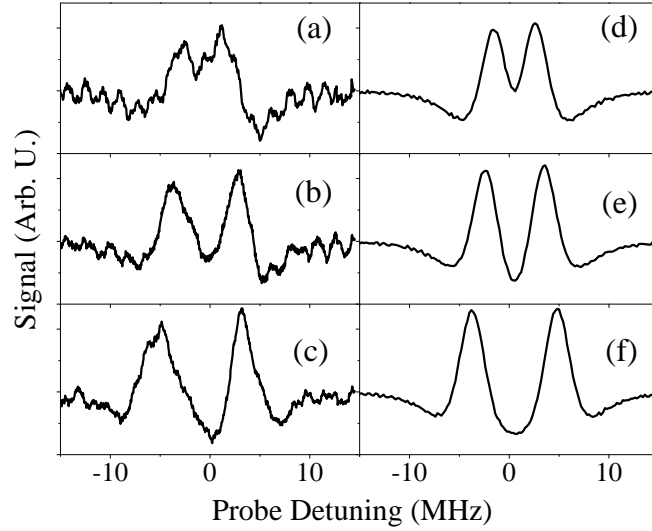
Figure 6.4: The slope change, or first derivative of the displacement signal near resonance. The experimental conditions are the same as shown in Fig. 6.3. The left panel (a), (b), (c) is the first derivative of the experimental traces of (d), (e), (f) in Fig. 6.3, respectively. The right panel (d), (e), (f) is the numerical simulation of (a), (b), (c) respectively. The zero point of the frequency axis is the resonance point of the 4-level EIT system.

E-field to the level of the variation in the measured AT splitting and uncertainty in μ_{MW}.

According to equation 6.4 in section 6.3, the deflection of the probe beam, $\Delta\mathrm{x}$, is frequency-dependent and approximately proportional to the real part of the index change around resonance. Fig. 6.3 $(\mathrm{d-f})$ shows signals from the quadrant detector measuring the displacement of the probe laser as the laser scans across the resonance frequency. When increasing the MW E-field amplitude, the dispersive signal splits at the resonant frequency as expected. A full numerical calculation of the 4 level EIT system is used to generate the theoretical curves. Our experimental data is in good agreement with the numerical simulations. Specifically, the absorptive signal with AT splitting is accurately simulated at different MW E-field amplitudes, as shown in the top panel of Fig. 6.3. The displacement signals also matches the numerical calculation, as shown in the bottom panel of Fig. 6.3.

6.5.2 The slope of the deflection measurements

When the AT splitting is not resolvable at low MW E-fields, the measurement requires analyzing the slope change of the displacement to determine the MW E-field amplitude. The change of the dispersive slope representing the change in the index of refraction induced by MW E-field is quite sensitive, especially when the MW E-field amplitude is low. Figure 6.4 shows the slope of the dispersive signal as a function of the probe laser frequency near resonance. The results are obtained by taking the first derivative of the displacement measured when scanning the probe laser frequency.

Taking the derivative of the displacement signal reveals the MW E-field amplitude values more clearly because the features of the measured dispersive signals are difficult to directly observe in the displacement signal as shown in Fig. 6.3. The left panel (a-c) is the experimental data while the right panel (d-f) is the simulation. The experimental results agree with the numerical simulation quite well as expected from Fig. 6.3.

The slope, $d\theta(\omega_p)/d\omega_p$, is close to that of 3-level Rydberg EIT when the MW E-field is weak. Therefore, the AT splitting cannot directly be resolved in the absorptive EIT signal. The 3-level EIT dispersive signal for the experimental conditions discussed in Section III, corresponds to a change of the index of refraction at the level of $dn(\omega_p)/d\omega_p \approx 7.67 \times 10^{-7}$ MHz^{-1}. The index of refraction can be translated to $d\theta(\omega_p)/d\omega_p \approx 0.2$ μrad MHz^{-1} , corresponding to a displacement change on the detector of 11 μm. The MW E-field measurement performed with the minimum detectable MW E-field induced change in the dispersive signal of 11 kHz AT splitting, corresponds to a displacement of ~ 0.024 μm, or a MW E-field amplitude of ~ 8.25 μV/cm. The sensitivity of MW E-field measurement is estimated as ~ 46.5 μVcm^{-1}Hz$^{-1/2}$. The sensitivity and the minimum detectable MW E-field are comparable to our previous experiment [38]. The wavelength resolution is R = $\lambda/\delta\lambda \approx 3.2 \times 10^{10}$.

The resolution here is lower than the predicted value given in Ref. [104], R = $\lambda/\delta\lambda \approx 10^{12}$, because the deflection angle for a typical ground state Λ-type EIT is much larger than the 4-level ladder EIT-like system that includes Rydberg states. The ground state Λ-type EIT system has a much longer coherence time.

The maximum coherence time of the 4-level EIT-like system using Rydberg states is determined by the lifetime of the Rydberg states, $\sim 30 \ \mu$s here. The coherence time for a Λ-type EIT that uses ground states is determined by the spin relaxation time, which is on the order of seconds. The diffraction limit and the spectral width of the EIT signal are also important limitations when measuring effects that depend on a small deflection. The key factor that makes the measurement of lower MW E-field amplitudes using Rydberg atoms difficult, is the residual Doppler broadening, $\sim 2 - 3$ MHz under the conditions of this work. In contrast, for the ground state Λ-type EIT system, the wavelengths of the probe and the coupling lasers are matched, resulting in very small residual Doppler broadening. The residual Doppler broadening decreases the slope of the dispersive signal in the presence of a MW E-field. The Doppler broadening effect can be reduced in future experiments by using alternative multi-photon schemes for readout.

6.5.3   Comparison of the experimental and calculated results

The experimental results and numerical simulation of the slope change with respect to the amplitude of the MW E-field are shown in Fig. 6.5. In the numerical simulation, an intensity change of the probe laser is up to 10% because of the rough surface of the prism-shaped vapor cell. The surface of the vapor cell is not perfectly flat, as the pyrex was fused at very high temperature during construction at our glass shop. The surface of the vapor cell can change the intensity of the probe laser when it moves during the measurement. An optically flat surface can be obtained
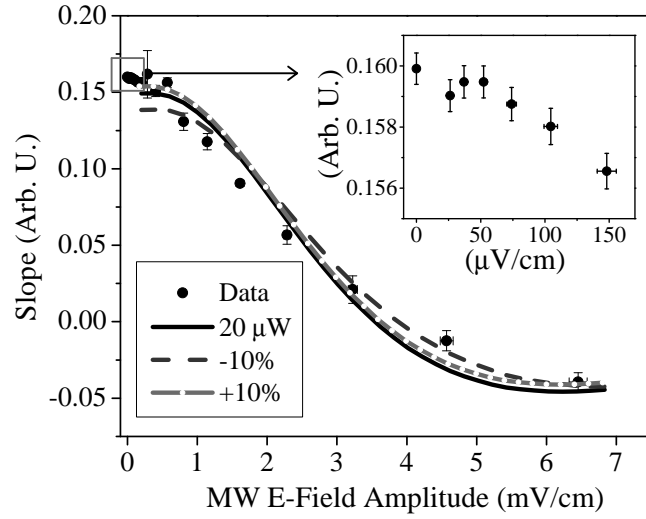
Figure 6.5: (color online) The slope at resonance versus MW E-field. A probe power uncertainty is up to $\pm 10\%$ due to the rough surface of the prism vapor cell. The unit of the slope is arbitrary unit considering its value depends on the overall amplitude of the processed signal, which can be normalized to the amplitude of the EIT signal with no MW E-field present. The error bar along the x-axis is given by considering the uncertainty of the MW E-field amplitude in the MW E-field measurement. The error bar along the y-axis is derived from the standard deviation of the raw data.

by improving the vapor cell manufacturing process, for example, by using anodic bonding to construct the prism shaped vapor cell [69]. The experimental results are in agreement with the numerical simulations for large MW E-field amplitudes, but the deviation grows as the MW E-field decreases. One reason for the deviation is that the dephasing rates are difficult to accurately estimate considering the spectral resolution of the experiment. The dephasing rates have a large influence on the index of refraction change at low MW E-field amplitude because these rates are approaching the MW E-field Rabi frequencies. Uncertainties in these factors are due to effects such as polarization or intensity drift of lasers, stray electric and magnetic fields and temperature fluctuations of the environment. A more sensitive MW E-field measurement requires a design to reduce the residual Doppler effect and the environmental noise. By reducing the residual Doppler effect, e.g. down to a few kHz determined only by the lifetime of Rydberg states, the resolution of the angular dispersion can be as large as $R = \lambda/\delta\lambda \approx 10^{12}$ [104]. Thus, the sensitivity can be improved by up to two orders of magnitude. An experimental configuration reducing environmental noise, for example, a double vapor cell setup as described in Ref. [115] or a Sagnac interferometer configuration similar to Ref. [116], can also increase the sensitivity of the MW E-field measurement.

6.6   Outlook

A higher sensitivity of MW E-field sensor can be used to study physics which is hard to observe using conventional methods or even lead to discovery of new physics

[87, 77]. Achieving a sensitivity several orders of magnitude greater than the current limit, it is also possible to quantify and study the dephasing rates to improve the sensor. For example, superradiance between Rydberg states, which is usually studied with large Rydberg population [111], can be observed. With higher sensitivity, the interactions between Rydberg atoms can cause a dephasing rate that limits the MW E-field measurement. Thus, these interactions can be precisely quantified despite of their small values [117]. These measurements can be useful for quantum information applications in vapor cells [118, 119].

The experimental setup described here also has potential for several applications. By folding the alignment of the probe beam, the experimental setup can potentially be integrated into a compact MW electrometer. MW E-field spatial distributions can be mapped using this setup by detecting the gradient of the index of refraction induced by MW E-fields. In addition, it is possible to study non-linear optical phenomena in the MW regime by manipulating the dispersive properties of the 4-level EIT-like system with MW E-fields. The ability to deflect laser beams using MW E-fields can also be developed as a refractive index waveguide [120], or for optical cloaking [121]. By controlling the direction of the probe laser propagation in the presence of a MW E-field, all optical switching [122] can be accomplished. Similar to the scheme in Ref. [123], a prism-shaped vapor cell can be implemented as a device for broadband optical steering with MW E-field control. Modern MW technology enables encoding complex signals in the MW E-field to control the laser beam pointing at high speed. Thus, the experimental setup can potentially be used for information transport and

communications.

6.7 Conclusion

In summary, the chapter has experimentally demonstrated MW E-field measurements using an atomic prism in a vapor cell at room temperature by measuring the probe beam deflection. At a transition frequency of 5.047 GHz, the minimum MW E-field amplitude obtained in this work was 8.25 μVcm^{-1}, with a sensitivity of ~ 46.5 μVcm^{-1}Hz$^{-1/2}$, which is comparable to our previous efforts based upon directly measuring the absorptive part of the EIT readout signal [38]. The experimental data agrees well with the full calculation of the 4-level EIT system. The measurement is limited by the spectral resolution of the experimental setup, the dephasing rates, noise such as stray electric and magnetic fields, and the surface quality of the vapor cell. The sensitivity of the measurement can be increased by improving the manufacturing process of the vapor cell, and adopting a multi-photon readout which can reduce the residual Doppler effect. The method holds promise for many applications, because of its ability to measure the index of refraction change induced by MW E-fields and the control of the propagation direction of the probe laser beam using a MW E-field. In addition, it is satisfying to see that a dispersive signal approach to Rydberg atom electrometry behaves as expected.

Chapter 7

Microwave Electric Field Measurements Using Mach-Zehnder Interferometer with Cesium Rydberg Atoms in Vapor Cells

7.1   Introduction

This chapter introduces a new method to perform Rydberg atom-based MW E-field measurements. The method uses a Mach-Zehnder interferometer (MZI) along with a homodyne detection technique [124, 125, 105, 126, 106, 127]. With the MZI, the measurement is performed by observing phase difference between a probe signal and a local oscillator (LO). The noise of the probe laser can be canceled by the subtraction of the homodyne detection and the EIT signal is enhanced by the strong LO. The MW E-field measurement has reached a high sensitivity, $\sim 3 - 5\mu\mathrm{Vcm}^{-1}\mathrm{Hz}^{-1/2}$, which is one order of magnitude higher than the previous result [38].

7.2   Motivation

In previous chapters, Rydberg atoms have been introduced to measure the amplitude of MW E-fields. The Rydberg atom-based MW E-field measurement is promising for performing traceable MW E-field measurements with a higher sensitivity than that of the conventional antenna standard. The high sensitivity of the MW E-field measurement is a result of the huge transition dipole moment between Rydberg states [51]. The huge transition dipole moment makes Rydberg atoms extremely

sensitive to MW E-fields.

One of the limiting factors for the Rydberg atom-based approach is the noise of the probe laser. The probe laser always has small drifts in terms of power and polarization. The noise of the probe laser reduces the signal-to-noise ratio (SNR) of the Rydberg EIT window. Thus, the sensitivity of the MW E-field sensing is decreased. An optical interferometer is one of the options to eliminate the noise of the probe laser. The interferometer detects the nonlinear phase shift instead of directly measuring transmitted probe power. A lot of experiments with atoms [128, 129], photons [130, 125, 105, 131, 132], and electrons [133] show that interferometers have the ability to perform physical measurements at a high sensitivity and has the potential to reach the shot noise limit.

The increased sensitivity gives the opportunity to quantitatively study the factors determining the shot noise limit. The factors include transit time broadening, collision broadening and lifetime of Rydberg atoms. The experiment described in this chapter quantitatively studies how these factors determine the shot noise limit for atom-based MW electrometry.

7.3   Experiment

7.3.1   Mach-Zehnder interferometer

A MZI is applied in this chapter to reduce the noise of the probe laser. Fig. 7.1 shows the experimental setup using the MZI along with homodyne detection. The probe laser, 852 nm, excites the atoms from the ground state to an intermediate state,
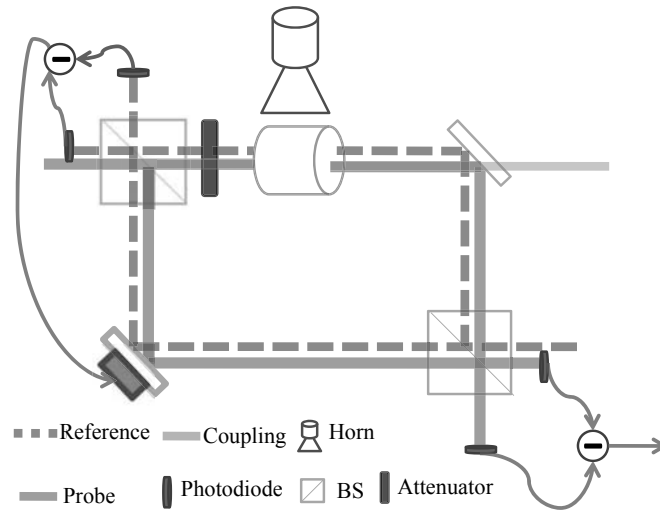
Figure 7.1: Diagram of the setup for the experiment. The probe laser (red line) is split into two branches by a $50 - 50$ non-polarizing beamsplitter (NBS). One goes into the vapor cell overlapped with the coupling laser (blue line). The other goes to a mirror with a piezoelectric transducer(PZT) attached. These two beams overlap in the other NBS and are split into two branches with different phases. The output probe laser signals are captured by a homodyne detection scheme. The reference laser enters the MZI from the output side and is overlapped with the probe laser in the MZI. The output of the reference laser is detected by a differential photodiode and is sent to a PID loop to stabilize the MZI.

i.e., $6S_{1/2}(F = 4) \rightarrow 6P_{3/2}(F' = 5)$. The probe laser beam passes through the MZI

to eliminate the noise. A $50-50$ non-polarizing beamsplitter cube (NBS) splits the

probe beam into two arms. One arm is the probe arm and the other arm is the LO.

The probe arm passes through a neutral density (ND) attenuator and then a 4-cm

long cylindrical cesium (Cs) vapor cell; the probe arm is reflected by a hot mirror

and goes to a second NBS. The LO hits a mirror where a piezo-electric transducer

(PZT) is attached and then passes the second NBS. The probe arm and the LO are

merged at the second NBS and interfere with each other. The two arms maintain

the same polarization to obtain maximum interference. The coupling laser, 509 nm,

passes through the hot mirror and overlaps with the probe arm to excite the atoms

into a Rydberg state from the intermediate state, i.e., $6P_{3/2}(F' = 5) \rightarrow 52D_{5/2}$. A

horn antenna radiates a MW E-field at a frequency of 5.047 GHz. The MW E-field is

resonant with the $52D_{5/2} \leftrightarrow 53P_{3/2}$ transition.

The homodyne detection system is implemented on the output side of the second

NBS. The two output channels of the MZI are captured by a differential photodiode.

The intensity of the LO is much higher than the probe arm. The coupling laser is

intensity-modulated using an acoustic-optical modulator (AOM). Then, the probe

signal captured by the homodyne detector is demodulated by a lock-in amplifier and

recorded by an oscilloscope. A reference laser, 795 nm, is used to lock the phase of

the interferometer. The frequency of the reference laser is far way from any transition

of Cs atoms. This reference laser enters the MZI from the output side of the probe

laser and overlapped with the probe beam in the MZI. The output of the reference
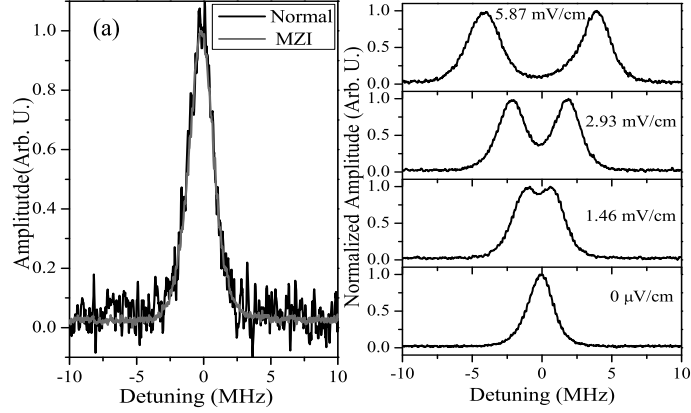
Figure 7.2: (a). Single trace of Rydberg EIT with and without MZI. The data is taken using the same Rabi frequencies for both probe and coupling laser. (b). A single trace of Autler-Townes Splitting using MZI. The scan period is 1 sec and the integration time is 1 ms.

laser is detected by a differential photodiode. The signal of the photodiode goes to a PID loop to stabilize the MZI through the PZT. The MZI is stabilized where the EIT signal is maximum.

7.3.2 Oven

As a part of the experiment, an oven is built to control the temperature of the vapor cell. The size of the oven is large enough to fit the vapor cell and the heater inside. To maintain the stability of the MZI when heating the vapor cell, the oven is made of TPX. There are several reasons to build the oven like this. Firstly, the dielectric constant of TPX is low, $\epsilon = 2.1$. The dielectric constant of a material determines the reflection and absorption to MW E-fields. Specifically, as discussed in Chapter 5, the lower ϵ will cause less absorption and reflection to MW E-fields. The

dielectric constant of TPX is closer to that of the air compared to other materials such as pyrex and quartz. The reflection and absorption of the MW E-field can be negligible. Thus, this oven is considered to be transparent to the MW E-field. Secondly, an oven is a good isolation for the air flow or the change in index of refraction of the air caused by the heater. The uniform temperature in the oven minimized the disturbance to the MZI when heating the vapor cell. Thirdly, the TPX has a high soften and melting point, $\sim$ 240 ºC. The high soften and melting point gives the experiment enough temperature range. The highest temperature in the MW E-field measurement is $\sim$ 80 ºC.

7.3.3 The signal to noise ratio of EIT

Fig.7.2(a) shows the comparison of the EIT windows with and without the MZI. The Rabi frequencies of the probe and the coupling laser are set to be the same in both cases. As shown in Fig. 7.2(a), the SNR of EIT is improved by at least a factor of 20 with the MZI and homodyne detection. Fig.7.2(b) shows the Autler-Townes (AT) Splitting at different intensities of the MW E-field. The results are obtained from a single trace when scanning the frequency of the probe laser. The scanning period is 1 s and the integration time is 1 ms. When the MW E-field is at the mV/cm level, the AT splitting can be resolved and the amplitude of the MW E-field can be determined directly by observing a single trace of the AT splitting. When the MW E-field is lower than the mV/cm level, e.g. μV/cm level, the MW E-field amplitude is determined by the transmission of the probe beam relative to the EIT height.
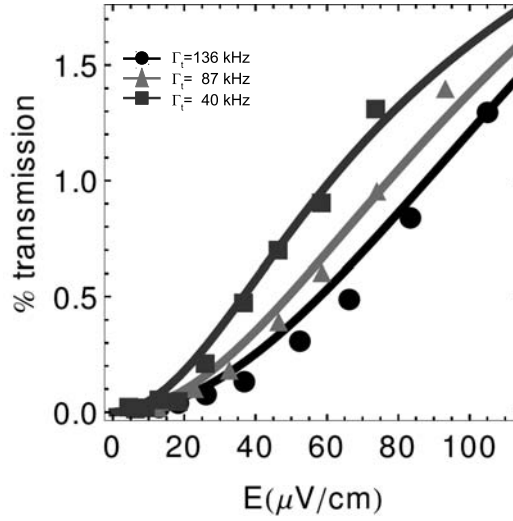
Figure 7.3: The results of percentage increased in transmission versus ME electric field for three different transit time broadening. The experiment uses 3 beam sizes, 0.32 mm, 0.50 mm and 1.1 mm, corresponding to transit time broadening 40 kHz (black), 87 kHz (red) and 136 kHz (blue). The dots are the measurement data and the lines are the calculation using density matrix method.

The high SNR enables the detection using lower power for the probe and coupling laser beams compared to the case without MZI. Thus, the power broadening can be reduced in the experimental setup. For example, the full-width-half-maximum (FWHM) of Rydberg EIT window is 1.6 MHz at room temperature. The FWHW of the EIT window is much lower than that of previous setups [38]. With the Rydberg EIT with high SNR, the experimental setup is able to detect the dephasing effects for the MW E-field measurement, e.g., transit time broadening and collision broadening.

7.4 Results

7.4.1 The trasit time broadening

One important dephasing factor for the MW E-field measurement is transit time broadening. For the atoms in vapor cells, the laser is a pulse of light whose width is determined by the time for atoms to pass through. Thus, the spectroscopic signals are broadened. The transit time broadening is determined by the size of the laser beam and the velocity of the atom, i.e.,

$$\Delta\nu = \sqrt{2}v/d, \tag{7.1}$$

where $\Delta\nu$ is the transit time broadening rate, v is the velocity of the atoms, and d is the diameter of the interaction regime, that is, the diameter of the probe beam in the experiment.

For the MW E-field measurement, Fig.7.3 shows the transmission difference with different beam sizes at room temperature. The radii of the beam are 1.1 mm, 0.5 mm,

and 0.32 mm, which give transit time broadening rates of 40 kHz, 87 kHz, and 136 kHz, respectively. The signal is calibrated as the percentage of EIT height without the presence of the MW E-field. As the the transit time broadening rate decreases, the percentage of transmission increases. This means the sensitivity is higher when the beamsize is larger. The experimental results are consistent with numerical simulation results as shown in Fig 7.3.

7.4.2 The collisional broadening

Collision broadening effects of the atoms in the vapor cell is also important. The collision broadening rate is defined as,

$$\Gamma_{col} = \sigma v \rho, \tag{7.2}$$

where Γ_{col} is the collision broadening rate, σ is the cross section, and ρ is the density of atoms. The density of the Cs vapor changes at different temperatures because the vapor pressure of Cs in the vapor cell changes [134]. In the 22 ℃ to 80 ℃ regime, the average velocity of atoms changes little while the atomic density varies at different temperature.

The cross section can be evaluated by observing the EIT FWHM at different temperatures shown in Fig. 7.4 (a). In Fig. 7.4 (b), the results are converted to density of atoms versus FWHM. A polynomial function is applied to fit the FWHM with the change of the atom density. The results show that the FWHM changes linearly with the change of the atom density, which validates Eq. 7.2. Thus, the cross section for collisions can be derived as $\sigma = 1.2 \times 10^{-11}$ cm^2, which is consistent
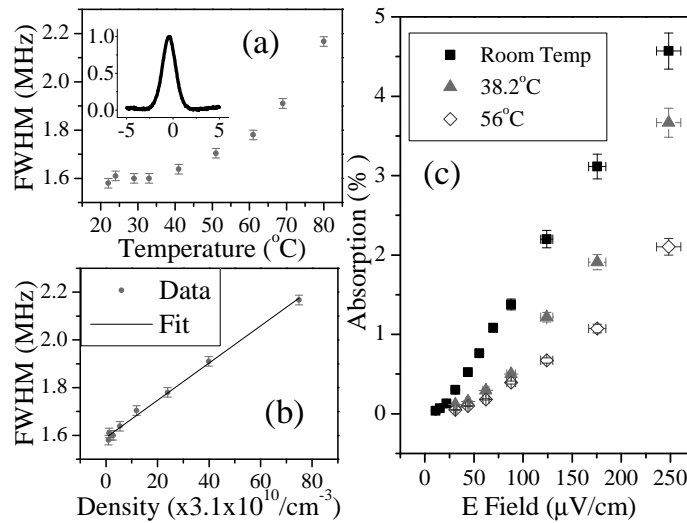
Figure 7.4: (a). The FWHM of EIT at different temperatures. the inset is a typical EIT at room temperature. (b). The density of the atoms in the vapor cell versus the FWHM of EIT, and the linear fit. The density is calculated using the temperature in (a). $3.1 \times 10^{10}/\text{cm}^{-3}$ is the density at room temperature. (c). The absorptive behavior of the MW E-field at different temperatures. Collision rate is larger at higher temperature. This give the lower absorption when MW electric field is applied.

with reported theoretical work [51]. The experimental results give the collision rate, $\sim 8.2 \, \text{MHz} \cdot \text{mTorr}^{-1}$. The ground-Rydberg atom collision rate, $\sim 5 \, \text{MHz} \cdot \text{mTorr}^{-1}$, is the dominant one. In the process of MW E-field measurements, the population of Rydberg atoms is low, $\sim 0.01\%$ of the ground state atom density. The average distance between the Rydberg atoms is large, $> 100 \, \mu$m. Therefore, the Rydberg-Rydberg atom collision rate is much smaller, $< 1 \, \text{kHz}$. The dephasing involving the intermediate state, $6\text{P}_{3/2}$, is dominated by the spontaneous emission $\sim 5.2 \, \text{MHz}$. Thus, the collisions involving the $6\text{P}_{3/2}$ state, $\sim \text{kHz}$, are negligible. The cross section for ground-ground state atom collisions is much smaller than the Rydberg-ground state collision at the temperatures that are considered here.

Fig. 7.4 (c) shows the absorptive behavior of the MW E-field at different temperatures, that is, at different collision broadening rates. When the collision broadening rate increases, the spectral absorption of the probe beam induced by the MW E-field gets smaller, so the sensitivity of the measurement decreases. When the density of atoms is 10 times (usually round 56 ºC) the density at room temperature, $3.1 \times 10^{10}/\text{cm}^{-3}$, the collision broadening effect dominates the MW E-field measurement.

7.4.3 Power broadening

Even with the same transit time broadening rate and collision broadening rate, the power of both lasers affects the sensitivity of the MW electric field measurement. Fig. 7.5 shows the effect of changing the power of the probe laser and the coupling laser. When the MW E-field amplitude is several hundred μV/cm, the spectrum can

vary from absorption to transmission as the laser power increases. The transmission happens when one increases the power of both the probe and coupling laser. Because the MW E-field measurement is not in the weak probe regime, the Rydberg EIT window can easily be broadened by the probe or the coupling power. Thus, when a small MW E-field is coupled between Rydberg states, the EIT window gets larger. The power broadened case is the same as observed in Ref [38].
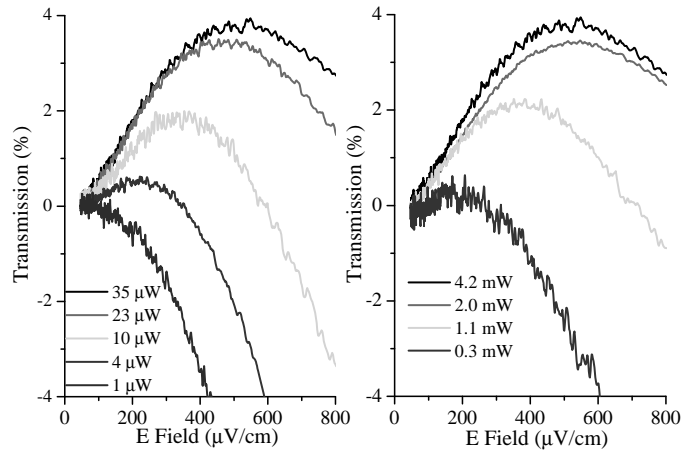
Figure 7.5: Left: the absorptive behavior with MW electric field at different powers of the probe; the power of the coupling laser is 2 mW. Right: the absorptive behavior with MW electric field at different powers of the coupling laser; the power of the probe laser is 35 μW

Under the broadened EIT condition [38], the sensitivity is limited, and the minimum detectable field is larger. This is due to the fact that the population of the intermediate state and Rydberg state are larger than those of lower laser powers. The large Rydberg population increases the dephasing rate. For example, the increased population of the intermediate state and Rydberg states due to the higher laser powers

can cause more collisions between atoms. Moreover, the interactions between the atoms and vapor cell walls are also increased. Stronger laser powers can generate more ionized atoms. The ionized atoms in the vapor cell create inhomogeneous electric fields. More work on Rydberg surface interactions is needed to quantify the dephasing rates due to surface effects. Suitable power of lasers need to be selected to obtain the best sensitivity for the MW E-field measurement.

7.4.4 Measurements at different modulation frequencies

As described in the Section 7.3, the coupling laser intensity is modulated using an AOM to increase the SNR in the data acquisition process. However, the modulation changes the atomic spectrum at different modulation frequencies [135]. To clearly show the observation, we investigate the spectrum at different modulation frequencies with the presence of MW E-fields. The results are shown in Fig. 7.6. In the left side of Fig. 7.6, the MW frequency is scanned while the probe and coupling laser are at resonance. The spectrum changes from transmission to absorption when increasing the modulation frequency. On the right side of Fig. 7.6, the power of the MW is scanned when the probe, coupling laser and MW are all at resonance. The experimental results show the same behavior as that of the left side in Fig.7.6.

At a low modulation frequency, a period of modulation is longer than the lifetime of Rydberg atoms. The Rydberg atoms decay to the ground state before the next cycle of modulation. While at a higher modulation frequency, at least one modulation cycle happens before the Rydberg atom decays to the ground state. As a result,

more power of the probe laser is absorbed at higher modulation frequencies. The effective interaction time between Rydberg atoms and the MW E-field is also longer at higher modulation frequencies. In this sense, the sensitivity of the MW E-field measurement is better at higher modulation frequencies. Both the modulation period and the lifetime of a Rydberg state is in the μs scale. For the 4-level EIT to reach equilibrium, or steady state condition, the time is in the ns scale. Therefore, the discussion in this section is in steady state condition of the 4-level EIT system.
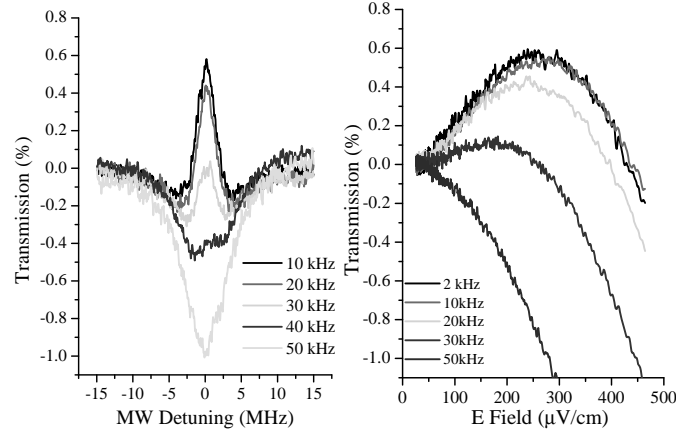

Figure 7.6: Left, the scan of MW frequency versus transmission at different modulation frequency. Right, spectrum using different modulation frequency when the MW is at resonance.

7.4.5 Discussions

The sensitivity at the shot noise limit can be calculated as [48]

$$E_{min} = \frac{h}{\mu\sqrt{T_2 T N}}, \tag{7.3}$$

131

where h is the Planck constant, μ is the transition dipole moment, T is the measurement time, and N is the number of atoms in the interacting area. T_2 is the dephasing time. T_2 is determined by the transit time broadening, Γ_t, the collisional broadening, Γ_{col}, and the lifetime of the Rydberg state, Γ,

$$1/T_2 = \sqrt{\Gamma_t^2 + \Gamma_{col}^2 + \Gamma^2}. \tag{7.4}$$

The minimum value obtained in experiment is $\Gamma_t = 40$ kHz, $\Gamma_{col} = 40$ kHz and $\Gamma = 30$ kHz. When the measurement time $T = 1$ sec and the transition dipole moment $\mu = 1745\ ea_0$, the calculated sensitivity determined by shot noise limit is approximately ~ 500 pVcm^{-1}Hz$^{-1/2}$. In experiment, the MW E-field measurement has additional dephasing effects, e.g., transit time broadening and collision broadening effects. These effects are at the same noise level as determined by the Rydberg lifetime. The achieved sensitivity, $3 - 5\ \mu$Vcm^{-1}Hz$^{-1/2}$, is an order higher than our prior best sensitivity [38].

The sensitivity to the MW E-field measurement is also limited by the residual Doppler effect. The residual Doppler effect is caused by the wavelength mismatch between the probe and and coupling lasers. The current FWHM of the Rydberg EIT is ~ 1.6 MHz. The residual doppler effect contributes the most to the ~ 1.6 MHz width. The width of the Rydberg EIT can be significantly reduced to the regime of $\sim$ kHz by using multi-photon readout scheme in future experiments.

Despite their small rates in the current experimental setup, some other effects may also be factors limiting the sensitivity of the MW E-field measurement. For example, superradiance between Rydberg states. The transition wavelength between

Rydberg states is usually much longer than that of ground states transitions. So the superradiance can be important. As discussed in Chapter 6, the maximum superradiance rate can be as large as $\Gamma_{\text{Sup}} \approx 2\pi \times 700$ kHz. For Rydberg atoms in a vapor cell at room temperature, the initial phases of the atomic oscillators are not correlated and change randomly, so the superradance is suppressed and not observable using current experimental setup. The transition between Rydberg states is long compared to the interaction sized of atomic vapor. Thus, the superradiance between Rydberg states can potentially contribute to decay and dephasing processes.

The reasons preventing us from reaching quantum shot noise limit can also be in the experimental setup itself. The detection bandwidth is low, 50 kHz. 50 MHz is a typical modulation frequency for MZI detection methods to reach Heisenberg limit [136]. The amplitude-modulated (AM) signal of the couping laser creates residual amplitude noise. The residual amplitude noise leads to dephasing and drift that dramatically reduce the sensitivity. By applying an active feedback control system as described in Ref [137], it is possible to reduce the noise of the coupling laser down to the shot noise limit. The noise from the MZI degrades the sensitivity. The noise could be in the phase stabilization of MZI, the amplitude fluctuation of the interferometric arms, the imperfection of the photodetection, or the phase diffusion of the MZI. As proposed in Ref [136], the MZI can be designed as a nearly optimal interferometer by controlling the phase diffusion. The interaction of the Rydberg atoms with vapor cell walls causes dephasing, too. More work on vapor cell construction and material selection needs to be done to minimize the Rydberg atom-surface interactions. Moreover, the residual

magnetic field of the earth is another factor that limits the sensitivity. A magnet is used to compensate the earth magnetic field down to 0.1 Gauss. The vapor cell has to be put in free space such that the MW E-field gets least reflection or absorption. So it is hard to shield the magnetic field completely because the shield materials are usually made of metal. The sensitivity of the MW E-field measurement using the MZI can be essentially improved by solving these problems.

7.5 Conclusion

In summary, the experiment applies a homodyne detection technique using a MZI to achieve a new sensitivity limit for the measurement of MW E-fields, $\sim 3 - 5 \ \mu \mathrm{Vcm}^{-1} \mathrm{Hz}^{-1/2}$. The minimum detectable field is $\sim 1 \ \mu \mathrm{Vcm}^{-1}$. This set-up can be easily implemented to cancel the noise of the probe laser. The chapter also discusses the homogeneous dephasing effects caused by transit time broadening, collision broadening, and the lifetime of the Rydberg atoms. It is shown that these dephasing effects are the fundamental limiting factors that determine the shot noise limit. The study of these factors is important not only to MW E-field sensing, but also to quantum information science which requires to manipulating the interactions involving Rydberg atoms. A recent report shows that the optical MZI can be integrated into a chip [138] to study alkali atom spectroscopy. This can be beneficial to the MW E-field measurement towards on-chip devices without the probe noise.

Chapter 8

Discussions and outlook

8.1 A brief review on atom-based MW electrometry

This dissertation demonstrates an atom-based method to measure MW E-fields. The atom-based approach uses Rydberg atoms in thermal vapor cells via electromagnetically induced transparency (EIT). A MW E-field is coupled between two neighbouring Rydberg state, causing an AT splitting in the atomic spectrum. The amplitude of the MW E-field is proportional to the AT splitting. The atom-based method is promising to perform MW E-field measurements with a sensitivity orders of magnitude higher than the conventional MW standard. The measurement of MW E-fields links to the properties of Rydberg atoms. The properties of Rydberg atoms are determined precisely with atomic spectroscopy. Thus, the properties of Rydberg atoms lead to traceable or self-calibrated devices for MW E-fields.

Being different from the conventional dipole antennas that are made of conducting materials, the atom-based approach utilizes an atomic vapor in a dielectric container. The dielectric container is free of metal and minimally disturbs the MW E-field. This dissertation demonstrates an imaging technique to measure MW E-fields in the sub-wavelength regime, obtaining $\sim 66\,\mu$m, $\lambda/650$ spatial resolution the [39]. The near-field measurement is also presented by imaging a MW E-field near a waveguide. The method is promising to develop into portable standard devices by minimizing the setup and detection system. The accuracy of the MW E-field measurement is

about ∼1% by using a vapor cell with its size much smaller than the wavelength of the target MW E-field.

The dissertation introduced an alternative way to measure the amplitude of a MW E-field besides using AT splitting. The amplitude of a MW E-field is determined by detecting the change in the index of refraction induced by the MW E-field. The change in the index of refraction results in the deflection of the probe laser beam passing through a prism shaped vapor cell. The sensitivity of the MW E-field measurement is $\sim 46.5\,\mathrm{mV\,cm^{-1}\,Hz^{-1/2}}$ with a minimum detectable field of $\sim 8.25\,\mu\mathrm{V\,cm^{-1}}$.

The dissertation also presents the MW E-field measurement applying a Mach-Zehnder Interferometer with a homodyne detection. The sensitivity of the MW E-field measurement reaches $\sim 3\mu\mathrm{Vcm^{-1}Hz^{-1/2}}$ and the minimum detectable field is $\sim 1\mu\mathrm{Vcm^{-1}}$. The dephasing is caused by transit time broadening, collision broadening, and the lifetime of the Rydberg atoms. These dephasing effects are the fundamental limiting factors that determine the shot noise limit.

8.2   Shot noise limit for Rydberg atom electrometry

In Chapter 7, the equation 7.3 gives the minimum detectable E-field limited by the shot noise. When setting the integration time T = 1 s, the shot noise limit sensitivity is given by

$$\frac{E_{min}}{\sqrt{Hz}} = \frac{h}{\mu_{MW}\sqrt{N_{at}T_2}}.$$

(8.1)

When ignoring transit time broadening and collisions, the dephasing time T_2 is determined by radiative decay rate of the involved Rydberg state, scaling with n^3,

while the transition dipole moment scales with n^2. As a result, the sensitivity scales with n as,

$$\frac{E_{min}}{\sqrt{Hz}} \sim n^{-3.5}. \tag{8.2}$$

Take [133]Cs gas for an example, the Cs gas is in a vapor cell at room temperature. The EIT beam radius is 0.5 mm and the length of the vapor cell is 3 cm. The transition of $52D_{5/2} \rightarrow 53P_{3/2}$ at 5.047 GHz with a transition dipole moment is ~ 1749 ea$_0$. At room temperature, 25 ºC, the pressure of the Cs vapor cell is $\sim 1.5 \times 10^{-6}$ Torr, corresponding to a atomic density of $\sim 5 \times 10^{10}$cm^{-3}. About $\sim 1/400$ of the atomic density in the vapor cell participates in the EIT process. Therefore, the sensitivity is 10 pVcm^{-1}Hz$^{-1/2}$.

To pursue a sensitivity towards shot noise limit, several other effects can limit the sensitivity of the MW E-field measurement. For example, collisions and transit time broadening change the dephasing time T_2 so the sensitivity of the MW E-field measurement is degraded. The technical noises need to be overcome to reach this sensitivity. These noises are due to the noise of lasers, stray electric and magnetic fields, etc.

8.3   Outlook

The statistical error are caused by several technical noises including frequency and intensity instability of the lasers, acoustic noise from the opto-mechanics, and optical imperfections. More efforts on reducing these technical noises are needed for the MW E-field measurement. The wavelength mismatch between the probe and

coupling lasers induces a residual Doppler effect that is the main factor to broaden the EIT window. The broadened EIT window limits the sensitivity of the MW E-field measurement. To reach the shot noise limit, it is necessary to find a way to eliminate the residual Doppler effect. The background magnetic field of the earth is one of the primary source of systematic errors. Maintaining a high accuracy of the MW E-field measurement requires to improve methods to shield, compensate, and cancel the stray magnetic field in the background.

Standard antenna measurements are needed to test the Rydberg atom-based MW E-field sensing. The stable properties of Rydberg atoms facilitate calibration of the MW radiation to SI units. A comparison to a conventional standard antenna is needed to validate the Rydberg atom-based sensor as a candidate for a new generation of the MW E-field standard. As demonstrated in this dissertation, the atom-based MW E-field sensors are superior to the conventional standard antenna. Thus, it is necessary to build two Rydberg atom-based standards. The comparison between the two standards is essential to evaluate the precision of the new standard.

Besides being a candidate as a new standard for MW E-field measurement, the potential to be a portable MW E-field sensor is also attractive to both scientific research and industrial applications. The techniques for a portable atom-based sensor have already been developed for atomic clocks [63]. These techniques include micro-optics package for the laser system, mini-vapor-cell fabrication technique, magnetic field shielding, and minimizing the electric power consumption for the device. With these existing techniques, a small volume of MW E-field probe is promising to implement

using the Rydberg EIT process as discussed in this dissertation.

The Rydberg atom-based MW E-field sensor creates a choice for probes at far-infrared (FIR) frequencies. The atom-based approach can lead to self-calibrated devices for MW E-field in the FIR regime. By changing the principle quantum number of Rydberg atoms, the Rydberg EIT system is applicable to measure MW E-fields across a large frequency range, from GHz to THz. A highly sensitive THz MW sensor facilitates the applications with THz radiation such as quantum cascade laser, wireless communication with THz waves, and metamaterials in the THz-frequency range [139]. The detection of MW E-field in millimeter regime (or 100 GHz regime) has been already realized using this approach [140]. The Rydberg EIT method provides a promising approach for MW E-field detection in FIR frequencies including the millimeter wave regime and THz frequency regime.

References

[1] John Kitching, Svenja Knappe, and Elizabeth A Donley. Atomic sensors–a review. *Sensors Journal, IEEE*, 11(9):1749–1758, 2011.

[2] IK Kominis, TW Kornack, JC Allred, and MV Romalis. A subfemtotesla multichannel atomic magnetometer. *Nature*, 422(6932):596–599, 2003.

[3] Dmitry Budker and Derek F Jackson Kimball. *Optical magnetometry*. Cambridge University Press, 2013.

[4] Christo Buizert, Daniel Baggenstos, Wei Jiang, Roland Purtschert, Vasilii V Petrenko, Zheng-Tian Lu, Peter Müller, Tanner Kuhl, James Lee, Jeffrey P Severinghaus, et al. Radiometric 81kr dating identifies 120,000-year-old ice at taylor glacier, antarctica. *Proceedings of the National Academy of Sciences*, 111(19):6876–6881, 2014.

[5] Pradeep K Aggarwal, Takuya Matsumoto, Neil C Sturchio, Hung K Chang, Didier Gastmans, Luis J Araguas-Araguas, Wei Jiang, Zheng-Tian Lu, Peter Mueller, Reika Yokochi, et al. Continental degassing of 4he by surficial discharge of deep groundwater. *Nature Geoscience*, 8(1):35–39, 2015.

[6] DS Durfee, YK Shaham, and MA Kasevich. Long-term stability of an area-reversible atom-interferometer sagnac gyroscope. *Physical review letters*, 97(24):240801, 2006.

[7] Brynle Barrett, Rémy Geiger, Indranil Dutta, Matthieu Meunier, Benjamin Canuel, Alexandre Gauguet, Philippe Bouyer, and Arnaud Landragin. The sagnac effect: 20 years of development in matter-wave interferometry. *Comptes Rendus Physique*, 15(10):875–883, 2014.

[8] JJ Hudson, BE Sauer, MR Tarbutt, and EA Hinds. Measurement of the electron electric dipole moment using ybf molecules. *Physical review letters*, 89(2):023003, 2002.

[9] Neil E. Shafer-Ray. Possibility of 0-*g*-factor paramagnetic molecules for measurement of the electron's electric dipole moment. *Phys. Rev. A*, 73:034102, Mar 2006.

[10] JF Barry, DJ McCarron, EB Norrgard, MH Steinecker, and D DeMille. Magneto-optical trapping of a diatomic molecule. *Nature*, 512(7514):286–289, 2014.

[11] Peter J Mohr and Barry N Taylor. CODATA recommended values of the fundamental physical constants: 2002. *Reviews of modern physics*, 77(1):1, 2005.

[12] Peter J Mohr, Barry N Taylor, and David B Newell. CODATA recommended values of the fundamental physical constants: 2006a). *Journal of Physical and Chemical Reference Data*, 37(3):1187–1284, 2008.

[13] Peter J Mohr, Barry N Taylor, and David B Newell. CODATA recommended values of the fundamental physical constants: 2010a). *Journal of Physical and Chemical Reference Data*, 41(4):043109, 2012.

[14] Vadim S Zotev, Andrei N Matlashov, Petr L Volegov, Igor M Savukov, Michelle A Espy, John C Mosher, John J Gomez, and Robert H Kraus. Microtesla mri of the human brain combined with meg. *Journal of Magnetic Resonance*, 194(1):115–120, 2008.

[15] JianCheng Fang and Jie Qin. Advances in atomic gyroscopes: A view from inertial navigation applications. *Sensors*, 12(5):6331–6346, 2012.

[16] VA Tishchenko, VI Tokatly, and VI Luk'yanov. The beginning of the metrology of radio-frequency electromagnetic fields and the first standards of electric field strength. *Measurement Techniques*, 46(1):76–84, 2003.

[17] Motohisa Kanda and R David Orr. Generation of standard electromagnetic fields in a tem cell. 1988.

[18] Motohisa Kanda. Standard probes for electromagnetic field measurements. *Antennas and Propagation, IEEE Transactions on*, 41(10):1349–1364, 1993.

[19] Motohisa Kanda. Standard antennas for electromagnetic interference measurements and methods to calibrate them. *Electromagnetic Compatibility, IEEE Transactions on*, 36(4):261–273, 1994.

[20] VA Tishchenko, VI Tokatly, and VI Luk'yanov. Upgrading radiofrequency electromagnetic field standards. part 1. *Measurement Techniques*, 46(9):903–911, 2003.

[21] VA Tishchenko, VI Tokatly, and VI Luk'yanov. Upgrading radiofrequency electromagnetic field standards. part 2. *Measurement Techniques*, 46(9):903–911, 2003.

[22] IG Malter, OP Pavlovskii, VA Korshunov, and VL Voronov. Russian and foreign millimeter band radio measuring instruments. *Measurement Techniques*, 52(9):997, 2009.

[23] Sriram S Sriram, Stuart A Kingsley, and Joseph T Boyd. Electro-optical sensor for detecting electric fields, November 30 1993. US Patent 5,267,336.

[24] David C Paulusse, Nelson L Rowell, and Alain Michaud. Accuracy of an atomic microwave power standard. *Instrumentation and Measurement, IEEE Transactions on*, 54(2):692–695, 2005.

[25] TP Crowley, Elizabeth A Donley, and Thomas P Heavner. Quantum-based microwave power measurements: Proof-of-concept experiment. *Review of Scientific Instruments*, 75(8):2575–2580, 2004.

[26] Florian Dolde, Helmut Fedder, Marcus W Doherty, Tobias Nöbauer, Florian Rempp, G Balasubramanian, T Wolf, F Reinhard, LCL Hollenberg, F Jelezko, and J Wrachtrup. Electric-field sensing using single diamond spins. *Nature Physics*, 7(6):459–463, 2011.

[27] Victor M Acosta, Kasper Jensen, Charles Santori, Dmitry Budker, and Rymond G Beausoleil. Electromagnetically induced transparency in a diamond spin ensemble enables all-optical electromagnetic field sensing. *Physical review letters*, 110(21):213605, 2013.

[28] PP Herrmann, J Hoffnagle, N Schlumpf, VL Telegdi, and A Weis. Stark spectroscopy of forbidden two-photon transitions: a sensitive probe for the quantitative measurement of small electric fields. *Journal of Physics B: Atomic and Molecular Physics*, 19(9):1271, 1986.

[29] A Osterwalder and F Merkt. Using high Rydberg states as electric field sensors. *Physical review letters*, 82(9):1831, 1999.

[30] Marcis Auzinsh, Lalith Jayasinghe, Lance Oelke, Ruvin Ferber, and Neil Shafer-Ray. Strobe imaging of electric fields by depolarization of Rydberg states of hg. *Journal of Physics D: Applied Physics*, 34(12):1933, 2001.

[31] Ashok K Mohapatra, Mark G Bason, Björn Butscher, Kevin J Weatherill, and Charles S Adams. A giant electro-optic effect using polarizable dark states. *Nature Physics*, 4(11):890–894, 2008.

[32] P Goy, L Moi, M Gross, JM Raimond, C Fabre, and S Haroche. Rydberg-atom masers. ii. triggering by external radiation and application to millimeter-wave detectors. *Physical Review A*, 27(4):2065, 1983.

[33] H Figger, G Leuchs, R Straubinger, and H Walther. A photon detector for submillimetre wavelengths using Rydberg atoms. *Optics Communications*, 33(1):37–41, 1980.

[34] Mark George Bason, M Tanasittikosol, A Sargsyan, AK Mohapatra, D Sarkisyan, RM Potvliege, and CS Adams. Enhanced electric field sensitivity of RF-dressed Rydberg dark states. *New Journal of Physics*, 12(6):065015, 2010.

[35] M Tanasittikosol, JD Pritchard, D Maxwell, Alexandre Gauguet, KJ Weatherill, RM Potvliege, and CS Adams. Microwave dressing of Rydberg dark states. *Journal of Physics B: Atomic, Molecular and Optical Physics*, 44(18):184020, 2011.

[36] AK Mohapatra, TR Jackson, and CS Adams. Coherent optical detection of highly excited Rydberg states using electromagnetically induced transparency. *Physical Review Letters*, 98(11):113003, 2007.

[37] JA Sedlacek, A Schwettmann, Harald Kübler, and JP Shaffer. Atom-based vector microwave electrometry using rubidium Rydberg atoms in a vapor cell. *Physical Review Letters*, 111(6):063001, 2013.

[38] Jonathon A Sedlacek, Arne Schwettmann, Harald Kübler, Robert Löw, Tilman Pfau, and James P Shaffer. Microwave electrometry with Rydberg atoms in a vapour cell using bright atomic resonances. *Nature Physics*, 8(11):819–824, 2012.

[39] HQ Fan, S Kumar, R Daschner, H Kübler, and JP Shaffer. Subwavelength microwave electric-field imaging using Rydberg atoms inside atomic vapor cells. *Optics Letters*, 39(10):3030–3033, 2014.

[40] Christopher L Holloway, Joshua A Gordon, Andrew Schwarzkopf, David A Anderson, Stephanie A Miller, Nithiwadee Thaicharoen, and Georg Raithel. Sub-wavelength imaging and field mapping via electromagnetically induced transparency and Autler-Townes splitting in Rydberg atoms. *Applied Physics Letters*, 104(24):244102, 2014.

[41] Jonathon A. Sedlacek, Arne Schwettmann, Harald Kübler, Robert Löw, Tilman Pfau, and James P. Shaffer. Microwave electrometry with Rydberg atoms in a vapour cell using bright atomic resonances. *Nature Physics*, 8(11):819–824, Nov 2012.

[42] SE Harris, JE Field, and A Imamoğlu. Nonlinear optical processes using electromagnetically induced transparency. *Physical Review Letters*, 64(10):1107, 1990.

[43] J Vanier. Atomic clocks based on coherent population trapping: a review. *Applied Physics B*, 81(4):421–442, 2005.

[44] Yazhou Zhao, Steve Tanner, Arnaud Casagrande, Christoph Affolderbach, Luc Schneller, Gaetano Mileti, and P-A Farine. CPT cesium-cell atomic clock operation with a 12-mW frequency synthesizer ASIC. *Instrumentation and Measurement, IEEE Transactions on*, 64(1):263–270, 2015.

[45] J Kitching, S Knappe, L Liew, J Moreland, HG Robinson, P Schwindt, V Shah, V Gerginov, and L Hollberg. Chip-scale atomic clocks at NIST. In *NCSL International Workshop and Symposium*, 2005.

[46] Michael Fleischhauer, Atac Imamoglu, and Jonathan P Marangos. Electromagnetically induced transparency: Optics in coherent media. *Reviews of Modern Physics*, 77(2):633, 2005.

[47] II Beterov, II Ryabtsev, DB Tretyakov, and VM Entin. Quasiclassical calculations of blackbody-radiation-induced depopulation rates and effective lifetimes of Rydberg n S, n P, and n D alkali-metal atoms with $n <= 80$. *Physical Review A*, 79(5):052504, 2009.

[48] Haoquan Fan, Santosh Kumar, Jonathon Sedlacek, Harald Kübler, Shaya Karimkashi, and James P Shaffer. Atom based rf electric field sensing. *Journal of Physics B: Atomic, Molecular and Optical Physics*, 48(20):202001, 2015.

[49] Mark Sheard Child. *Molecular collision theory*. Courier Corporation, 1996.

[50] Rainer Salomaa and Stig Stenholm. Two-photon spectroscopy. ii. effects of residual doppler broadening. *Journal of Physics B: Atomic and Molecular Physics*, 9(8):1221, 1976.

[51] Thomas F Gallagher. *Rydberg atoms*, volume 3. Cambridge University Press, 2005.

[52] MD Lukin, M Fleischhauer, R Cote, LM Duan, D Jaksch, JI Cirac, and P Zoller. Dipole blockade and quantum information processing in mesoscopic atomic ensembles. *Physical Review Letters*, 87(3):037901, 2001.

[53] Mark Saffman, TG Walker, and Klaus Mølmer. Quantum information with rydberg atoms. *Reviews of Modern Physics*, 82(3):2313, 2010.

[54] Donald Booth, ST Rittenhouse, Jin Yang, HR Sadeghpour, and JP Shaffer. Production of trilobite rydberg molecule dimers with kilo-debye permanent electric dipole moments. *Science*, 348(6230):99–102, 2015.

[55] Daniel A Steck. *Cesium D line data revision 2.1.4*. 2010.

[56] C-J Lorenzen and K Niemax. Precise quantum defects of ns, np and nd levels in Cs i. *Zeitschrift für Physik A Atoms and Nuclei*, 315(2):127–133, 1984.

[57] Michel Poirier. Autoionization of rydberg states with large angular momentum: Application to alkaline-earth atoms. *Physical Review A*, 38(7):3484, 1988.

[58] Christopher J Foot. *Atomic physics*. OUP Oxford, 2004.

[59] Daniel A. Steck. *Cesium D Line Data, available online at http://steck.us/alkalidata (revision 2.1.4, 2010)*.

[60] M Marinescu, HR Sadeghpour, and A Dalgarno. Dispersion coefficients for alkali-metal dimers. *Physical Review A*, 49(2):982, 1994.

[61] F Salvat, JM Fernández-Varea, and W Williamson. Accurate numerical solution of the radial schrödinger and dirac wave equations. *Computer physics communications*, 90(1):151–168, 1995.

[62] Bindiya Arora, MS Safronova, and Charles W Clark. Determination of electric-dipole matrix elements in k and rb from stark shift measurements. *Physical Review A*, 76(5):052516, 2007.

[63] Svenja Knappe, Vishal Shah, Peter DD Schwindt, Leo Hollberg, John Kitching, Li-Anne Liew, and John Moreland. A microfabricated atomic clock. *Applied Physics Letters*, 85(9):1460–1462, 2004.

[64] TW Kornack, RK Ghosh, and MV Romalis. Nuclear spin gyroscope based on an atomic comagnetometer. *Physical review letters*, 95(23):230801, 2005.

[65] Edgar L Wheeler. *Scientific glassblowing.* Interscience Publishers, 1958.

[66] Renate Daschner, Ralf Ritter, Harald Kübler, Norbert Frühauf, Eberhard Kurz, Robert Löw, and Tilman Pfau. Fabrication and characterization of an electrically contacted vapor cell. *Optics Letters*, 37(12):2271–2273, 2012.

[67] Douglas Sparks, Sonbol Massoud-Ansari, and Nader Najafi. Long-term evaluation of hermetically glass frit sealed silicon to pyrex wafers with feedthroughs. *Journal of micromechanics and microengineering*, 15(8):1560, 2005.

[68] S Knappe, PDD Schwindt, V Shah, L Hollberg, J Kitching, L Liew, and J Moreland. A chip-scale atomic clock based on 87 rb with improved frequency stability. *Optics express*, 13(4):1249–1253, 2005.

[69] Renate Daschner, Harald Kübler, Robert Löw, Holger Baur, Norbert Frühauf, and Tilman Pfau. Triple stack glass-to-glass anodic bonding for optogalvanic spectroscopy cells with electrical feedthroughs. *Applied Physics Letters*, 105(4):041107, 2014.

[70] G Epple, KS Kleinbach, TG Euser, NY Joly, T Pfau, P St J Russell, and R Löw. Rydberg atoms in hollow-core photonic crystal fibres. *Nature communications*, 5, 2014.

[71] Li-Anne Liew, Svenja Knappe, John Moreland, Hugh Robinson, Leo Hollberg, and John Kitching. Microfabricated alkali atom vapor cells. *Applied Physics Letters*, 84(14):2694–2696, 2004.

[72] Kristan L Corwin, Zheng-Tian Lu, Carter F Hand, Ryan J Epstein, and Carl E Wieman. Frequency-stabilized diode laser with the Zeeman shift in an atomic vapor. *Applied Optics*, 37(15):3295–3298, 1998.

[73] KR Overstreet, J Franklin, and JP Shaffer. Zeeman effect spectroscopically locked Cs diode laser system for atomic physics. *Review of scientific instruments*, 75(11):4749–4753, 2004.

[74] Eric D Black. An introduction to pound–drever–hall laser frequency stabilization. *American Journal of Physics*, 69(1):79–87, 2001.

[75] Robert V Pound. Electronic frequency stabilization of microwave oscillators. *Review of Scientific Instruments*, 17(11):490–505, 1946.

[76] RWP Drever, John L Hall, FV Kowalski, J Hough, GM Ford, AJ Munley, and H Ward. Laser phase and frequency stabilization using an optical resonator. *Applied Physics B*, 31(2):97–105, 1983.

[77] Andrew D. Ludlow, Martin M. Boyd, Jun Ye, E. Peik, and P. O. Schmidt. Optical atomic clocks. *Review of Modern Physics*, 87:637–701, 2015.

[78] John F O'Hanlon. *A user's guide to vacuum technology*. John Wiley & Sons, 2005.

[79] Davide Gatti, Riccardo Gotti, Tommaso Sala, Nicola Coluccelli, Michele Belmonte, Marco Prevedelli, Paolo Laporta, and Marco Marangoni. Wide-bandwidth pound–drever–hall locking through a single-sideband modulator. *Optics letters*, 40(22):5176–5179, 2015.

[80] Janis Alnis, Arthur Matveev, Nikolai Kolachevsky, Th Udem, and TW Hänsch. Subhertz linewidth diode lasers by stabilization to vibrationally and thermally compensated ultralow-expansion glass fabry-pérot cavities. *Physical Review A*, 77(5):053809, 2008.

[81] Changmin Lee, GZ Iwata, E Corsini, James M Higbie, S Knappe, MP Ledbetter, and D Budker. Small-sized dichroic atomic vapor laser lock. *Review of Scientific Instruments*, 82(4):043107, 2011.

[82] JC Camparo. Atomic stabilization of electromagnetic field strength using rabi resonances. *Physical review letters*, 80(2):222, 1998.

[83] T. Swan-Wood, J. G. Coffer, and J. C. Camparo. Precision measurements of absorption and refractive-index using an atomic candle. *Instrumentation and Measurement, IEEE Transactions on*, 50(5):1229–1233, 2001.

[84] John Pendry. Manipulating the near field with metamaterials. *Optics and photonics news*, 15(9):32–37, 2004.

[85] Felix von Cube, Stephan Irsen, Richard Diehl, Jens Niegemann, Kurt Busch, and Stefan Linden. From isolated metaatoms to photonic metamaterials: evolution of the plasmonic near-field. *Nano letters*, 13(2):703–708, 2013.

[86] Reuben M Bakker, Vladimir P Drachev, Hsiao-Kuan Yuan, and Vladimir M Shalaev. Near-field, broadband optical spectroscopy of metamaterials. *Physica B: Condensed Matter*, 394(2):137–140, 2007.

[87] Dmitry Budker and Michael Romalis. Optical magnetometry. *Nature Physics*, 3(4):227–234, 2007.

[88] Pascal Böhi and Philipp Treutlein. Simple microwave field imaging technique using hot atomic vapor cells. *Applied Physics Letters*, 101(18):181107, 2012.

[89] Andrew Horsley, Guan-Xiang Du, Matthieu Pellaton, Christoph Affolderbach, Gaetano Mileti, and Philipp Treutlein. Imaging of relaxation times and microwave field strength in a microfabricated vapor cell. *Physical review A*, 88(6):063407, 2013.

[90] Michael Fleischhauer, Atac Imamoglu, and Jonathan P. Marangos. Electromagnetically induced transparency: Optics in coherent media. *Reviews of Modern Physics*, 77:633–673, Jul 2005.

[91] Ashfaq S. Thanawalla, S. K. Dutta, C. P. Vlahacos, D. E. Steinhauer, B. J. Feenstra, Steven M. Anlage, F. C. Wellstood, and Robert B. Hammond. Microwave near-field imaging of electric fields in a superconducting microstrip resonator. *Applied Physics Letters*, 73:2491, 1998.

[92] SK Dutta, CP Vlahacos, DE Steinhauer, Ashfaq S Thanawalla, BJ Feenstra, FC Wellstood, Steven M Anlage, and Harvey S Newman. Imaging microwave electric fields using a near-field scanning microwave microscope. *Applied Physics Letters*, 74(1):156–158, 1999.

[93] Gouri Dhatt, Emmanuel Lefrançois, and Gilbert Touzot. *Finite element method*. John Wiley & Sons, 2012.

[94] Bibhas K Dutta and Prasanta K Mahapatra. Nonlinear optical effects in a doubly driven four-level atom. *Physica Scripta*, 75(3):345, 2007.

[95] H. Schmidt and A. Imamoglu. Giant kerr nonlinearities obtained by electromagnetically induced transparency. *Optics Letters*, 21(23):1936, 1996.

[96] M. D. Lukin, S. F. Yelin, M. Fleischhauer, and M. O. Scully. Quantum interference effects induced by interacting dark resonances. *Physical Review A*, 60(4):3225, 1999.

[97] Harald Kübler, J. P. Shaffer, T. Baluktsian, R. Löw, and T. Pfau. Coherent excitation of Rydberg atoms in micrometre-sized atomic vapour cells. *Nature Photonics*, 4(2):112–116, 2010.

[98] Duan Yuping, Ma He, Li Xiaogang, Liu Shunhua, and Ji Zhijiang. The microwave electromagnetic characteristics of manganese dioxide with different crystallographic structures. *Physica B: Condensed Matter*, 405(7):1826 – 1831, 2010.

[99] *Technical Report AFML-TR-74-250. Dielectric constant and loss data*. Laboratory for Insulation Research, Massachuesetts Institute of Technology, 1977.

[100] Leonid Brekhovskikh. *Waves in Layered Media*. London: Academic Press, 1960.

[101] D Barredo, H Kübler, R Daschner, R Löw, and T Pfau. Electrical readout for coherent phenomena involving Rydberg atoms in thermal vapor cells. *Physical Review Letters*, 110(12):123002, 2013.

[102] Joshua A Gordon, Christopher L Holloway, Andrew Schwarzkopf, Dave A Anderson, Stephanie Miller, Nithiwadee Thaicharoen, and Georg Raithel. Millimeter wave detection via Autler-Townes splitting in rubidium Rydberg atoms). *Applied Physics Letters*, 105(2):024104, 2014.

[103] Hervé Gilles, Bernard Cheron, and Joseph Hamel. Dispersive effects in optically pumped (2 3 S 1) 4He atomic vapor measured by using a geometrical optics technique. *Optics Communications*, 190(1):179–184, 2001.

[104] Vladimir A Sautenkov, Hebin Li, Yuri V Rostovtsev, and Marlan O Scully. Ultradispersive adaptive prism based on a coherently prepared atomic medium. *Physical Review A*, 81(6):063824, 2010.

[105] Min Xiao, Yong-qing Li, Shao-zheng Jin, and Julio Gea-Banacloche. Measurement of dispersive properties of electromagnetically induced transparency in rubidium atoms. *Physical Review Letters*, 74(5):666, 1995.

[106] Marlan O Scully and Michael Fleischhauer. High-sensitivity magnetometer based on index-enhanced media. *Physical review letters*, 69(9):1360, 1992.

[107] GT Purves, G Jundt, CS Adams, and IG Hughes. Refractive index measurements by probe-beam deflection. *The European Physical Journal D-Atomic, Molecular, Optical and Plasma Physics*, 29(3):433–436, 2004.

[108] David J Starling, Steven M Bloch, Praveen K Vudyasetu, Joseph S Choi, Bethany Little, and John C Howell. Double lorentzian atomic prism. *Physical Review A*, 86(2):023826, 2012.

[109] Julio Gea-Banacloche, Yong-qing Li, Shao-zheng Jin, and Min Xiao. Electromagnetically induced transparency in ladder-type inhomogeneously broadened media: Theory and experiment. *Physical Review A*, 51(1):576, 1995.

[110] Tun Wang, SF Yelin, R Côté, EE Eyler, SM Farooqi, PL Gould, M Koštrun, D Tong, and D Vrinceanu. Superradiance in ultracold Rydberg gases. *Physical Review A*, 75(3):033802, 2007.

[111] C Carr, R Ritter, CG Wade, CS Adams, and KJ Weatherill. Nonequilibrium phase transition in a dilute Rydberg ensemble. *Physical Review Letters*, 111(11):113901, 2013.

[112] JE Thomas and WW Quivers Jr. Transit-time effects in optically pumped coupled three-level systems. *Physical Review A*, 22(5):2115, 1980.

[113] VM Borodin, II Fabrikant, and AK Kazansky. Collisional broadening of Rydberg states by alkali-metal perturbers. *Physical Review A*, 44(9):5725, 1991.

[114] VB Tiwari, S Singh, HS Rawat, Manoranjan P Singh, and SC Mehendale. Electromagnetically induced transparency in cold 85Rb atoms trapped in the ground hyperfine F= 2 state. *Journal of Physics B: Atomic, Molecular and Optical Physics*, 43(9):095503, 2010.

[115] Kiwoong Kim, Won-Kyu Lee, In-Seon Kim, and Han Seb Moon. Atomic vector gradiometer system using cesium vapor cells for magnetocardiography: Perspective on practical application. *Instrumentation and Measurement, IEEE Transactions on*, 56(2):458–462, 2007.

[116] David J Starling, P Ben Dixon, Andrew N Jordan, and John C Howell. Precision frequency measurements with interferometric weak values. *Physical Review A*, 82(6):063822, 2010.

[117] Luis G Marcassa and James P Shaffer. Interactions in ultracold Rydberg gases. *Advances in Atomic, Molecular, and Optical Physics*, 63:47–133, 2014.

[118] T Baluktsian, B Huber, R Löw, and T Pfau. Evidence for strong van der waals type Rydberg-Rydberg interaction in a thermal vapor. *Physical review letters*, 110(12):123001, 2013.

[119] A Urvoy, F Ripka, I Lesanovsky, D Booth, JP Shaffer, T Pfau, and R Löw. Strongly correlated growth of Rydberg aggregates in a vapor cell. *Physical Review Letters*, 114(20):203002, 2015.

[120] Utsab Khadka, Jiteng Sheng, and Min Xiao. Spatial domain interactions between ultraweak optical beams. *Physical Review Letters*, 111(22):223601, 2013.

[121] Chengjie Zhu, L Deng, EW Hagley, and Mo-Lin Ge. Optical cloaking using alternate Raman gain and free-space media in the presence of spatially distributed pump fields. *Physical Review A*, 88(4):045804, 2013.

[122] Andrew MC Dawes, Lucas Illing, Susan M Clark, and Daniel J Gauthier. All-optical switching in rubidium vapor. *Science*, 308(5722):672–674, 2005.

[123] Qingqing Sun, Yuri V Rostovtsev, and M Suhail Zubairy. Optical beam steering based on electromagnetically induced transparency. *Physical Review A*, 74(3):033819, 2006.

[124] William D Oliver, Yang Yu, Janice C Lee, Karl K Berggren, Leonid S Levitov, and Terry P Orlando. Mach-zehnder interferometry in a strongly driven superconducting qubit. *Science*, 310(5754):1653–1657, 2005.

[125] JG Rarity, PR Tapster, E Jakeman, T Larchuk, RA Campos, MC Teich, and BEA Saleh. Two-photon interference in a mach-zehnder interferometer. *Physical Review Letters*, 65(11):1348, 1990.

[126] Syed Abdullah Aljunid, Meng Khoon Tey, Brenda Chng, Timothy Liew, Gleb Maslennikov, Valerio Scarani, and Christian Kurtsiefer. Phase shift of a weak coherent beam induced by a single atom. *Physical review letters*, 103(15):153601, 2009.

[127] Michael A Armen, John K Au, John K Stockton, Andrew C Doherty, and Hideo Mabuchi. Adaptive homodyne measurement of optical phase. *Physical Review Letters*, 89(13):133602, 2002.

[128] J Denschlag, JE Simsarian, DL Feder, Charles W Clark, LA Collins, J Cubizolles, L Deng, EW Hagley, K Helmerson, WP Reinhardt, et al. Generating solitons by phase engineering of a bose-einstein condensate. *Science*, 287(5450):97–101, 2000.

[129] L Pezzé, LA Collins, A Smerzi, GP Berman, and AR Bishop. Sub-shot-noise phase sensitivity with a bose-einstein condensate mach-zehnder interferometer. *Physical Review A*, 72(4):043612, 2005.

[130] Graham T Purves, Charles S Adams, and Ifan G Hughes. Sagnac interferometry in a slow-light medium. *Physical review A*, 74(2):023805, 2006.

[131] David J Starling, P Ben Dixon, Nathan S Williams, Andrew N Jordan, and John C Howell. Continuous phase amplification with a sagnac interferometer. *Physical Review A*, 82(1):011802, 2010.

[132] AS Zibrov, MD Lukin, L Hollberg, DE Nikonov, MO Scully, HG Robinson, and VL Velichansky. Experimental demonstration of enhanced index of refraction via quantum coherence in Rb. *Physical review letters*, 76(21):3935, 1996.

[133] Yang Ji, Yunchul Chung, D Sprinzak, M Heiblum, D Mahalu, and Hadas Shtrikman. An electronic mach–zehnder interferometer. *Nature*, 422(6930):415–418, 2003.

[134] Daniel A Steck. *Cesium D line data revision 2.1.4.* 2010.

[135] David F Phillips, Irina Novikova, Christine Y-T Wang, Ronald L Walsworth, and Michael Crescimanno. Modulation-induced frequency shifts in a coherent-population-trapping-based atomic clock. *JOSA B*, 22(2):305–310, 2005.

[136] Marco G Genoni, Stefano Olivares, Davide Brivio, Simone Cialdi, Daniele Cipriani, Alberto Santamato, Stefano Vezzoli, and Matteo GA Paris. Optical interferometry in the presence of large phase diffusion. *Physical Review A*, 85(4):043817, 2012.

[137] NC Wong and John L Hall. Servo control of amplitude modulation in frequency-modulation spectroscopy: demonstration of shot-noise-limited detection. *JOSA B*, 2(9):1527–1533, 1985.

[138] Ralf Ritter, Nico Gruhler, Wolfram Pernice, Harald Kübler, Tilman Pfau, and Robert Löw. Atomic vapor spectroscopy in integrated photonic structures. *arXiv preprint arXiv:1505.00611*, 2015.

[139] Masayoshi Tonouchi. Cutting-edge terahertz technology. *Nature photonics*, 1(2):97–105, 2007.

[140] C Holloway, J Gordon, Steven Jefferts, Andrew Schwarzkopf, D Anderson, S Miller, Nithiwadee Thaicharoen, and Georg Raithel. Broadband Rydberg atom-based electric-field probe for SI-traceable, self-calibrated measurements. *IEEE Transactions on Antennas and Propagation*, 62(12):6169, 2014.

Appendix A

Publications and Presentations

A.1 List of publications

Below is a list of peer-reviewed publications in which I was either author or co-author.

1. **H. Fan**, S. Kumar, Jiteng Sheng, and J. Shaffer, "Microwave electrometry using Mach-Zehnder interferometer with Rydberg atoms in vapor cells " *in preparation*, (2016).

2. **H. Fan**, S. Kumar, H. Kübler, and J. Shaffer, "Dispersive radio frequency electrometry using Rydberg atoms in a prism-shaped atomic vapor cell " *J. Phys. B*, 49, 104004 (2016).

3. S. Kumar, J. Sheng, J. Sedlacek, **H. Fan**, and J. Shaffer, "Collective state synthesis in an optical cavity using Rydberg atom dipole blockade" *J. Phys. B*, 49, 064014 (2016).

4. **H. Fan**, S. Kumar, J. Sheng, J. Shaffer, C. Holloway, and J. Gorden, "Effect of Vapor-Cell Geometry on Rydberg-Atom-Based Measurements of Radio-Frequency Electric Fields" *Phys. Rev. Applied* 4, 044015 (2015).

5. **H. Fan** and S. Kumar, J. Sedlacek, H. Kübler, Harald, S. Karimkashi, Shaya and J. P. Shaffer, "Atom based RF electric field sensing", *J. Phys. B*, 48, 202001 (2015).

(*Invited Review*)

6. **H. Fan**, S. Kumar, R. Daschner, H. Kübler, and J. Shaffer, "Subwavelength microwave electric-field imaging using Rydberg atoms inside atomic vapor cells," *Opt. Lett.* 39, 3030-3033 (2014).

A.2 List of presentations

Below is a list of the presentations that I have either presented or been co-author of the presentation.

1. **Haoquan Fan**, Santosh Kumar, and James Shaffer, "Homodyne Microwave Electric Field Measurements Using Cesium Rydberg Atoms in Vapor Cells" DAMOP, 2015 *talk*.

2. **Haoquan Fan**, Santosh Kumar, Renate Dashner, and James Shaffer, "Sub-Wavelength Microwave Electric Field Imaging using Rydberg Atoms" DAMOP, 2014 *talk*.

3. Santosh Kumar, Jiteng Sheng, Jonathon Sedlacek, Charlie Ewel, **Haoquan Fan**, and James Shaffer, "Interacting Rydberg atoms in an optical cavity to synthesize coherent collective states using dipole blockade" DAMOP, 2015 *contributed talk*.

4. **Haoquan Fan**, Santosh Kumar, Renate Dashner, Jon Sedlacek, and James Shaffer, "Quantum-Assisted Electrometry using Electromagnetically Induced Transparency with Rydberg Atoms in a Vapor Cell" DAMOP, 2014 *poster*.

5. Harald Kübler, Jonathan A Sedlacek, Arne Schwettmann, Renate Daschner, **Haoquan Fan**, Santosh Kumar, Robert Löw, Tilman Pfau, and James P Shaffer, "Atom Based Vector Microwave Electrometry Using Rubidium Rydberg Atoms in a Vapor Cell" Quantum Information and Measurement, 2014 *poster*.

6. Jonathon Sedlacek, **Haoquan Fan**, Renate Daschner, Charles Ewel, and James Shaffer, "Using Rydberg Atom Electromagnetically Induced Transparency for Microwave Electrometry Applications" DAMOP, 2013 *poster*.

7. **Haoquan Fan**, Jon Sedlacek, Arne Schwettmann, James P Shaffer, Harald Kübler, and Tilman Pfau, "Quantum Assisted Sensing Using Rydberg Atom Electromagnetically Induced Transparency" DAMOP, 2012 *poster*.

8. Jonathon Sedlacek, Arne Schwettmann, **Haoquan Fan**, and James Shaffer, "Polarization Dependent Dark Resonances in Electromagnetically Induced Transparency with Rydberg Atoms" DAMOP, 2012 *poster*.